

VIBRATION BASED AND MINIATURIZABLE SATELLITE ATTITUDE
ACTUATOR

A THESIS SUBMITTED TO
THE GRADUATE SCHOOL OF NATURAL AND APPLIED SCIENCES
OF
MIDDLE EAST TECHNICAL UNIVERSITY

BY

BURAK AKBULUT

IN PARTIAL FULFILLMENT OF THE REQUIREMENTS
FOR
THE DEGREE OF DOCTOR OF PHILOSOPHY
IN
AEROSPACE ENGINEERING

SEPTEMBER 2019

Approval of the thesis:

**VIBRATION BASED AND MINIATURIZABLE SATELLITE ATTITUDE
ACTUATOR**

submitted by **BURAK AKBULUT** in partial fulfillment of the requirements for the degree of **Doctor of Philosophy in Aerospace Engineering Department, Middle East Technical University** by,

Prof. Dr. Halil Kalıpçilar
Dean, Graduate School of **Natural and Applied Sciences** _____

Prof. Dr. İsmail Hakkı Tuncer
Head of Department, **Aerospace Engineering** _____

Prof. Dr. Ozan Tekinalp
Supervisor, **Aerospace Engineering, METU** _____

Assist. Prof. Dr. Kivanç Azgın
Co-Supervisor, **Mechanical Engineering, METU** _____

Examining Committee Members:

Assist. Prof. Dr. Ali Türker Kutay
Aerospace Engineering, METU _____

Prof. Dr. Ozan Tekinalp
Aerospace Engineering, METU _____

Prof. Dr. Metin Uymaz Salamçı
Mechanical Engineering, Gazi University _____

Prof. Dr. Atilla Doğan
Mechanical and Aerospace Engineering, UT Arlington _____

Prof. Dr. M. Kemal Özgören
Mechanical Engineering, METU _____

Date: 05.09.2019

I hereby declare that all information in this document has been obtained and presented in accordance with academic rules and ethical conduct. I also declare that, as required by these rules and conduct, I have fully cited and referenced all material and results that are not original to this work.

Name, Surname: Burak Akbulut

Signature:

ABSTRACT

VIBRATION BASED AND MINIATURIZABLE SATELLITE ATTITUDE ACTUATOR

Akbulut, Burak
Doctor of Philosophy, Aerospace Engineering
Supervisor: Prof. Dr. Ozan Tekinalp
Co-Supervisor: Assist. Prof. Dr. Kivanç Azgın

September 2019, 157 pages

Major malfunctions are originated from bearing mechanisms of reaction wheels, momentum wheels and control moment gyroscopes. Current research investigates the theoretical background for attitude actuators depending on oscillatory actuation which can be implemented without bearings. The approximate angular momentum and dynamics of such a device is formulated. A prototype vibration based attitude control actuator was designed and produced. Design implications originating from the mathematical model of the actuator were incorporated into its mechanical design. An experimental setup consisting of a load cell and a frictionless air bearing was utilized. Experiments were carried in which the device successfully rotated the experimental setup; proving the concept of vibration based attitude actuation. Furthermore, a scale-down study was carried out to assess the novel concept's suitability for miniaturization. Later, a MEMS based actuator was designed and its functioning was exhibited through simulations.

Keywords: Attitude Control, Actuator, Vibration, MEMS, Miniaturization

ÖZ

TİTREŞİM TEMELLİ VE KÜÇÜLTÜLEBİLİR UYDU YÖNELİM EYLEYİCİSİ

Akbulut, Burak
Doktora, Havacılık ve Uzay Mühendisliği
Tez Danışmanı: Prof. Dr. Ozan Tekinalp
Ortak Tez Danışmanı: Dr. Öğr. Üyesi Kıvanç Azgın

Eylül 2019, 157 sayfa

Tepki tekerleri, momentum tekerleri ve kontrol momenti jiroskopları gibi uydu yönelim eyleyicilerinde yer alan yataklama mekanizmaları büyük arızalara sebebiyet verebilmektedir. Bu çalışmanın amacı yatak mekanizmasına ihtiyaç duymadan gerçekleştirilebilecek yönelim eyleyicilerini kavramsal olarak ortaya koymaktır. Bu cihazın açısal momentum ve dinamik etkileri formüle edilmiştir. Prototip bir titreşim temelli yönelim eyleyicisi tasarlanmış ve üretilmiştir. Matematiksel modelden yapılan çıkarımlar eyleyicinin mekanik tasarımına dâhil edilmiştir. Yük hücresi ve sürtünmesiz hava yatağı kullanılarak deneyler yapılmıştır. Cihaz, hava yatağı üzerinden yer alan deney düzeneğini döndürmeyi başarmasıyla titreşim temelli yönelim eyleyicisi kavramı deneyel olarak doğrulanmıştır. Bu yeni kavramın minyatürleştirilebilmesini değerlendirmek için bir ölçeklendirme analizi yapılmıştır. Buna istinaden, MEMS tabanlı bir eyleyici tasarlanmış ve işleyişi benzetimlerle gösterilmiştir.

Anahtar Kelimeler: Yönelim Denetimi, Eyleyici, Titreşim, MEMS, Minyatürleştirme

To my late Father,

ACKNOWLEDGEMENTS

Firstly, I would like to thank my supervisor Prof. Dr. Ozan Tekinalp for his guidance and my co-supervisor Asst. Prof. Dr. Kivanç Azgin for his valuable insights on MEMS scale actuator design.

This work is possible through the help of many friends; foremost being Mr. Ferhat Arberkli. This project would not have been realized if not for his mechanical aptitude and intuition as well as his camaraderie. I also extend my gratitudes to Mr. Eyyüp Demirkutlu for his help during the instrumentation of the actuator.

I would also like to thank the Scientific and Technological Research Council of Turkey (TÜBİTAK) for supporting this study in the framework of project 214M074. Additionally, I thank the METU Center of Excellence in Biomaterials and Tissue Engineering for lending their MSC ADAMS license.

Last, but definitely not the least; I would like to thank my wife Cansu Alsancak-Akulut for her ever present support, endurance and understanding

TABLE OF CONTENTS

ABSTRACT	v
ÖZ	vi
ACKNOWLEDGEMENTS	viii
TABLE OF CONTENTS	ix
LIST OF TABLES	xiii
LIST OF FIGURES	xiv
LIST OF ABBREVIATIONS	xix
LIST OF SYMBOLS	xx
1. INTRODUCTION	1
1.1. Overview of Satellite Attitude Actuation	1
1.2. Failure Trends in Actuators	5
1.3. Vibration Based Actuation	6
1.4. Motivation	9
1.5. Contribution.....	10
1.6. Organization	11
2. MATHEMATICAL MODEL	13
2.1. Introduction	13
2.2. Review of Dynamic Models.....	13
2.3. Free Body Diagram	14
2.4. Sense of Motion.....	15
2.5. Vector Equations	16
2.5.1. Angular Momentum.....	16

2.5.2. Equation of Motion	17
2.6. Matrix Formulation.....	20
2.6.1. Angular Momentum	22
2.6.2. Torque Expressions	24
2.7. Shaping the Actuator.....	26
3. ACTUATOR DESIGN.....	35
3.1. Vibration Based Actuator (VBA) Architecture	35
3.2. Mechanical Design.....	37
3.2.1. Rotor and Gimbal Design.....	37
3.2.2. Springs.....	40
3.2.3. Support Structures & Cabling	43
3.2.4. Structural Analysis	45
3.3. Electrical Architecture	46
3.3.1. Power Interface.....	46
3.3.2. Stepper Motors	46
3.3.3. Driving Circuit	47
3.3.4. Instrumentation.....	49
3.4. Algorithm and Software.....	55
4. SIMULATION AND RESULTS	57
4.1. Justification	57
4.2. Simulation Model.....	58
4.3. Results	60
5. EXPERIMENTAL SETUPS	67
5.1. Load Cell.....	67

5.2. Frictionless Air Bearing	68
5.2.1. Tethered Configuration.....	68
5.2.2. Un-Tethered Configuration.....	70
6. EXPERIMENTAL RESULTS	75
6.1. Load Cell	75
6.2. Frictionless Air Bearing	79
6.2.1. Tethered Configuration.....	80
6.2.2. Un-Tethered Configuration.....	81
6.2.2.1. Telemetry from run #2	83
6.2.2.2. Telemetry from run #4	90
6.3. Summary of Results	94
7. A MEMS VIBRATION BASED ACTUATOR.....	97
7.1. A Case for Miniaturization.....	97
7.1.1. Satellite Miniaturization Trend	98
7.1.2. Actuator Performance and Dimensional Analysis.....	98
7.1.3. Results.....	103
7.2. MEMS Based VBA Architecture	107
7.3. Actuator Design.....	108
7.3.1. Justification for TMA Utilization	108
7.3.2. TMA Placement.....	109
7.3.3. Determining TMA Force and Stroke	113
7.3.4. Thermo-Mechanical Actuator (TMA) Design	114
7.3.5. Spring and Shaft Sizing	117
7.4. Results	120

8. CONCLUSION	127
8.1. Summary	127
8.2. Discussion	128
8.3. Conclusion	129
8.4. Future Work	130
REFERENCES	135
A. Datasheet for the Components Utilized in Actuators	141
B. Datasheet for the Equipment Utilized in Experimental Setup	147
CURRICULUM VITAE.....	155

LIST OF TABLES

TABLES

Table 2.1. Coordinate Frame Associations of Dyadics and Vectors	21
Table 3.1. Calibration Parameters for the Accelerometers	50
Table 3.2. Calibration Parameters for the Gyroscopes	52
Table 7.1. RSI 15-215 Reaction Wheel Estimated Data [39]	103
Table 7.2. Rod-type VBA [30].....	103
Table 7.3. TMA Characteristics	117
Table 7.4. MEMS VBA Properties	125

LIST OF FIGURES

FIGURES

Figure 1.1. Basic Control System as Defined by ESA	2
Figure 1.2. A Collage of Common Spacecraft Actuators.....	4
Figure 1.3.Feline Body as Interlinked Rigid Bodies	6
Figure 1.4. Dynamical Model Including Astronaut Torso, Upper and Lower Limbs to Assess the Effects of Cyclic Limb Motion on Astronaut Attitude	7
Figure 2.1. Rotor, Gimbal and Spacecraft Body Configuration and Respective Coordinate Systems	14
Figure 2.2. The Complete Motion Cycle for the Vibration Based Satellite Attitude Actuator	15
Figure 2.3. Rod Shaped VBA Implementation.....	27
Figure 2.4. Proposed Design for a VBA with A Rotor Having Uniformly Distributed Inertia.....	30
Figure 2.5. Locus of Angular Momentum Vector for $\sigma = -90^\circ$	31
Figure 2.6. Locus of Angular Momentum Vector for $\sigma = 0^\circ$	32
Figure 2.7. Evolution of Angular Momentum Loci from $\sigma = -90^\circ$ to $\sigma = 0^\circ$	33
Figure 2.8. Locus of Angular Momentum Vector for $\sigma = 0^\circ$ to $\sigma = 90^\circ$	34
Figure 3.1. Actuator Architecture Together with Interfaces.....	35
Figure 3.2. The Prototype Actuator	37
Figure 3.3. CAD Design of the Rotor.....	38
Figure 3.4. Manufactured Hemispheres.....	39
Figure 3.5. The Gimbal and Its Mechanical Interfaces	40
Figure 3.6. Spring Elements at Gimbal and Rotor.....	42
Figure 3.7. Inner View of the Actuator.....	44
Figure 3.8. Fundamental Modes of the Gimbal Shaft and the Balance Mass	45
Figure 3.9. Fundamental Modes of the Shaft Side Rotor Hemisphere	46

Figure 3.10. Electrical Diagram of the Driver Circuit	48
Figure 3.11. Circuit Implementation.....	48
Figure 3.12. Gimbal IMU in Different Stable Poses for Calibration	50
Figure 3.13. Gimbal and Rotor Hall Effect Sensor Implementation.....	53
Figure 3.14. Curve Fit for the Gimbal Angle.....	54
Figure 3.15. Curve Fit for the Rotor Angle.....	55
Figure 4.1. The Model Utilized in ADAMS Simulation.....	59
Figure 4.2. MSC ADAMS Simulation Result Predicting the Angular Motion of the Air Bearing Due to Operation of the Actuator.....	61
Figure 4.3. Spectrum of Air Bearing Angular Velocity.....	62
Figure 4.4. Simulated Rotor and Gimbal Angles.....	62
Figure 4.5. Frequency Content of the Rotor and Gimbal Angular Motion.....	63
Figure 4.6. Rotor and Gimbal Angular Rates	64
Figure 4.7. Comparison of Result Together with the Actuator Output.....	64
Figure 5.1. Load Cell Experimental Setup.....	68
Figure 5.2. Air Bearing Experimental Setup in Tethered Configuration	69
Figure 5.3. Levels Present on the Mounting Table for Level Adjustment.....	69
Figure 5.4. Architecture for Untethered Experimental Setup	70
Figure 5.5. Command Shifting and Amplification Circuit	71
Figure 5.6. Oscilloscope View of the PCF8591 DAC Signal (Channel #2) Shifted and Amplified (Channel #1) to be Fed into Driving Circuit.....	72
Figure 5.7. Hall Effect Sensor Amplifying Circuit	72
Figure 5.8. Setup for Wireless Experimentation.....	73
Figure 6.1. Torque Measurements for the Gimbal and Rotor Axis with Sinusoidal Excitations Having 0.6V and 1.2V Amplitudes.....	76
Figure 6.2. Torque Measurements for the Output Axis	76
Figure 6.3. Frequency Content of the Torque Measurements.....	77
Figure 6.4. Relation Between Input Rotor and Gimbal Voltage Phase Difference with Measured Rotor and Gimbal Torque Phase Difference	78
Figure 6.5. Output Torque Frequency Content for Varying Phase Values.....	79

Figure 6.6. Air-Bearing Encoder Angle History	80
Figure 6.7. Air-Bearing Encoder Angle Spectral Content.....	81
Figure 6.8. Air Bearing Position for Various Input Phase Difference Settings.....	82
Figure 6.9. Encoder Angle and Angular Rate for Test Run #2	84
Figure 6.10. Frequency Content of Run #2 Derived from Air Bearing Angle Data .	85
Figure 6.11. Rotor and Gimbal Angles with Specific Detail at the 75 th Second.....	85
Figure 6.12. Frequency Content of the Rotor and Gimbal Angular Motion	86
Figure 6.13. Rotor and Gimbal Angular Rates	87
Figure 6.14. Weighing Campaign for the Setup Tray Elements to Identify Mass Properties	88
Figure 6.15. CAD Model to Which the Mass Measurements were Input and Moment of Inertia Estimate was Obtained.....	88
Figure 6.16. Comparison of Run #2 Encoder Derived Results with the Actuator Output.....	89
Figure 6.17. Encoder Angle and Angular Rate for Test Run #4	91
Figure 6.18. Frequency Content of Run #4	91
Figure 6.19. Rotor and Gimbal Angles.....	92
Figure 6.20. Frequency Content of the Rotor and Gimbal Angular Motion	92
Figure 6.21. Rotor and Gimbal Angular Rates	93
Figure 6.22. Comparison of Run #4 Encoder Derived Results with the Actuator Output	94
Figure 7.1. Correlating Maximum Reaction Wheel Angular Speed with Respect to Their Size.....	100
Figure 7.2. Scaling Analysis Comparison of VBA and RW Angular Momentum..	104
Figure 7.3. Scaling Analysis Comparison of VBA and RW Volumetric Angular Momentum.....	105
Figure 7.4. Scaling Analysis Comparison of VBA and RW Specific Angular Momentum.....	106
Figure 7.5. Enumerated Actuators.....	107

Figure 7.6. Spring and Shaft Structures Together with Their Connection to the TMA	108
Figure 7.7. Forces Being Applied by TMAs on the Rotor.....	110
Figure 7.8. Pulling Forces Applied by Individual TMAs	112
Figure 7.9. Torque Resulting from Compound Application of Force by the TMA array	112
Figure 7.10. A Simplified Depiction of a TMA	114
Figure 7.11. A Single Buckle-Beam Element.....	115
Figure 7.12. TMA Design Detail from MEMS VBA	117
Figure 7.13. Spring Element and Shaft Implemented by Cantilevered Beams.....	119
Figure 7.14. First Modal Shape for the MEMS Actuator (@447.37 Hz)	121
Figure 7.15. Second Modal Shape for the MEMS Actuator (@688.71 Hz)	122
Figure 7.16. Third Modal Shape for the MEMS Actuator (@792.51 Hz).....	122
Figure 7.17. Temperature Distribution of Thermal Actuators to Enable x- Axis Rotation.....	123
Figure 7.18. Resulting Deformation Leading to x- Axis Rotation.....	124
Figure 7.19. Temperature Distribution of Thermal Actuators to Enable y- Axis Rotation.....	124
Figure 7.20. Resulting Deformation Leading to y- Axis Rotation.....	125
Figure 7.21. A Representative Chip-Sized Satellite [80]	126
Figure 8.1. Driving Two Spherical Rotor VBAs with $\pi/2$ Total Phase Difference to Cancel out Parasitic Angular Momentum in Non-output Axes.....	132
Figure 8.2. Driving Two Spherical Rotor VBAs with π Total Phase Difference to Smooth Output Angular Momentum	132
Figure 8.3. A Hypothetical Four Element VBA Array with Constant and Single Axis Angular Momentum Output.....	133
Figure A.1. Power Operational Amplifier LA6500 Specifications.....	141
Figure A.2. Power Operational Amplifier LA6500 Specifications Continued	142
Figure A.3. MPU6050 IMU Specifications for Gyroscope Functionality	143
Figure A.4. MPU6050 IMU Specifications for Accelerometer Functionality.....	144

Figure A.5. UGN3503 Hall Effect Sensor Specifications	145
Figure A.6. UGN3503 Hall Effect Sensor Specifications Continued	145
Figure B.7. NI PCI-4461 High Performance ADC/DAC Card Specifications.....	147
Figure B.8. NI PCI-4461 High Performance ADC/DAC Card Specifications Continued.....	148
Figure B.9. MC3A-250 Load Cell Specifications	149
Figure B.10. PI Glide Model A-603.050H Air Bearing Specifications.....	150
Figure B.11. PI Glide Model A-603.050H Air Bearing Specifications Ctd.....	151
Figure B.12. Atlas Copco Air Compressor for Air Bearing Supply.....	152
Figure B.13. PCF8591 ADC/DAC Specifications	153
Figure B.14. TL082 Operational Amplifier Specification.....	154

LIST OF ABBREVIATIONS

ABBREVIATIONS

ADC	Analog to Digital Converter
ADCS	Attitude Determination and Control System
CAD	Computer Aided Design
CMG	Control Moment Gyroscope
COG	Center of Gravity
COTS	Commercial off the Shelf
DAC	Digital to Analog
DC	Direct Current, <i>i.e.</i> 0 Hz content of a signal
DCM	Direction Cosine Matrix
EAP	Electroactive Polymer
ESA	European Space Agency
I2C	Inter-Integrated Circuit (serial communication protocol)
IMU	Inertial Measurement Unit
MEMS	Micro Electro-Mechanical Systems
NA	Not Applicable
RW	Reaction Wheel
TMA	Thermo-Mechanical Actuator
VBA	Vibration Based Actuator

LIST OF SYMBOLS

SYMBOLS

m	: mass, kg
J	: inertia, kg.m ²
f	: excitation frequency, Hz
r	: position, m
v	: velocity, m/s
a	: acceleration, m/s ²
ω	: angular velocity, rad/s
α	: angular acceleration, rad/s ²
H	: angular momentum, N.m.s
τ	: torque, N.m
θ	: rotor angle, rad
φ	: gimbal angle, rad
σ	: phase difference, rad
C	: transformation matrix, unitless
V	: potential difference, volts
ε	: accelerometer offset angle, direction cosine
γ	: gyroscope offset angle, direction cosine
s	: measurement scale factor, unitless
b	: bias, rad/s or g
ν	: measurement noise, rad/s or g
ρ	: density, kg/m ³
r_1, r_2	: RW inner and outer dimensions, m
h	: RW height, m
η	: scaling factor, unitless
k	: spring coefficient, N.m/rad
E	: modulus of elasticity, Pa
I	: section moment of inertia, m ⁴
L	: beam length, m
W	: beam width, m
t	: beam thickness, m
F	: TMA pulling force, N
T	: torque applied on MEMS VBA rotor, N.m
u	: TMA displacement, m

Superscripts & Subscripts

i	: inertial frame
s	: spacecraft body
g	: gimbal
r	: rotor
j/k	: vector quantity of/on “j” with respect to/by “k”
x	: x-axis component
y	: y-axis component
z	: z-axis component
a	: accelerometer
gyr	: gyroscope
rod	: relating to rod-type rotor VBA
sph	: relating to sphere-type rotor VBA
spr	: relating to the spring element
sh	: relating to the shaft element
m	: measured value
r	: real value

Accents

\tilde{x}	: dyadic
\vec{x}	: vector
\hat{x}	: two dimensional matrix
\bar{x}	: column matrix
\dot{x}, \ddot{x}	: first and second time derivative

CHAPTER 1

INTRODUCTION

1.1. Overview of Satellite Attitude Actuation

Spacecraft attitude dynamics and control is concerned with the orientation of the spacecraft. Orientation is critical since a multitude of subsystems on the spacecraft are required to be pointed to certain targets to function. For instance, solar panels have to be directed to the Sun for generating power and antennae have to be pointed to ground stations on Earth for receiving or transmitting signals. But the most performance critical case is the pointing of the satellite payload (*i.e.* electro-optical camera, synthetic aperture radar etc.) to various targets on Earth (or to another heavenly body) for data collection. For such Earth observation or astronomy missions, spacecraft attitude dynamics becomes mission critical since the attitude control system is expected to reorient the spacecraft in a prescribed duration (*i.e.* time limited maneuver) and hold the orientation during data collection within a predefined error limit.

Similar to the other control systems, spacecraft attitude control systems do also consist of sensors, actuators, controlled plant and controllers [31]. In such a system, sensors provide information regarding the attitude (or the rate of change of attitude) of the spacecraft (*i.e.* star tracker and gyroscope) or they may also provide direction of other celestial bodies (*i.e.* sun sensor, earth horizon sensor) or magnetic field (*i.e.* magnetometer) from which the spacecraft attitude can be calculated. Attitude determination algorithms (*i.e.* Kalman Filter, QUEST etc.) are utilized to accurately determine the spacecraft orientation. In turn, guidance algorithms are utilized to determine the target attitude and hence the current error state that could be fed to the controllers. Controllers provide the control laws that provide the necessary commands

to the actuators by processing the measurements from the sensors. Actuators provide angular momentum exchange (*i.e.* reaction wheel) with or apply moment (*i.e.* magnetic torque rod) to the spacecraft so it can reorient to the desired target while rejecting disturbance moments from various sources.

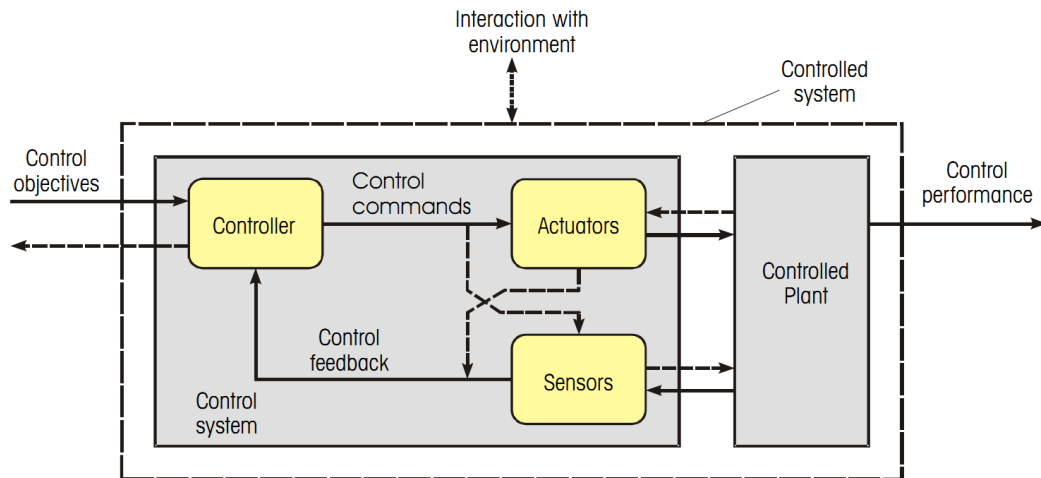


Figure 1.1. Basic Control System as Defined by ESA

As mentioned earlier, being an integral part of the attitude control loop, major attitude actuators utilized for manipulating spacecraft can be named as; magnetic torque rods, propulsion system (also known as reaction control system), reaction/momenta wheels and control moment gyroscopes (CMGs).

Magnetic torque rods utilize the principles of electromagnetism to produce torque via interaction with the Earth's magnetic field. This torque is limited and dependent on the spacecraft attitude with respect to local magnetic field as well as the variance in the magnetic field depending on the spacecraft orbital position. However, they are useful at the beginning of a satellite missions when the angular momentum exchange actuators (*i.e.* CMGs and reaction wheels) are yet to be initialized and the excess satellite angular velocities after deployment from the launcher have to be attenuated. They are also utilized for angular momentum dumping to de-saturate the actuators as well as contingency equipment. Lastly, they only work when the spacecraft is in the

close vicinity of a planetary body having an intrinsic magnetic field. For instance, while visiting planets lacking a substantial magnetic field (*i.e.* Venus and Mars [32]), spacecraft have to utilize the propulsion system for angular momentum management, expending relatively precious propellant in the process.

Propulsion system is mainly used for orbit maneuvering. However, as mentioned earlier, they may also be used for attitude control by utilizing the thrusters to generate momentum couples. Since their operation involve expenditure of propellants, using of propulsion system for attitude control is considered to be costly.

Reaction/momentum wheels utilize the exchange of angular momentum with the spacecraft to reorient it. Reaction wheels produce the required control moment by accelerating/decelerating the rotor they house. In contrast, momentum wheels have rotors that spin at a constant rotational speed thus giving the spacecraft gyroscopic stiffness in a certain direction. Reaction wheels have greater torque output capacity and more precise control capability in contrast with the magnetic torque rods.

Last but not least, similar to the reaction wheels, CMGs also induce satellite angular motion via angular momentum exchange. However, the main distinction between reaction wheels and CMGs lies in the method of changing the angular momentum vector. Reaction wheels alter the angular momentum vector magnitude whereas CMGs shift the direction of the vector in order to apply moment to the host satellite.

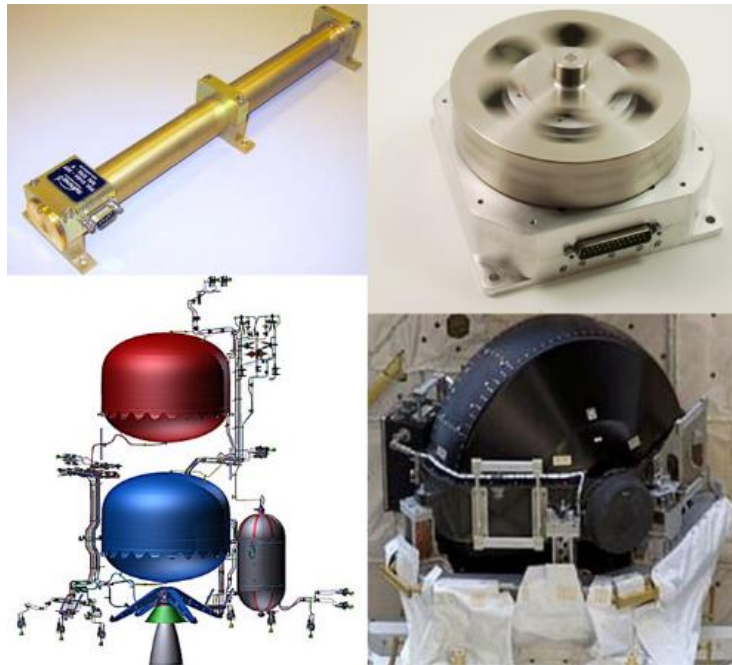


Figure 1.2. A Collage of Common Spacecraft Actuators. From Top Left, In Counterclockwise: Magnetic Torque Rod, Reaction Wheel, Control Moment Gyroscope and Propellant System

In addition to the previously mentioned traditional actuators, the search for more efficient and novel attitude actuators have also been long underway, resulting in numerous actuator propositions. For instance, Rossini *et al* proposed a reaction sphere [2], a momentum exchange device having a spherical rotor suspended within a magnetic field. Spherical rotor is composed of a permanent magnet with eight poles whereas the stator employs twenty coils for electrical manipulation. Its main proposition is that the rotor can be rotated in any direction; thus three axes attitude control can be ensured with a single actuator.

Another proposed actuator is the tilted wheel (or rotor), which can generate torques in three distinct axes utilizing a spinning rotor and two degree of freedom tilt mechanism [3][4]. The tilt mechanism reorients the rotor's angular momentum vector. This enables the device to act as double axis CMG albeit with limited rotation angles. Tilting provides control authority in two axes, whereas manipulation of the wheel speed provides the control authority in the third. It's claimed to be more simple to

implement than a conventional CMG and unlike CMGs singularities are not expected to be encountered in its operation [33].

An additional proposed novel actuator is the electroactive polymer actuators by Menon *et al* [18]. In this particular research, controlled large deflections of beams made of electroactive polymers (EAP) are proposed to manipulate satellite attitude. EAP materials are light and can perform large deflections with a relatively small amount of energy input.

Yet another novel actuation proposition is the utilization of fluid based momentum exchange devices [19],[20]. Named as fluidic momentum control (FMC), this particular actuator functions by circulating fluids in closed loops utilizing mechanical pumps. Its claimed advantages are the transmitting of minimal vibration to the structure due to the employment of fluids as rotors, its low energy density and flexibility for dual use such thermal cooling [25].

1.2. Failure Trends in Actuators

Of the traditional attitude actuators; reaction wheels and CMGs utilize continuous rotational motion to output the required torque and angular momentum for regulating satellite pointing. This continuous rotary motion requires the utilization of bearings and other mechanisms, which in turn are major sources of failures [5]. Reaction wheels are prone to bearing malfunctions; recent missions that have experienced such failures can be named as Hayabusa [9], Radarsat-1 [22], FUSE Observatory [7], Kepler Space Telescope and Dawn Space Probe [8]. Such failures even prompted satellite operators like Globalstar to implement reaction wheel monitoring procedures to preemptively identify possible future failures and take necessary precautions [8].

Being more complicated mechanically than the reaction wheels, CMGs also suffer from similar malfunctions. Skylab, housed three double gimbal CMGs [16]. During its operations, one of its CMGs experienced bearing failure and another exhibited anomalous behavior. CMGs were utilized on Mir space station as well; called "Gyrodynes", they were single gimbal control moment gyroscopes in contrast to the

double axis Skylab CMGs [23]. A total of twelve Gyrodynes were on Mir with clusters of six being in different modules. By the year 1991, five out of twelve had failed. ISS, having four double gimbal CMGs, also suffered malfunctions. Sensors (accelerometers) embedded in the CMGs measured excessive radial acceleration due to the imbalance caused by a faulty bearing.

1.3. Vibration Based Actuation

Number of researchers investigated the idea of attitude control via structural vibration. The motion of a cat in a free-fall is one of the foremost naturally occurring examples of attitude manipulation through periodic shape change. Kane proposed a model composed of two rigid bodies (Figure 1.3) that can bend with respect to each other (but do not twist to model cat's spine integrity) to better explain the dynamics of such motion [10].

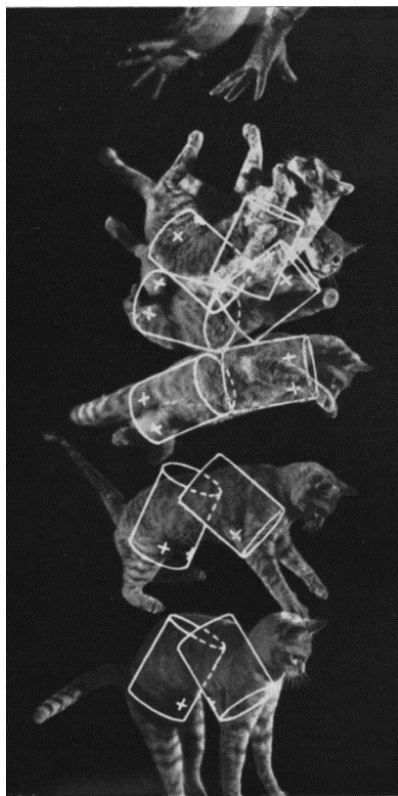


Figure 1.3.Feline Body as Interlinked Rigid Bodies for Cat Self-Righting Reflex Dynamical Modelling (from Ref. [10])

Later, a robotic “cat” composed of two rigid bodies connected by spine-like joints with artificial rubber muscles actuators was implemented by Kawamura to validate this dynamical model [14]. Kane later extended this research to astronaut motion by formulating the effect of limb actuation on astronaut attitude [11]. Utilizing multiple rigid body Lagrange formulation, a mathematical model was developed to relate per cycle of conical limb actuation to astronaut orientation change. It was shown that via conical motion of arms around shoulder joints an astronaut can change his/her pitch angle. Similarly, conical periodic leg motion can lead to the yawing motion. However, only stationary initial condition was considered and other cases such as de-spinning of an already spinning astronaut was not mentioned. Note that especially the case of pitch control through arm rotation is very similar to the previous research conducted in Ref. [30].

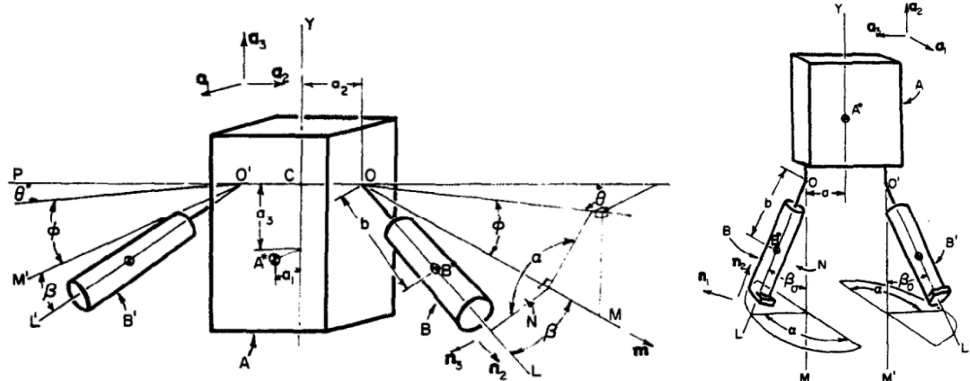


Figure 1.4. Dynamical Model Including Astronaut Torso, Upper and Lower Limbs to Assess the Effects of Cyclic Limb Motion on Astronaut Attitude (from Ref. [11])

Brockett classifies vibration based actuators as non-holonomic systems in which upon completion of a periodic cycle by an input element (i.e. actuator), the output element (i.e. spacecraft) is offset by a certain amount. Hence, they can be treated as mechanical analogues of electrical rectifiers; translating oscillatory motion to unidirectional motion [12]. This work emphasizes important points that were also observed in the current research; the importance of area defined by the trajectory function defined

through the phase difference between input signals, the ability to incite motion in a direction that is not being driven, the necessity of having at least two degrees of freedom (*i.e.* in our case gimbal and rotor) to generate rectification, the importance of the phase angle between the exciting periodic signals and the possibility of controlling the phase angle to control the speed and direction of the output.

Koh defined actuators named as pseudowheels, which unlike Brockett's proposition are only proof masses undergoing rotational motion to impart an opposite rotational motion on the host body [84]. Such actuators need to be large to be effective. In the presented experimentation, even though beams were very large; their actuation leads only to a small angular maneuver of a very minuscule bus with nearly 1 mm size. Since vibration based actuators may demand power to keep their morphed shape, a novel method was proposed involving successive actuation (and subsequent reverse actuation) of pseudowheels to effect a net change of orientation (which can be considered as some sort of an "attitude caterpillar"). Even though this research was able to present reorientation capability of this novel actuator, control capability for de-spinning a platform was not mentioned.

Bernstein utilized proof masses situated on linear tracks (in contrast with the rotary actuators in our current study) and a platform on a frictionless air bearing to investigate vibration based actuation [13]. They concluded that vibration based actuation to be a low authority attitude control method that could at best be supplementary to traditional momentum exchange devices. It was also found that open loop controller commanding positions with phase provided more effective response than closed-loop controllers. Due to the linear nature of their actuators, the center of mass of the system was ever changing, hindering the air bearing experiment.

In Ref. [21] a microelectromechanical system (MEMS) CMG consisting of rotary comb drive actuated rotor and parallel plate actuated gimbal was proposed. Unlike the traditional CMGs, rotor and gimbal of this device are actuated through vibrations. However, in this work, no detailed simulation results and MEMS design or fabrication

details were given. In Ref. [6], further research was built upon this concept by introducing a MEMS design together with a proposed manufacturing process and corresponding simulations via MEMS dedicated simulation package. However, possible interactions with the spacecraft attitude dynamics (*i.e.* as in the case of gyroscopic effects introduced by a reaction wheel during an attitude slew) were not explicitly stated in this work. Both in these works, the authors regard the proposed devices as CMGs instead of vibration based actuators. Additionally, their derivation is erroneous since they conclude that a net torque can be applied to the satellite with such a device.

Tyrell provides an extensive literature survey on attitude control of deformable bodies [85]. He identifies the problem as an extension of Gauge Theory in physics and further proposed alternative implementation methods. An experimental study was also carried out but the prototype failed to yield useful data.

1.4. Motivation

Recalling the history of CMG utilization in space stations from the previous section, one can observe that every CMG cluster sent to orbit for a space station has experienced at least a partial failure; known culprits being the bearings.

In this study, the possibility of utilizing oscillating mass actuators, to replace traditional momentum exchange devices is explored. In other words, means of replacing rotational continuous motion with an oscillatory motion will be examined. In addition to this, due to the ever increasing trend of small satellite utilization, a miniaturizable satellite actuator concept would likely to be well received by the industry. As it will elaborated upon Chapter 7, current moment exchange devices scale-down poorly. Thus, a new actuation scheme having better miniaturization performance would have better chance of adoption in the ever expanding pico-satellite domain.

1.5. Contribution

The main contributions of this study can be summarized as:

- Formulation of the vibration based actuation's effect on host satellite body's attitude through conservation of angular momentum.
- Design and manufacturing of a prototype novel satellite attitude actuator capable of attitude manipulation through structural vibration. The electrical and mechanical hardware of the prototype has been either COTS or in-house designed. The necessary software for utilization of the device was also designed, coded and implemented.
- The experimental campaign and the resulting validation of attitude manipulation through vibration based actuation.
- Scale-down study to investigate the effect of miniaturization on the both traditional momentum exchange as well as vibration based actuators' performance and the subsequent identification of VBA concept's advantage in the micro domain.
- Conceptualization and subsequent design of MEMS based VBA aimed for picosatellite utilization. Simulation results exhibiting the functioning of the device.

Some secondary contributions of this thesis can be mentioned as:

- A low-cost, wireless air bearing setup capable of momentum exchange experimentation in single axis.
- Implementation of simple calibration method for COTS IMUs that enable angular sensing within $\pm 0.1^\circ$ range.
- Realization of angular position sensing through Hall effect sensor. Methodology for calibration of such sensors with the previously mentioned IMUs to enable gimbal and rotor position sensing.

1.6. Organization

The organization of the dissertation is elaborated below:

Chapter 1 provides a general introduction regarding satellite attitude actuation. It discusses failure trends in the current actuators prevalent in the industry and builds-up motivation for the investigation of the vibration based actuation. It also explores the existing research activities regarding VBAs.

Chapter 2 develops the mathematical model relating the VBA functioning with the satellite attitude. The angular momentum output of the VBAs are formulized as a function of VBA design parameters and several VBA types are proposed.

Chapter 3 introduces the prototype actuator through detailed specification of its mechanical, electrical and software design.

Chapter 4 quantifies the expected output from the prototype through high fidelity MSC ADAMS simulation based on the actual CAD model from which the prototype was built.

Chapter 5 defines the experimental setups utilized throughout the experimental campaign aimed at proving the vibration based actuation concept via the utilization of the manufactured prototype.

Chapter 6 provides the results from various experiments conducted in the experimental campaign.

Chapter 7 examines the effect of miniaturization on the performance of attitude actuators. Miniaturization performances of both the traditional RW actuator and rod-type VBA are compared and dimensions where VBAs become more effective were tried to be identified. Later, a miniaturized rod-type MEMS VBA design that could be suitable for utilization in microsatellites is proposed and explored.

Chapter 8 discusses the results obtained so far and highlights possible avenues of future research.

CHAPTER 2

MATHEMATICAL MODEL

2.1. Introduction

The aim of this chapter is to establish the mathematical relationship between VBA design parameters and the resulting change in the satellite attitude due to VBA operation.

For the mathematical derivations throughout this chapter, it is assumed that all the bodies involved are rigid and not deformable. Furthermore, no mass is expulsed and the main spacecraft body is free to rotate in space.

It was further assumed that the centers of mass and the connection points of all the rigid bodies are coincident. In other words, there exists no static imbalance; hence the VBA simplifies to purely rotational dynamics. Moreover, all the angular oscillations of VBA are assumed to be small. Lastly, the body frames and the principal inertia axes of each rigid body is coincident. In other words, the inertia matrix of a rigid body does not possess off-diagonal elements.

2.2. Review of Dynamic Models

Several approaches exist for deriving the equations of motion for a satellite-CMG system. Viswanathan *et al* carried out a detailed survey of derivation approaches, identifying that the axissymmetric rotor assumption is widespread and models lack complete formulation [27]. Their approach utilized Lagrangian dynamics. Similarly, Roithmayer *et al* utilizes Kane's method [28]. For mixed CMG and momentum wheel control strategies, Skelton used Newton-Euler formulation to derive equation of motion for the hybrid actuated spacecraft [29]. Similarly, Stevenson and Schaub also utilizes Newton-Euler approach to derive the governing dynamics for double gimbal

variable speed CMG [15]. Their argument is that the Newton-Euler formulation provides ease when identifying the physical significance of various resulting terms. In this study, a similar approach is adopted. The Newton-Euler formulation is utilized together with transport theorem in order to easily discern the effects of gimbal and rotor actuation on the spacecraft.

2.3. Free Body Diagram

The proposed actuator is presented in Figure 2.1. Note that the gimbal is shown tilted in the spacecraft x- axis and the gimbal rotation takes place around it with angle φ . Similarly, the rotor is also shown tilted with angle θ in the gimbal y- axis. The output is expected to be along the z- axis of the spacecraft, which itself is represented by a slab like structure. Both the gimbal and rotor have single degree-of-freedom in the form of rotation motion defined by φ and θ , whereas the host spacecraft's body is assumed to be free to rotate in all three axes. Translational motions are assumed to be zero.

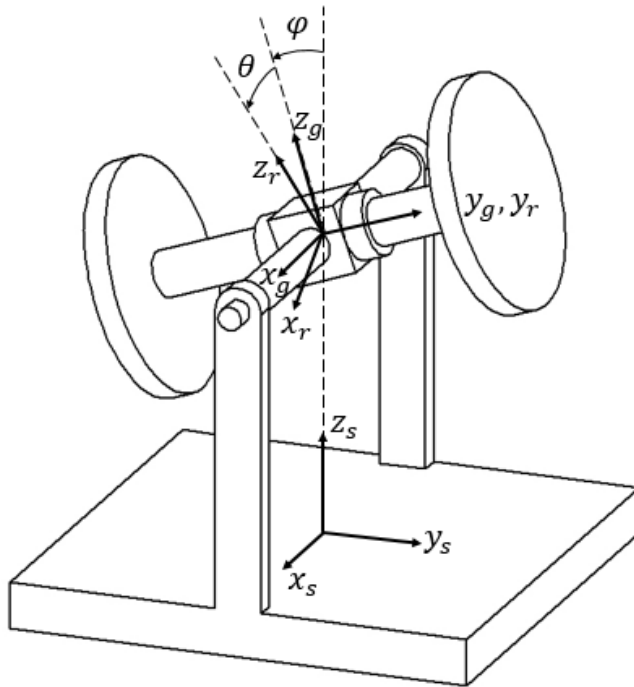


Figure 2.1. Rotor, Gimbal and Spacecraft Body Configuration and Respective Coordinate Systems

2.4. Sense of Motion

Gimbal (φ) and rotor (θ) angular motion are defined by the following oscillatory functions, respectively:

$$\begin{aligned}\varphi(t) &= \Phi \sin(2\pi ft) \\ \theta(t) &= \Theta \sin(2\pi ft + \sigma)\end{aligned}\quad (2.1)$$

Here, f is the excitation frequency and σ is the phase difference between the gimbal and rotor angular motion. Φ is assumed to be the maximum gimbal angle whereas Θ is the maximum angle for the rotor. Note that, neither the gimbal nor the rotor carries out a complete rotation, instead they only oscillate rotationally. The sense of motion is exhibited in Figure 2.2 for more detailed elaboration:

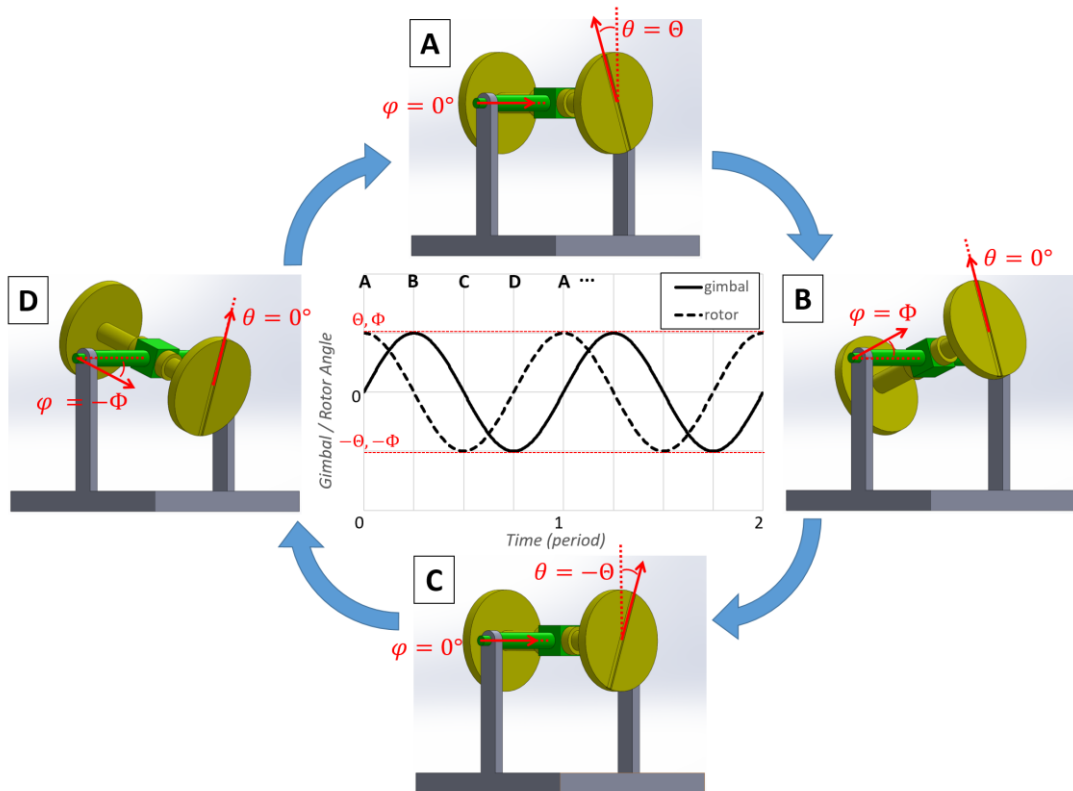


Figure 2.2. The Complete Motion Cycle for the Vibration Based Satellite Attitude Actuator

The motion of the actuator is provided for two complete cycles in the preceding figure. The plot in the center describes the angular motion of the gimbal and rotor; they carry out sinusoidal rotational motion with amplitudes Φ and θ , respectively. Note that, for this particular example, the rotor motion is assumed to be lagging the gimbal motion with a phase difference of $\pi/2$. The instances from the actuation cycle are exhibited as states from A to D. Their points of occurrence are also indicated on the plot. The actuator starts from state A and cycles through states A to D and again concludes at state A. The same motion is carried out in the next cycle. In the upcoming sections, the influence of such a motion on the host spacecraft will be investigated through conservation of angular motion.

2.5. Vector Equations

Under this topic, vector expressions for the system angular momentum is introduced followed by the equations of motion.

2.5.1. Angular Momentum

The angular momentum for the vibration based actuator can be described as the total of rotor and gimbal angular momentum.

$$\vec{H}_{VBA} = \vec{H}_g + \vec{H}_r \quad (2.2)$$

Angular momentum of the total actuator-spacecraft system can in turn be described by:

$$\vec{H}_{Total} = \vec{H}_s + \vec{H}_{SCA} \quad (2.3)$$

The angular velocities of the gimbal and rotor with respect to inertial frame can be represented by using main body angular velocity and relative angular velocities. For the gimbal:

$$\vec{\omega}_{g/i} = \vec{\omega}_{s/i} + \vec{\omega}_{g/s} \quad (2.4)$$

Similarly, for the rotor:

$$\vec{\omega}_{r/i} = \vec{\omega}_{s/i} + \vec{\omega}_{g/s} + \vec{\omega}_{r/g} \quad (2.5)$$

In this case, the angular momentum expression for the VBA becomes:

$$\vec{H}_{VBA} = \check{J}_g \cdot (\vec{\omega}_{s/i} + \vec{\omega}_{g/s}) + \check{J}_r \cdot (\vec{\omega}_{s/i} + \vec{\omega}_{g/s} + \vec{\omega}_{r/g}) \quad (2.6)$$

For the spacecraft main body

$$\vec{H}_s = \check{J}_s \cdot \vec{\omega}_{s/i} \quad (2.7)$$

Writing the angular momentum expression for the whole system and rearranging:

$$\vec{H}_{Total} = (\check{J}_s + \check{J}_g + \check{J}_r) \cdot \vec{\omega}_{s/i} + (\check{J}_g + \check{J}_r) \cdot \vec{\omega}_{g/s} + \check{J}_r \cdot \vec{\omega}_{r/g} \quad (2.8)$$

2.5.2. Equation of Motion

To obtain the Euler equation for the system, Eq. (2.8) is differentiated with respect to the inertial frame,

$$\vec{\tau}_{ext} = \frac{d}{dt} (\vec{H}_{Total})_i = \frac{d}{dt} (\vec{H}_s)_i + \frac{d}{dt} (\vec{H}_g)_i + \frac{d}{dt} (\vec{H}_r)_i \quad (2.9)$$

The expression for the satellite main body is straightforward and well known

$$\frac{d}{dt} (\vec{H}_s)_i = \check{J}_s \cdot \vec{\alpha}_{s/i} + \vec{\omega}_{s/i} \times \check{J}_s \cdot \vec{\omega}_{s/i} \quad (2.10)$$

The expression for gimbal becomes:

$$\frac{d}{dt} (\vec{H}_g)_i = \check{J}_g \cdot \frac{d}{dt} (\vec{\omega}_{s/i} + \vec{\omega}_{g/s})_i + (\vec{\omega}_{s/i} + \vec{\omega}_{g/s}) \times \check{J}_g \cdot (\vec{\omega}_{s/i} + \vec{\omega}_{g/s}) \quad (2.11)$$

Upon evaluation:

$$\begin{aligned} \frac{d}{dt} (\vec{H}_g)_i &= \check{J}_g \cdot (\vec{\alpha}_{s/i} + \vec{\alpha}_{g/s} + \vec{\omega}_{s/i} \times \vec{\omega}_{g/s}) \\ &\quad + (\vec{\omega}_{s/i} + \vec{\omega}_{g/s}) \times \check{J}_g \cdot (\vec{\omega}_{s/i} + \vec{\omega}_{g/s}) \end{aligned} \quad (2.12)$$

Similarly, for the rotor:

$$\begin{aligned} \frac{d}{dt}(\vec{H}_r)_i &= \check{J}_r \cdot (\vec{\alpha}_{s/i} + \vec{\alpha}_{g/s} + \vec{\alpha}_{r/g} + \vec{\omega}_{s/i} \times (\vec{\omega}_{g/s} + \vec{\omega}_{r/g}) + \vec{\omega}_{g/s} \\ &\quad \times \vec{\omega}_{r/g}) \\ &+ (\vec{\omega}_{s/i} + \vec{\omega}_{g/s} + \vec{\omega}_{r/g}) \times \check{J}_r \cdot (\vec{\omega}_{s/i} + \vec{\omega}_{g/s} + \vec{\omega}_{r/g}) \end{aligned} \quad (2.13)$$

Collecting all the terms such that:

$$\vec{\tau}_{ext} = \frac{d}{dt}(\vec{H}_{Total})_i = \frac{d}{dt}(\vec{H}_s)_i + \frac{d}{dt}(\vec{H}_g)_i + \frac{d}{dt}(\vec{H}_r)_i \quad (2.14)$$

Which becomes:

$$\begin{aligned} &\check{J}_s \cdot \vec{\alpha}_{s/i} + \vec{\omega}_{s/i} \times \check{J}_s \cdot \vec{\omega}_{s/i} \\ &+ \check{J}_g \cdot (\vec{\alpha}_{s/i} + \vec{\alpha}_{g/s} + \vec{\omega}_{s/i} \times \vec{\omega}_{g/s}) + (\vec{\omega}_{s/i} + \vec{\omega}_{g/s}) \times \check{J}_g \cdot (\vec{\omega}_{s/i} + \vec{\omega}_{g/s}) \\ &+ \check{J}_r \cdot (\vec{\alpha}_{s/i} + \vec{\alpha}_{g/s} + \vec{\alpha}_{r/g} + \vec{\omega}_{s/i} \times (\vec{\omega}_{g/s} + \vec{\omega}_{r/g}) + \vec{\omega}_{g/s} \times \vec{\omega}_{r/g}) \\ &+ (\vec{\omega}_{s/i} + \vec{\omega}_{g/s} + \vec{\omega}_{r/g}) \times \check{J}_r \cdot (\vec{\omega}_{s/i} + \vec{\omega}_{g/s} + \vec{\omega}_{r/g}) = \vec{\tau}_{ext} \end{aligned} \quad (2.15)$$

Collecting the dyadic terms for satellite inertia from eq. (2.15)

$$\check{J}_{sat} = \check{J}_s + \check{J}_g + \check{J}_r \quad (2.16)$$

rearranging the equations:

$$\begin{aligned} &\check{J}_{sat} \cdot \vec{\alpha}_{s/i} + \vec{\omega}_{s/i} \times \check{J}_{sat} \cdot \vec{\omega}_{s/i} \\ &= \vec{\tau}_{ext} - \check{J}_g \cdot (\vec{\alpha}_{g/s} + \vec{\omega}_{s/i} \times \vec{\omega}_{g/s}) \\ &- \vec{\omega}_{s/i} \times \check{J}_g \cdot \vec{\omega}_{g/s} - \vec{\omega}_{g/s} \times \check{J}_g \cdot (\vec{\omega}_{s/i} + \vec{\omega}_{g/s}) \\ &- \check{J}_r \cdot (\vec{\alpha}_{g/s} + \vec{\alpha}_{r/g} + \vec{\omega}_{s/i} \times (\vec{\omega}_{g/s} + \vec{\omega}_{r/g}) + \vec{\omega}_{g/s} \times \vec{\omega}_{r/g}) \\ &- \vec{\omega}_{s/i} \times \check{J}_r \cdot (\vec{\omega}_{g/s} + \vec{\omega}_{r/g}) - (\vec{\omega}_{g/s} + \vec{\omega}_{r/g}) \times \check{J}_r \cdot (\vec{\omega}_{s/i} + \vec{\omega}_{g/s} + \vec{\omega}_{r/g}) \end{aligned} \quad (2.17)$$

Next, collecting the dyadic terms for the total gimbal inertia

$$\check{J}_{gim} = \check{J}_g + \check{J}_r \quad (2.18)$$

Hence, the expression for the motion of a satellite with a CMG becomes:

$$\begin{aligned}
& \check{J}_{sat} \cdot \vec{\alpha}_{s/i} + \vec{\omega}_{s/i} \times \check{J}_{sat} \cdot \vec{\omega}_{s/i} \\
&= \vec{\tau}_{ext} - \check{J}_{gim} \cdot (\vec{\alpha}_{g/s} + \vec{\omega}_{s/i} \times \vec{\omega}_{g/s}) \\
&\quad - \vec{\omega}_{s/i} \times \check{J}_{gim} \cdot \vec{\omega}_{g/s} - \vec{\omega}_{g/s} \times \check{J}_{gim} \cdot (\vec{\omega}_{s/i} + \vec{\omega}_{g/s}) \\
&\quad - \check{J}_r \cdot (\vec{\alpha}_{r/g} + (\vec{\omega}_{s/i} + \vec{\omega}_{g/s}) \times \vec{\omega}_{r/g}) - (\vec{\omega}_{s/i} + \vec{\omega}_{g/s}) \times \check{J}_r \cdot \vec{\omega}_{r/g} \\
&\quad - \vec{\omega}_{r/g} \times \check{J}_r \cdot (\vec{\omega}_{s/i} + \vec{\omega}_{g/s} + \vec{\omega}_{r/g})
\end{aligned} \tag{2.19}$$

In order to elaborate on the physical significance of the above expression, first let us assume momentarily that there is no rotor and only the gimbal is rotating.

$$\begin{aligned}
& \check{J}_{sat} \cdot \vec{\alpha}_{s/i} + \vec{\omega}_{s/i} \times \check{J}_{sat} \cdot \vec{\omega}_{s/i} \\
&= \vec{\tau}_{ext} \\
&\quad - \check{J}_{gim} \cdot \vec{\alpha}_{g/s} - \vec{\omega}_{g/s} \times \check{J}_{gim} \cdot \vec{\omega}_{g/s} \\
&\quad - \vec{\omega}_{s/i} \times \check{J}_{gim} \cdot \vec{\omega}_{g/s} \\
&\quad - \check{J}_{gim} \cdot (\vec{\omega}_{s/i} \times \vec{\omega}_{g/s}) - \vec{\omega}_{g/s} \times \check{J}_{gim} \cdot \vec{\omega}_{s/i}
\end{aligned} \tag{2.20}$$

Here the physical insights regarding the right hand side expressions can be presented as follows; below term is only related to the motion of the gimbal. Hence, we can deduce that it is the part that results from the gimbal motor actuation

$$\check{J}_{gim} \cdot \vec{\alpha}_{g/s} + \vec{\omega}_{g/s} \times \check{J}_{gim} \cdot \vec{\omega}_{g/s} = \vec{\tau}_{gim}^{mot} \tag{2.21}$$

The gimbal angular velocity can lead to a gyroscopic torque through coupling with satellite angular velocity:

$$\vec{\omega}_{s/i} \times \check{J}_{gim} \cdot \vec{\omega}_{g/s} = \vec{\tau}_{gim}^{gyr} \tag{2.22}$$

by taking this into account in the control, the gyroscopic torque can be dealt with algorithms (via feed forwarding, etc.) which is common in reaction wheel implementation in satellites. The last term remaining is:

$$\check{J}_{gim} \cdot (\vec{\omega}_{s/i} \times \vec{\omega}_{g/s}) + \vec{\omega}_{g/s} \times \check{J}_{gim} \cdot \vec{\omega}_{s/i} = \vec{\tau}_{gim}^{asy} \tag{2.23}$$

It can be shown this term equals to zero when the inertia matrix is axisymmetric (refer to section 2.7 for more elaborate discussion on rotor and gimbal inertia selection).

Hence, the overall expression can be summarized as:

$$\check{J}_{sat} \cdot \vec{\alpha}_{s/i} + \vec{\omega}_{s/i} \times \check{J}_{sat} \cdot \vec{\omega}_{s/i} = \vec{\tau}_{ext} - \vec{\tau}_{gim}^{mot} - \vec{\tau}_{gim}^{gyr} - \vec{\tau}_{gim}^{asy} \quad (2.24)$$

Similarly, carrying out the same analysis this time with rotor and rearranging, one obtains:

$$\begin{aligned} & \check{J}_{sat} \cdot \vec{\alpha}_{s/i} + \vec{\omega}_{s/i} \times \check{J}_{sat} \cdot \vec{\omega}_{s/i} \\ &= \vec{\tau}_{ext} - \vec{\tau}_{gim}^{mot} - \vec{\tau}_{gim}^{gyr} - \vec{\tau}_{gim}^{asy} - \vec{\tau}_{rot}^{mot} - \vec{\tau}_{rot}^{gyr} - \vec{\tau}_{rot}^{cmg} - \vec{\tau}_{rot}^{asy} \end{aligned} \quad (2.25)$$

deducing that the following expression is due to the rotor motor actuation and naming it accordingly,

$$\check{J}_r \cdot \vec{\alpha}_{r/g} + \vec{\omega}_{r/g} \times \check{J}_r \cdot \vec{\omega}_{r/g} = \vec{\tau}_{rot}^{mot} \quad (2.26)$$

Similar to the previous case, the gyroscopic torque due to satellite motion

$$\vec{\omega}_{s/i} \times \check{J}_r \cdot \vec{\omega}_{r/g} = \vec{\tau}_{rot}^{gyr} \quad (2.27)$$

unlike the previous case, there also is gyroscopic torque due to the coupling of gimbal and rotor angular velocities. This actually is the definition for the output of a classical single-axis CMG:

$$\vec{\omega}_{g/s} \times \check{J}_r \cdot \vec{\omega}_{r/g} = \vec{\tau}_{cmg} \quad (2.28)$$

And similarly, the disturbance torque due to rotor asymmetry can be formulated as:

$$\check{J}_r \cdot ((\vec{\omega}_{s/i} + \vec{\omega}_{g/s}) \times \vec{\omega}_{r/g}) + \vec{\omega}_{r/g} \times \check{J}_r \cdot (\vec{\omega}_{s/i} + \vec{\omega}_{g/s}) = \vec{\tau}_{rot}^{asy} \quad (2.29)$$

Hence, Eq. (2.19) can be represented in a more succinct form as,

$$\check{J}_{sat} \vec{\alpha}_{s/i} + \vec{\omega}_{s/i} \times \check{J}_{sat} \vec{\omega}_{s/i} = \vec{\tau}_{ext} - \vec{\tau}_{VBA} \quad (2.30)$$

Where, the relationship describing the resulting total VBA torque can be described as:

$$\vec{\tau}_{VBA} = \vec{\tau}_{gim}^{mot} + \vec{\tau}_{gim}^{gyr} + \vec{\tau}_{gim}^{asy} + \vec{\tau}_{rot}^{mot} + \vec{\tau}_{rot}^{gyr} + \vec{\tau}_{cmg} + \vec{\tau}_{rot}^{asy} \quad (2.31)$$

2.6. Matrix Formulation

Previous equations have to be re-written in matrix form in order to be utilized in calculations; but beforehand, the representation frames for the vector variables have

to be determined. It is decided to represent the inertia dyadic, angular velocity and angular acceleration vectors of a body in its own body fixed frame. Relative angular velocities and acceleration vectors are expressed in the following body's frame (*i.e.* for the rotor-gimbal joint, the vectors $\vec{\omega}_{r/g}$ and $\vec{\alpha}_{r/g}$ will be represented in the rotor frame). Table 2.1 informs us regarding the coordinate frames in which the vector variables are expressed:

Table 2.1. *Coordinate Frame Associations of Dyadics and Vectors*

Frame	<i>Spacecraft Body</i>	<i>Gimbal</i>	<i>Rotor</i>
Symbol	S	g	r
inertia	\check{J}_s	\check{J}_g	\check{J}_r
velocity	$\vec{\omega}_{s/i}$	$\vec{\omega}_{g/i}, \vec{\omega}_{g/s}$	$\vec{\omega}_{r/i}, \vec{\omega}_{r/g}$
acceleration	$\vec{\alpha}_{s/i}$	$\vec{\alpha}_{g/i}, \vec{\alpha}_{g/s}$	$\vec{\alpha}_{r/i}, \vec{\alpha}_{r/g}$
torque	$\vec{\tau}_{ext}$	$\vec{\tau}_{gim}^{mot}, \vec{\tau}_{gim}^{gyr}, \vec{\tau}_{gim}^{asy}$	$\vec{\tau}_{rot}^{mot}, \vec{\tau}_{rot}^{gyr}, \vec{\tau}_{rot}^{asy}$

During the transformation from vector to matrix equations, an equivalent operation for cross product is defined via utilization of skew symmetric matrix:

$$(\bar{x})^\times = \begin{bmatrix} 0 & -x_3 & x_2 \\ x_3 & 0 & -x_1 \\ -x_2 & x_1 & 0 \end{bmatrix} \quad (2.32)$$

The matrices transforming from the coordinate frame of F_g to the coordinate frame of F_s is obtained using gimbal angle φ and can be expressed as:

$$\hat{C}_{s/g} = \begin{bmatrix} 1 & 0 & 0 \\ 0 & \cos(\varphi) & -\sin(\varphi) \\ 0 & \sin(\varphi) & \cos(\varphi) \end{bmatrix} \quad (2.33)$$

Utilizing small angle assumption, the above DCM takes the following form

$$\hat{C}_{s/g} = \begin{bmatrix} 1 & 0 & 0 \\ 0 & 1 & -\varphi \\ 0 & \varphi & 1 \end{bmatrix} \quad (2.34)$$

Additionally, being orthogonal, inverses of transformation matrices are their transposes. Hence,

$$\hat{C}_{g/s} = \hat{C}_{s/g}^{-1} = \hat{C}_{s/g}^T = \begin{bmatrix} 1 & 0 & 0 \\ 0 & 1 & \varphi \\ 0 & -\varphi & 1 \end{bmatrix} \quad (2.35)$$

Similarly, DCMs transforming among gimbal frame F_g and rotor frame F_r can be described by:

$$\hat{C}_{g/r} = \begin{bmatrix} 1 & 0 & \theta \\ 0 & 1 & 0 \\ -\theta & 0 & 1 \end{bmatrix}, \hat{C}_{r/g} = \begin{bmatrix} 1 & 0 & -\theta \\ 0 & 1 & 0 \\ \theta & 0 & 1 \end{bmatrix} \quad (2.36)$$

Next, vector equations will be written in matrix form, in the relevant frames stated in Table 2.1. The angular momentum and Euler equations will be expressed in satellite main body frame F_s to prevent erroneous inter-frame operations.

2.6.1. Angular Momentum

In order to obtain the angular momentum expression for the VBA, Eq. (2.6) can be expressed in matrix form in the main body frame as:

$$\begin{aligned} \bar{H}_{VBA} = & \hat{C}_{s/g}\hat{J}_g\hat{C}_{g/s}(\bar{\omega}_{s/i} + \hat{C}_{s/g}\bar{\omega}_{g/s}) \\ & + \hat{C}_{s/r}\hat{J}_r\hat{C}_{r/s} \cdot (\bar{\omega}_{s/i} + \hat{C}_{s/g}\bar{\omega}_{g/s} + \hat{C}_{s/r}\bar{\omega}_{r/g}) \end{aligned} \quad (2.37)$$

in which the transformation matrices are already provided in Eqs. (2.35) and (2.36). The angular velocity of the host spacecraft can be defined as:

$$\bar{\omega}_{s/i} = \begin{bmatrix} \omega_x \\ \omega_y \\ \omega_z \end{bmatrix} \quad (2.38)$$

As mentioned earlier, the gimbal axis is aligned with the x- axis of the host spacecraft. Under such conditions, the gimbal angular velocity with respect to the spacecraft in column matrix form is:

$$\bar{\omega}_{g/s} = \begin{bmatrix} \dot{\phi} \\ 0 \\ 0 \end{bmatrix} \quad (2.39)$$

Similarly, for the rotor:

$$\bar{\omega}_{r/g} = \begin{bmatrix} 0 \\ \dot{\theta} \\ 0 \end{bmatrix} \quad (2.40)$$

Furthermore, the gimbal inertia can be given as (recall that the body axes are assumed to be coincident with the principal axes and the gimbal is axisymmetric in the x-direction):

$$\hat{J}_g = \begin{bmatrix} J_g^x & 0 & 0 \\ 0 & J_g^y & 0 \\ 0 & 0 & J_g^z \end{bmatrix} \quad (2.41)$$

Similarly, for the rotor:

$$\hat{J}_r = \begin{bmatrix} J_r^x & 0 & 0 \\ 0 & J_r^y & 0 \\ 0 & 0 & J_r^z \end{bmatrix} \quad (2.42)$$

Inserting Eqs. from (2.38) to (2.42) into Eq. (2.37) and assuming higher order terms are zero (i.e. $\varphi^2, \varphi^3, \varphi^4, \theta^2, \theta^3 = 0$) via small angle assumption, the following approximation of the VBA angular momentum is obtained.

$$\bar{H}_{VBA} = \left[\begin{array}{l} (\varphi\omega_y - \omega_z)(J_r^x - J_r^z)\theta + (\omega_x + \dot{\phi})(J_r^x + J_g^x) \\ \{(\omega_x + \dot{\phi})(J_r^x - J_r^z)\theta + \omega_z(J_r^y + J_g^y - J_r^z - J_g^z)\}\varphi + (J_r^y + J_g^y)\omega_y + J_r^y\dot{\theta} \\ \{(J_r^y + J_g^y - J_r^z - J_g^z)\omega_y + J_r^y\dot{\theta}\}\varphi - (\omega_x + \dot{\phi})(J_r^x - J_r^z)\theta + (J_r^z + J_g^z)\omega_z \end{array} \right] \quad (2.43)$$

Gimbal and rotor angles have already been defined in Eq. (2.1). Consequently, their derivatives can be obtained as:

$$\begin{aligned} \dot{\phi}(t) &= 2\pi f \Phi \cos(2\pi ft) \\ \dot{\theta}(t) &= 2\pi f \Theta \cos(2\pi ft + \sigma) \end{aligned} \quad (2.44)$$

For the time being, further assuming higher order terms and spacecraft angular velocities to be zero (*i.e.* $\omega_x, \omega_y, \omega_z = 0$) and inserting Eqs. (2.1) and (2.44) into Eq. (2.43):

$$\bar{H}_{VBA} \cong \begin{bmatrix} (J_r^x + J_g^x)2\pi f\Phi \cos(2\pi ft) \\ (2J_r^y)2\pi f\Theta \cos(2\pi ft + \sigma) \\ -\pi f\Phi\Theta\{(J_r^x - J_r^y - J_r^z)\sin(4\pi ft + \sigma) + (J_r^x + J_r^y - J_r^z)\sin(\sigma)\} \end{bmatrix} \quad (2.45)$$

Several interesting traits are evident in Eq. (2.45). The angular momentum generated by the device in the x- and y- axes of the spacecraft frame are sinusoidal; yet the angular momentum in the spacecraft z- axis has both sinusoidal and constant components, which is defined by the phase difference angle σ . Also of note is the doubling of the frequency for the sinusoidal part of the z- axis output. Additionally, the z- axis output is solely dependent on the rotor moment of inertia and irrespective of the gimbal properties and also smaller in magnitude due to the inclusion of the magnitude product $\Phi\Theta$.

2.6.2. Torque Expressions

The aim of this subsection is to write the elements of expression in Eq. (2.31) in matrix form. As it can be observed from the section 2.5.2, torque expressions encountered in the equations of motion involve vectors for angular acceleration of the bodies. Similar to Eqs. (2.39) and (2.40), these can be written as:

$$\ddot{\alpha}_{g/s} = \begin{bmatrix} \ddot{\varphi} \\ 0 \\ 0 \end{bmatrix} \quad (2.46)$$

Similarly, for the rotor:

$$\ddot{\alpha}_{r/g} = \begin{bmatrix} 0 \\ \ddot{\theta} \\ 0 \end{bmatrix} \quad (2.47)$$

Recalling Eq. (2.44), the angular acceleration for sinusoidal motion can be quantified as:

$$\begin{aligned} \ddot{\varphi}(t) &= -4\pi^2 f^2 \Phi \sin(2\pi ft) \\ \ddot{\theta}(t) &= -4\pi^2 f^2 \Theta \sin(2\pi ft + \sigma) \end{aligned} \quad (2.48)$$

Starting off with the expression in Eq. (2.12):

$$\begin{aligned}\bar{\tau}_{gim}^{mot} = & (\hat{C}_{s/g}\hat{J}_g\hat{C}_{g/s} + \hat{C}_{s/r}\hat{J}_r\hat{C}_{r/s})\hat{C}_{s/g}\bar{\alpha}_{g/s} \\ & + (\hat{C}_{s/g}\bar{\omega}_{g/s})^\times \{(\hat{C}_{s/g}\hat{J}_g\hat{C}_{g/s} + \hat{C}_{s/r}\hat{J}_r\hat{C}_{r/s})(\hat{C}_{s/g}\bar{\omega}_{g/s})\}\end{aligned}\quad (2.49)$$

inserting the expressions for the angular acceleration and assuming higher order terms to be zero, Eq. (2.49) takes the following form

$$\bar{\tau}_{gim}^{mot} \cong \begin{bmatrix} (J_r^x + J_g^x)\ddot{\varphi} \\ (J_r^x - J_r^z)\theta(\dot{\varphi}^2 + \varphi\ddot{\varphi}) \\ (J_r^x - J_r^z)\theta(\dot{\varphi}^2\varphi - \ddot{\varphi}) \end{bmatrix} \quad (2.50)$$

For the expression in Eq. (2.14):

$$\bar{\tau}_{gim}^{gyr} = \bar{\omega}_{s/i}^\times \{(\hat{C}_{s/g}\hat{J}_g\hat{C}_{g/s} + \hat{C}_{s/r}\hat{J}_r\hat{C}_{r/s})(\hat{C}_{s/g}\bar{\omega}_{g/s})\} \quad (2.51)$$

Again, inserting the necessary expressions, simplifying and assuming higher order terms to be zero:

$$\bar{\tau}_{gim}^{gyr} \cong \begin{bmatrix} -(J_r^x - J_r^z)\dot{\varphi}\theta(\varphi\omega_z + \omega_y) \\ \{(J_r^x - J_r^z)\theta\omega_x + (J_g^x + J_r^x)\omega_z\}\dot{\varphi} \\ \{\varphi\theta(J_r^x - J_r^z)\omega_x - (J_g^x + J_r^x)\omega_y\}\dot{\varphi} \end{bmatrix} \quad (2.52)$$

Similarly, for Eq. (2.23),

$$\begin{aligned}\bar{\tau}_{gim}^{asy} = & (\hat{C}_{s/g}\hat{J}_g\hat{C}_{g/s} + \hat{C}_{s/r}\hat{J}_r\hat{C}_{r/s})(\bar{\omega}_{s/i}^\times \hat{C}_{s/g}\bar{\omega}_{g/s}) \\ & + (\hat{C}_{s/g}\bar{\omega}_{g/s})^\times \{(\hat{C}_{s/g}\hat{J}_g\hat{C}_{g/s} + \hat{C}_{s/r}\hat{J}_r\hat{C}_{r/s})\bar{\omega}_{s/i}\}\end{aligned}\quad (2.53)$$

Putting in the required expressions and further simplifying:

$$\bar{\tau}_{gim}^{asy} \cong \begin{bmatrix} (J_r^x - J_r^z)\dot{\varphi}\theta(\varphi\omega_z + \omega_y) \\ \dot{\varphi}(J_r^x - J_r^z)\theta\omega_x - \dot{\varphi}(J_g^y + J_r^y - J_g^z - J_r^z)\{2\varphi\omega_y - \omega_z\} \\ \dot{\varphi}(J_g^y + J_r^y - J_g^z - J_r^z)(\omega_y + 2\varphi\omega_z) + \dot{\varphi}(J_r^x - J_r^z)\theta\omega_x \end{bmatrix} \quad (2.54)$$

The CMG output in spacecraft frame can be obtained in matrix form by utilizing Eq. (2.28):

$$\bar{\tau}_{cmg} = (\hat{C}_{s/g}\bar{\omega}_{g/s})^\times \{(\hat{C}_{s/r}\hat{J}_r\hat{C}_{r/s})(\hat{C}_{s/r}\bar{\omega}_{r/g})\} \quad (2.55)$$

Substituting and simplifying:

$$\bar{\tau}_{cmg} \cong \begin{bmatrix} 0 \\ -\varphi J_r^y \dot{\phi} \dot{\theta} \\ J_r^y \dot{\phi} \dot{\theta} \end{bmatrix} \quad (2.56)$$

Moving on to the torque expressions for the rotor:

$$\bar{\tau}_{rot}^{mot} = (\hat{C}_{s/r} \hat{J}_r \hat{C}_{r/s}) (\hat{C}_{s/r} \bar{\alpha}_{r/g}) + (\hat{C}_{s/r} \bar{\omega}_{r/g})^\times \{(\hat{C}_{s/r} \hat{J}_r \hat{C}_{r/s}) (\hat{C}_{s/r} \bar{\omega}_{r/g})\} \quad (2.57)$$

Upon simplification takes the following form

$$\bar{\tau}_{rot}^{mot} \cong \begin{bmatrix} 0 \\ J_r^y \ddot{\theta} \\ \varphi J_r^y \ddot{\theta} \end{bmatrix} \quad (2.58)$$

Gyroscopic torque due to rotor and spacecraft

$$\bar{\tau}_{rot}^{gyr} = \bar{\omega}_{s/i}^\times \{(\hat{C}_{s/r} \hat{J}_r \hat{C}_{r/s}) (\hat{C}_{s/r} \bar{\omega}_{r/g})\} \quad (2.59)$$

Again, inserting the necessary expressions, simplifying and assuming higher order terms to be zero:

$$\bar{\tau}_{rot}^{gyr} \cong \begin{bmatrix} J_r^y \dot{\theta} (\varphi \omega_y - \omega_z) \\ \varphi J_r^y \dot{\theta} \omega_x \\ J_r^y \dot{\theta} \omega_x \end{bmatrix} \quad (2.60)$$

Other terms

$$\begin{aligned} \bar{\tau}_{rot}^{asy} &= (\hat{C}_{s/r} \hat{J}_r \hat{C}_{r/s}) \{(\bar{\omega}_{s/i} + \hat{C}_{s/g} \bar{\omega}_{g/s})^\times (\hat{C}_{s/r} \bar{\omega}_{r/g})\} \\ &\quad + (\hat{C}_{s/r} \bar{\omega}_{r/g})^\times \{(\hat{C}_{s/r} \hat{J}_r \hat{C}_{r/s}) (\bar{\omega}_{s/i} + \hat{C}_{s/g} \bar{\omega}_{g/s})\} \end{aligned} \quad (2.61)$$

Putting in the required expressions and further simplifying:

$$\bar{\tau}_{rot}^{asy} \cong \begin{bmatrix} (J_r^x - J_r^z) \dot{\theta} (2\theta \omega_x + 2\theta \dot{\phi} - \varphi \omega_y + \omega_z) \\ \varphi (J_r^x - J_r^z) \dot{\theta} (2\theta \omega_z - 2\theta \varphi \omega_y - \omega_x - \dot{\phi}) \\ (J_r^x - J_r^z) \dot{\theta} (2\theta \omega_z - 2\theta \varphi \omega_y - \omega_x - \dot{\phi}) \end{bmatrix} \quad (2.62)$$

2.7. Shaping the Actuator

Close inspection of angular momentum expressions of Eqs. (2.43) and (2.45) as well as the torque expressions from Eq. (2.51) to Eq. (2.62) leads to following observations:

the main output is in the z- axis; rotor mass properties (*i.e.* inertia) dominate the functioning of the device (even though gimbal terms also exist); under non-stationary conditions (*i.e.* when spacecraft is in motion) the angular momentum and torque outputs of the device are heavily coupled with spacecraft angular velocity and as mentioned earlier, the sinusoidal component of the output angular momentum.

A remedy for this problem was proposed in Ref. [30], namely shaping this rotor in the form of a rod-like structure (Figure 2.3).

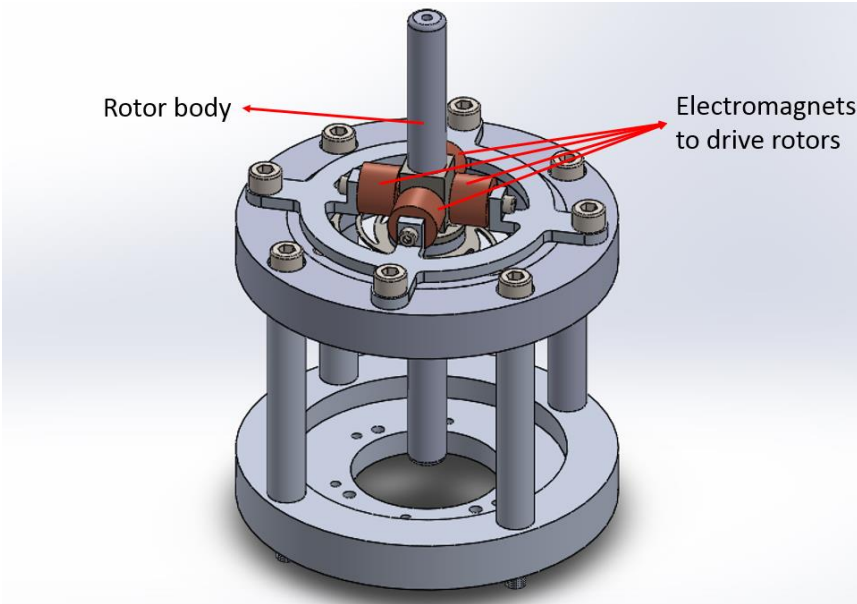


Figure 2.3. Rod Shaped VBA Implementation [30].

Recalling z- component of the VBA angular momentum output from Eq. (2.45),

$$\bar{H}_{SCA}^z \cong -\pi f \Phi \theta \{ (J_r^x - J_r^y - J_r^z) \sin(4\pi f t + \sigma) + (J_r^x + J_r^y - J_r^z) \sin(\sigma) \} \quad (2.63)$$

Note that the sinusoidal component has the expression $(J_r^x - J_r^y - J_r^z)$ for coefficient. Equating this coefficient to zero would theoretically cancel the sinusoidal z- axis component, leaving a constant angular momentum term dependent on the phase differences between gimbal and rotor oscillations. Assuming the following,

$$J_r^x = J_r^y + J_r^z \quad (2.64)$$

would result in,

$$\bar{H}_{rod}^z \cong -2\pi f \Phi \Theta J_r^y \sin(\sigma) \quad (2.65)$$

Note that Eq. (2.64), even though mathematically sound, is physically unrealizable. However, a practical realization can be obtained by having z- axis inertia J_r^z substantially smaller than J_r^x and J_r^y while also having it axisymmetric about the z-axis (*i.e.* $J_r^x \cong J_r^y$). This physically corresponds to a rod-like rotor structure which has its slender axis in the z- axis direction. Assuming such rod like structure with $J_r^x = J_r^y = J_{rod}$ as well as substantially smaller gimbal inertias, Eq. (2.45) takes the following form:

$$\bar{H}_{VBA} \cong \begin{bmatrix} 2\pi f \Phi J_{rod} \cos(2\pi f t) \\ 2\pi f \Theta J_{rod} \cos(2\pi f t + \sigma) \\ -2\pi f \Phi \Theta J_{rod} \sin(\sigma) \end{bmatrix} \quad (2.66)$$

Here, as expected, z- axis output becomes a constant term dependent on the phase difference between gimbal and rotor oscillations; however, x- and y- are stilll of sinusoidal nature. Note that the angular momentum takes its maximum value when the phase difference is odd multiples of $\pi/2$. Also of note, the angular momentum frequency at the z-axis (output axis) is twice the excitation frequency. To investigate the coupling between spacecraft and VBA motion, assume that the spacecraft angular velocity to be non-zero:

$$\bar{H}_{rod} \cong \begin{bmatrix} J_{rod}\{\theta(\varphi\omega_y - \omega_z) + \dot{\varphi} + \omega_x\} \\ J_{rod}\{\varphi(\theta\omega_x + \theta\dot{\varphi} + \omega_z) + \dot{\theta} + \omega_y\} \\ J_{rod}\{\theta(\theta\omega_z - \dot{\varphi} - \omega_x) + \varphi(\dot{\theta} + \omega_y)\} \end{bmatrix} \quad (2.67)$$

Inserting expressions from Eqs. (2.1) and (2.44) and further simplifying by assuming higher order terms to be zero

$$\bar{H}_{rod} \cong \begin{bmatrix} J_{rod} \left\{ \frac{1}{2} \theta \Phi \omega_y (\cos(\sigma) - \cos(4\pi f t + \sigma)) + 2\pi f \Phi \cos(2\pi f t) - \omega_z \theta \sin(2\pi f t + \sigma) \right\} + J_{rod} \omega_x \\ J_{rod} \left\{ \frac{1}{2} \theta \Phi \omega_x (\cos(\sigma) - \cos(4\pi f t + \sigma)) + 2\pi f \theta \cos(2\pi f t + \sigma) + \omega_z \Phi \sin(2\pi f t) \right\} + J_{rod} \omega_y \\ J_{rod} \left\{ \omega_y \Phi \sin(2\pi f t) - \omega_x \theta \sin(2\pi f t + \sigma) \right\} \\ -2\pi f \Phi \theta \sin(\sigma) \end{bmatrix} \quad (2.68)$$

Comparing and contrasting Eqs. (2.66) and (2.68), the heavy coupling with the spacecraft angular velocities are evident. Hence, even though only angular momentum in z- axis was the goal, a complex spacecraft motion may result. Note that the last terms in the x- and y- axes components are stemming from the rigid body motion of the spacecraft.

A remedy to this problem can be found by inspecting the Eq. (2.43), the coupling terms generally involve coefficients such as $J_r^x - J_r^z$ and $J_r^y + J_g^y - J_r^z - J_g^z$. Note that these terms are concerned with rotor and gimbal inertias. The first term vanishes if the rotor is axisymmetric in the y- axis. Similarly, the second term vanishes if both the rotor and gimbal becomes axisymmetric in the x- axis. Physically, this can be realized if gimbal is axisymmetric in x- axis direction and rotor is axisymmetric in both of the x- and y- axes which corresponds to a rod-like gimbal and sphere-like rotor.

We may calculate the output of such a device via assuming uniformly symmetric rotor inertia such that $J_r^{x,y,z} = J_{sph}$ and axis-symmetric gimbal inertia where $J_g^y = J_g^z$ while further assuming gimbal x- axis inertia is relatively small (*i.e.* $J_g^x \ll J_g^{y,z}$). The spherical rotor inertia may additionally be assumed to be substantially larger than the gimbal inertias ($J_{sph} \gg J_g^{y,z}$). Under such assumptions, the expression for angular momentum of a VBA having sphere-like rotor becomes:

$$\bar{H}_{sph} \cong \begin{bmatrix} J_{sph} 2\pi f \Phi \cos(2\pi ft) + J_{sph} \omega_x \\ J_{sph} 2\pi f \Theta \cos(2\pi ft + \sigma) + (J_{sph} + J_g^y) \omega_y \\ J_{sph} \pi f \Phi \theta \{ \sin(4\pi ft + \sigma) - \sin(\sigma) \} + (J_{sph} + J_g^y) \omega_z \end{bmatrix} \quad (2.69)$$

Note that no spacecraft angular velocity terms $\omega_{x,y,z}$ are present in Eq. (2.69) (except the rigid body motion terms), contrasting heavily with Eq. (2.68). This was achieved in the expanse of introduction of the sinusoid term $\sin(4\pi ft + \sigma)$ in the device output even though it still has the constant term $\sin(\sigma)$ dependent on the phase difference. Hence the spherical rotor offers actuator angular momentum decoupling from spacecraft angular velocity, yet its output is not constant as with the previous rod architecture. A depiction of an actuator with a spherical rotor is provided in Figure 2.4.

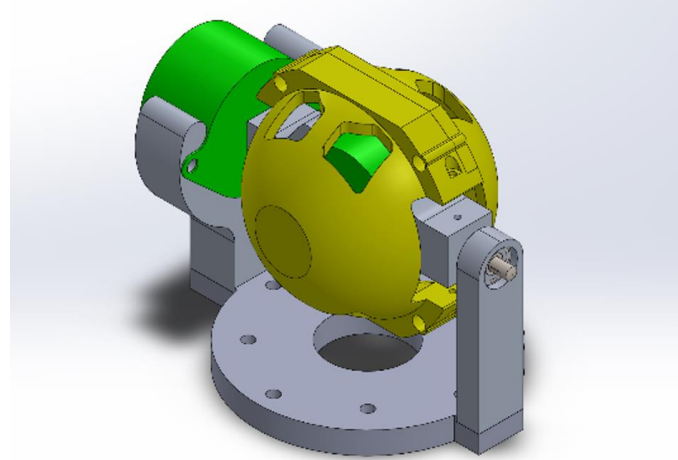


Figure 2.4. Proposed Design for a VBA with A Rotor Having Uniformly Distributed Inertia

Assuming the spherical rotor inertia (J_{sph}) to be $2.115\text{E-}4 \text{ kg}\cdot\text{m}^2$, gimbal inertia (J_g^y) to be $1.456\text{E-}4 \text{ kg}\cdot\text{m}^2$, excitation frequency as 15 Hz and the gimbal and rotor angle amplitudes as 5° ; the resulting VBA angular momentum can be numerically obtained by utilizing Eq. (2.69). Using these parameters, the angular momentum vector of the actuator for every time instant of the operation cycle can be plotted; providing us with

the locus of angular momentum vectors. Such a locus of vectors is presented in Figure 2.5 for a phase difference (σ) of -90° together with the curve representing the trace defined by the tip of the actuator's angular momentum vector. The axes correspond to the spacecraft body axes shown in Figure 2.1.

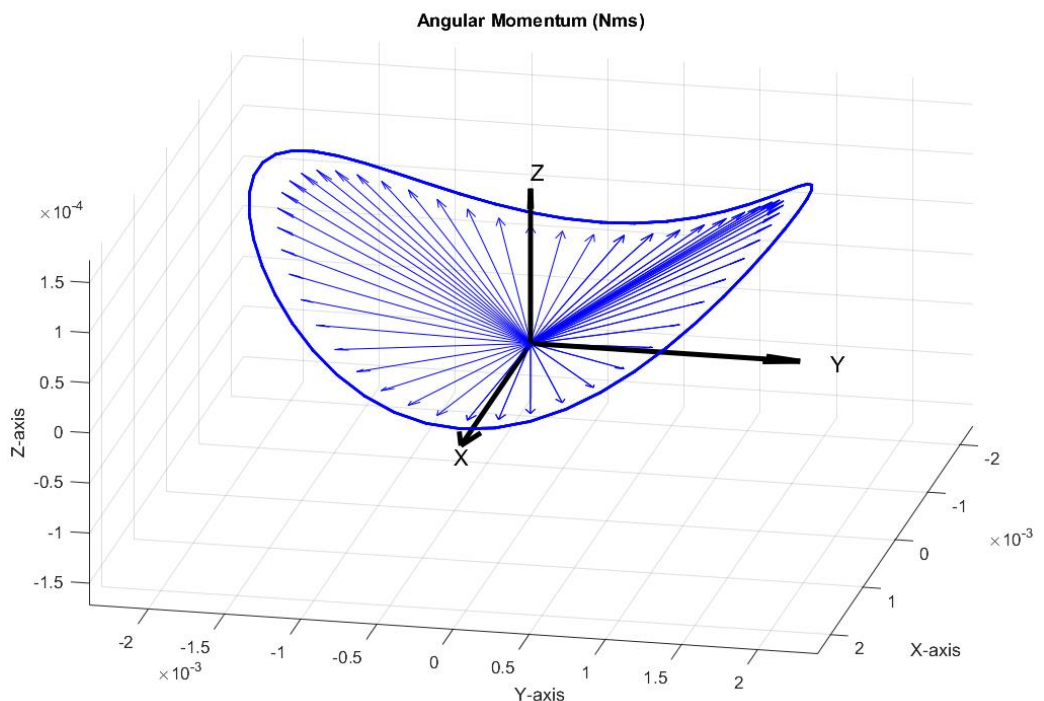


Figure 2.5. Locus of Angular Momentum Vector for $\sigma = -90^\circ$

Note that, the resulting curve is consistently above the x-y plane, therefore having a strictly positive angular momentum component in the z- axis throughout the actuator operation. This component leads to the net and unidirectional rotational motion around the z-axis upon completion of each actuation cycle described in Figure 2.2. The angular momentum locus takes the following form with the phase difference of 0° :

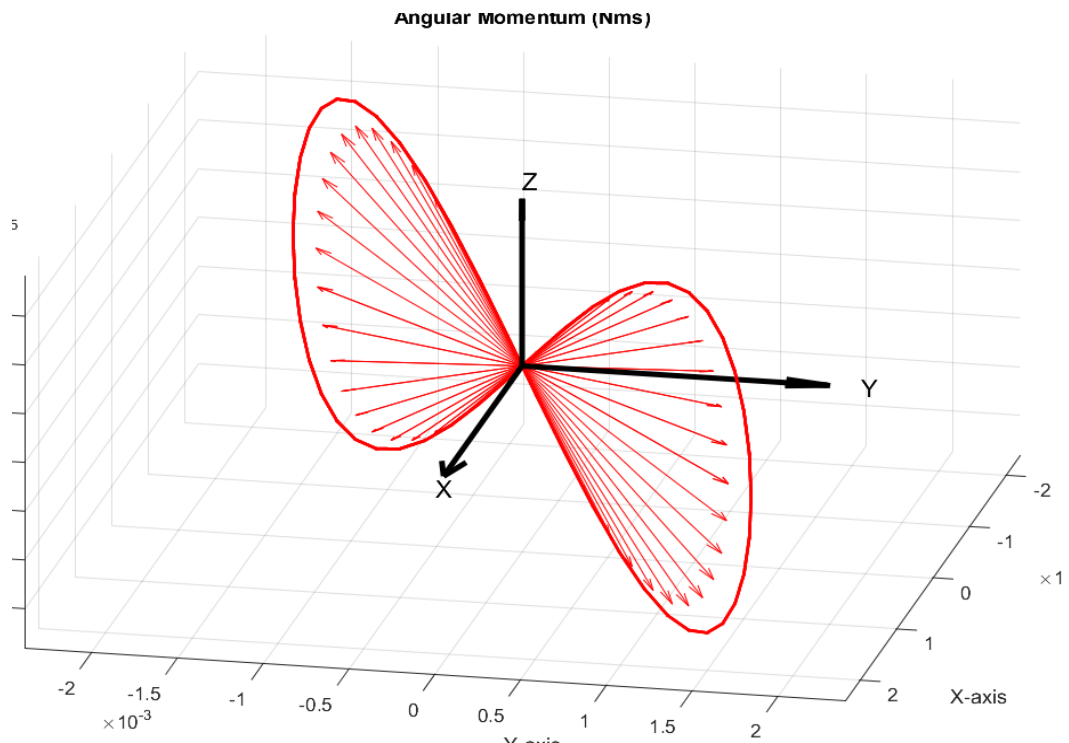


Figure 2.6. Locus of Angular Momentum Vector for $\sigma = 0^\circ$

In contrast with the Figure 2.5, this angular momentum locus is symmetrical with respect to the x-y plane. Thus, for every non-zero z- axis angular momentum vector component, there will exist an equal but opposite component below the x-y plane. Consequently, no net rotational motion will result upon the completion of actuation cycle. The evolution of angular momentum loci will be better understood with the comparison of different phase difference settings. Therefore, locus for different phase difference settings were obtained and plotted concurrently:

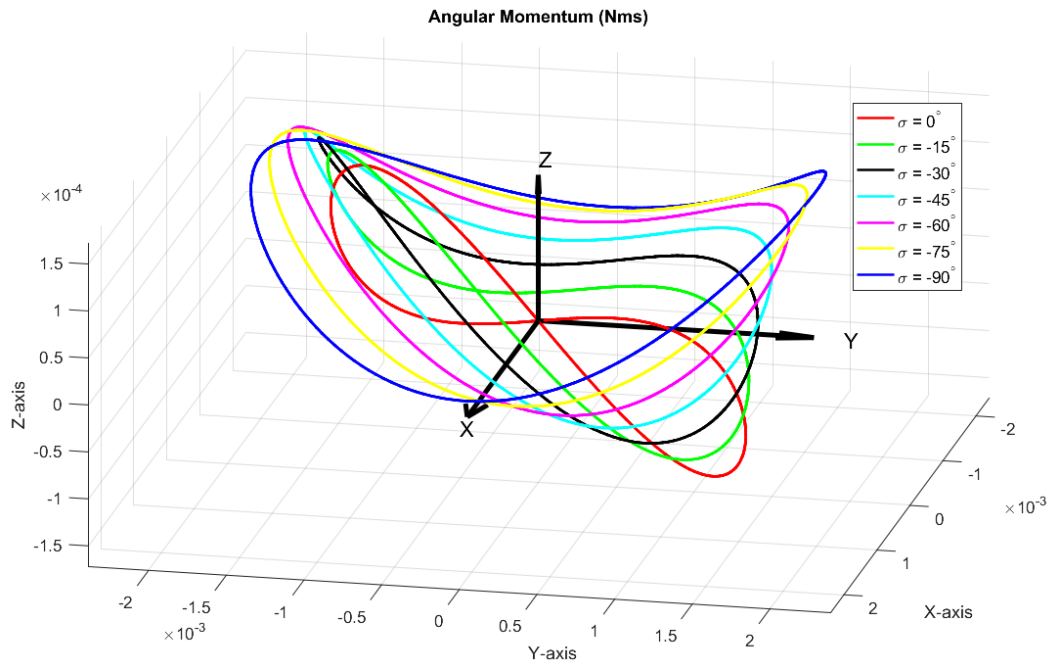


Figure 2.7. Evolution of Angular Momentum Loci from $\sigma = -90^\circ$ to $\sigma = 0^\circ$

As it can be observed from Figure 2.7, as the phase difference approaches to zero, the angular momentum locus becomes symmetrical with respect to the x-y axis with no net z- axis component upon completion of the actuation cycle. Hence, it can be concluded that phase difference σ can act as a modulating parameter capable of adjusting the amplitude of actuator's output. Furthermore, for positive phase difference settings, the angular momentum loci are obtained as:

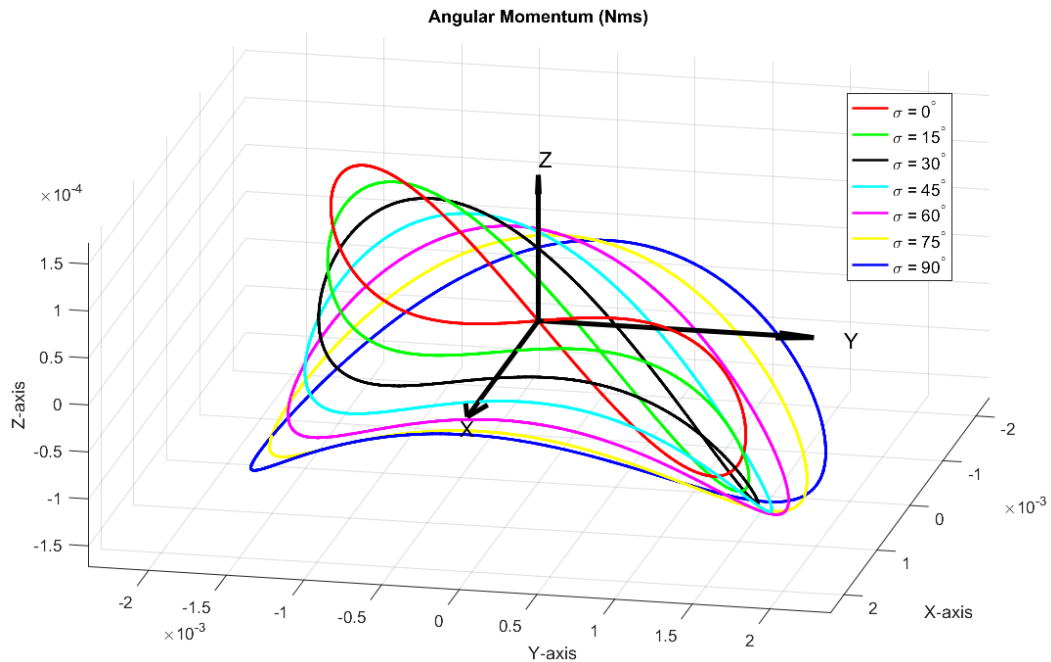


Figure 2.8. Locus of Angular Momentum Vector for $\sigma = 0^\circ$ to $\sigma = 90^\circ$

Here, it can be observed that, a locus very similar to the case with $\sigma = -90^\circ$ but in opposite direction is obtained. In this case, the z- axis component of the angular momentum locus is strictly negative; resulting in a curve consistently below the x-y plane. Consequently, the host spacecraft would likely to rotate with the same amount in $\sigma = -90^\circ$, but in the opposite sense. Hence, it can be concluded that phase difference setting can not only modulate the output amplitude of the actuator, but also is able to define the direction of the resulting motion.

In the following sections, simulations and the corresponding results from a prototype implementation of such an actuator will be presented.

CHAPTER 3

ACTUATOR DESIGN

3.1. Vibration Based Actuator (VBA) Architecture

The architecture of the prototype actuator is complex; spanning mechanical, electrical and software domains together with actuating and sensing elements. A functional block diagram of VBA is provided in Figure 3.1 to facilitate ease of understanding.

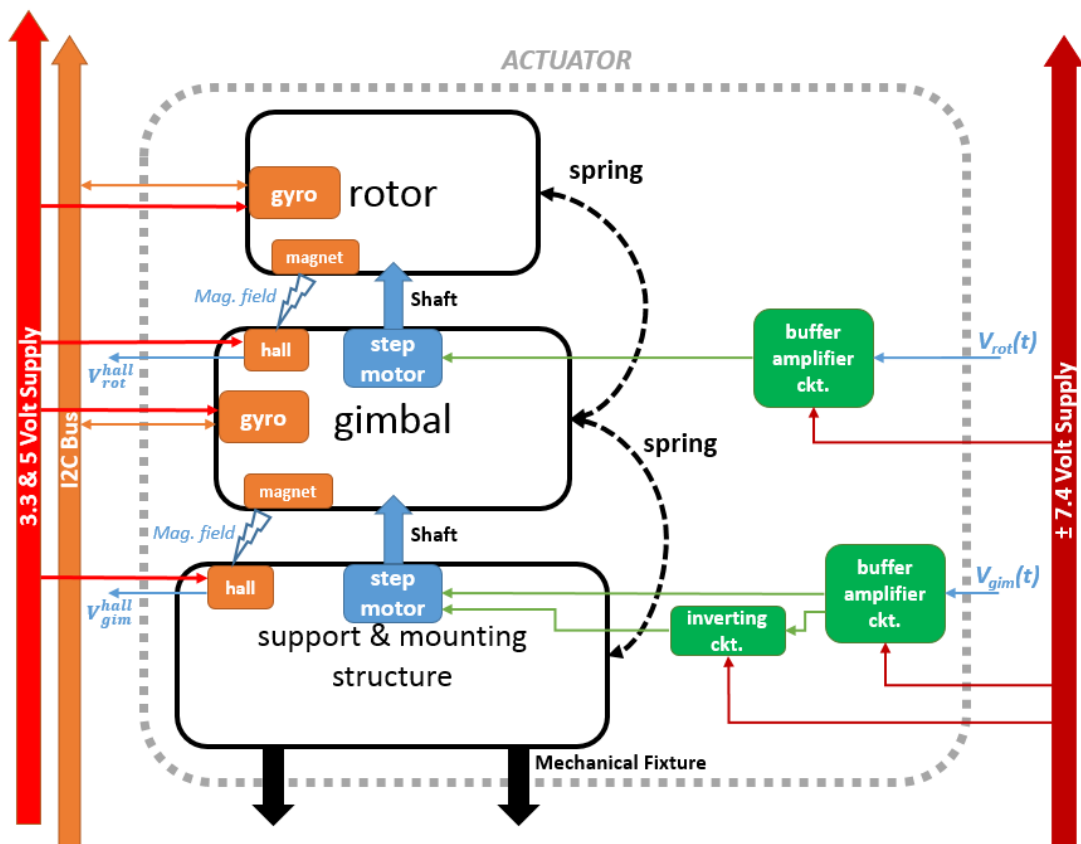


Figure 3.1. Actuator Architecture Together with Interfaces

The following color coding was utilized in Figure 3.1; color black correspond to mechanical elements, blue is used for the actuators, orange is for sensors and green is for circuitry. Furthermore, signal buses are colored in orange and the power buses are colored in shades of red.

The prototype actuator consists of a rotor, gimbal and supporting structure. The rotor is actuated by a unipolar stepper motor which itself is situated in the gimbal structure. Similarly, the gimbal is actuated through a bipolar stepper motor situated in the support structure. Stepper motors are not utilized in the traditional sense; instead their movements are mechanically confined within a single step in order to constraint them to oscillate within a predefined limit. Hence, not all of their coils are energized, the potential difference is applied to only selected coils to ensure in-step oscillation. The electrical component of the actuator is composed of the aforementioned motors and the circuitry that receives sinusoidal potential difference which are amplified to drive the stepper motors. Sensing is carried out by gyroscopes to measure angular rate and hall effect sensors for angular position.

The resulting implementation can be observed in Figure 3.2.

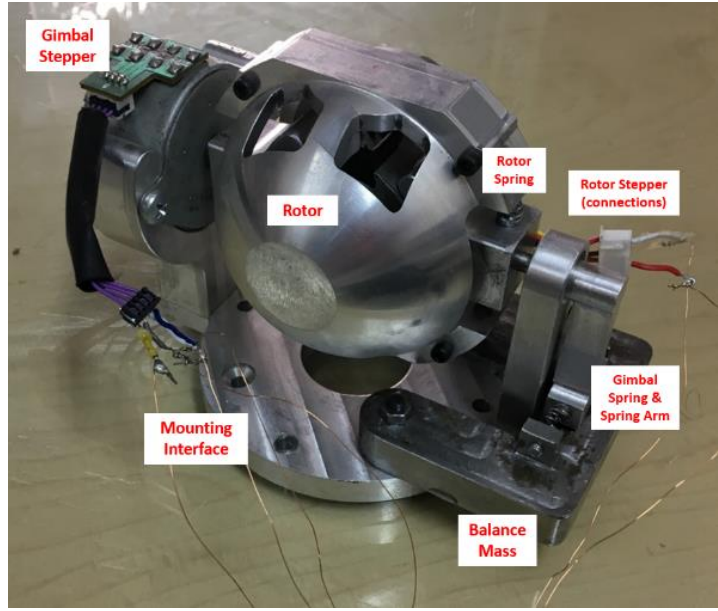


Figure 3.2. The Prototype Actuator

3.2. Mechanical Design

The actuator consists mainly of rotor, gimbal and supporting structures. Flexible connections (i.e. springs) exist between these elements. Details on these elements are subsequently provided.

3.2.1. Rotor and Gimbal Design

As mentioned back in section 2.7 Shaping the Actuator, a spherical rotor design is ideal for the minimization of disturbance.

Rotor design was the predominant effort in the overall actuator mechanical design. As outlined earlier in Eq. (2.69), a rotor with uniform inertia would be the ideal solution unsusceptible to angular velocity coupling. Thus the main requirement for the rotor design was to have a uniform inertia, which lead to the spherical shape of the rotor.

However, several solutions had to be formulated for the practical implementation of such a shape. Firstly, a spherical rotor cannot be implemented as a single part due to the integration as well as manufacturing constraints; you need access to the inside of the sphere to situate driving motor. Secondly, it had to have a cavity to make room for the gimbal. Therefore, the spherical rotor was designed as two distinct hollow hemispheres which will be assembled around the gimbal using connecting elements (*i.e.* nuts and bolts). Hemispheres are named as the “shaft side” and the “sensor side” hemisphere.

Openings are available for the gimbal to access the support structure from the front and back of the rotor. These openings are designed by taking the maximum rotational motion of the rotor into account. These openings also disturb the uniform inertia so, in order to remedy this, additional openings have been designed on the rotor and material had been hollowed out as it can be observed from Figure 3.3.

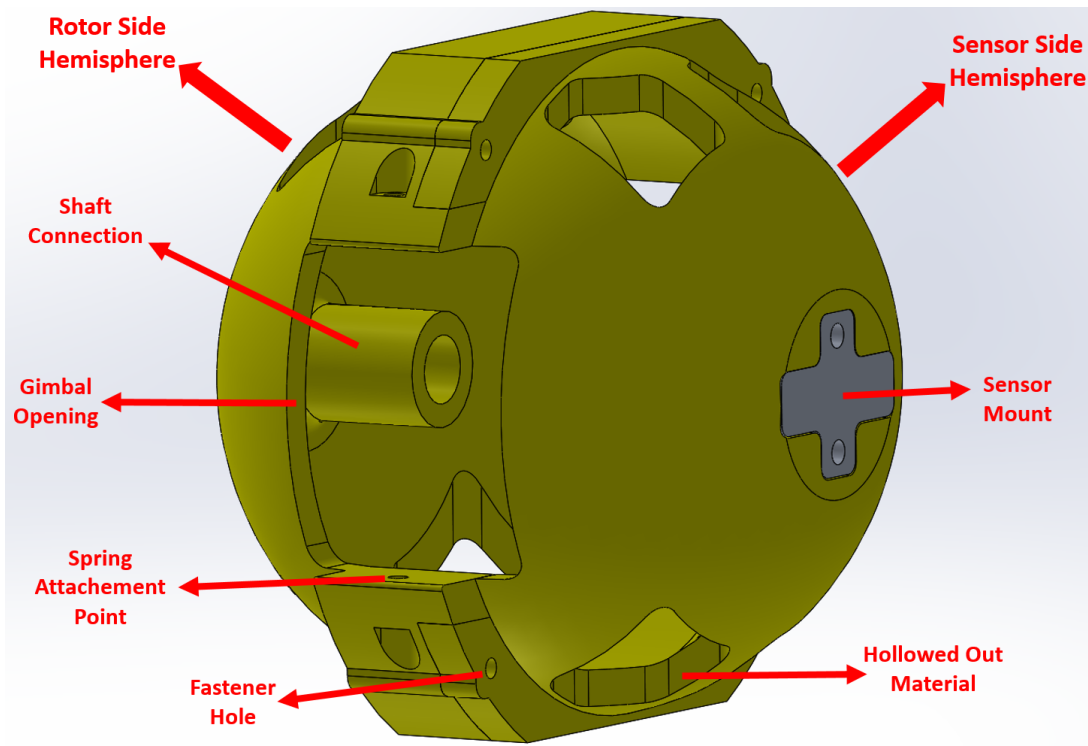


Figure 3.3. CAD Design of the Rotor

The “shaft side” hemisphere has a mechanical connection with the shaft side of the rotor motor and the “sensor side” hemisphere has a mechanical structure to ensure IMU mounting. These parts were machined from aluminum 6061 due to its availability and ease of manufacturing. Two hemispheres were machined separately by C-Y Axis CNC Mill machine. The hemispheres were also toleranced to have a tight fit with each other.



Figure 3.4. Manufactured Hemispheres

Gimbal design is straightforward in comparison with the rotor design. The function of the gimbal is to provide a rotating base for the rotor assembly; it has to have the ability to house the rotor motor and support the rotor structure. It is also connected to the support structures via bearings. On one end, it also houses the spring arm structure with connection to the springs which are themselves connected to the support structure. The gimbal is designed such that its moment of inertia is lower than the rotor inertia (*i.e.* $J_g^x \ll J_r^x$) such that by-product angular momentum in x- axis is reduced as outlined in the equation (2.45). Gimbal is also manufactured from aluminum.

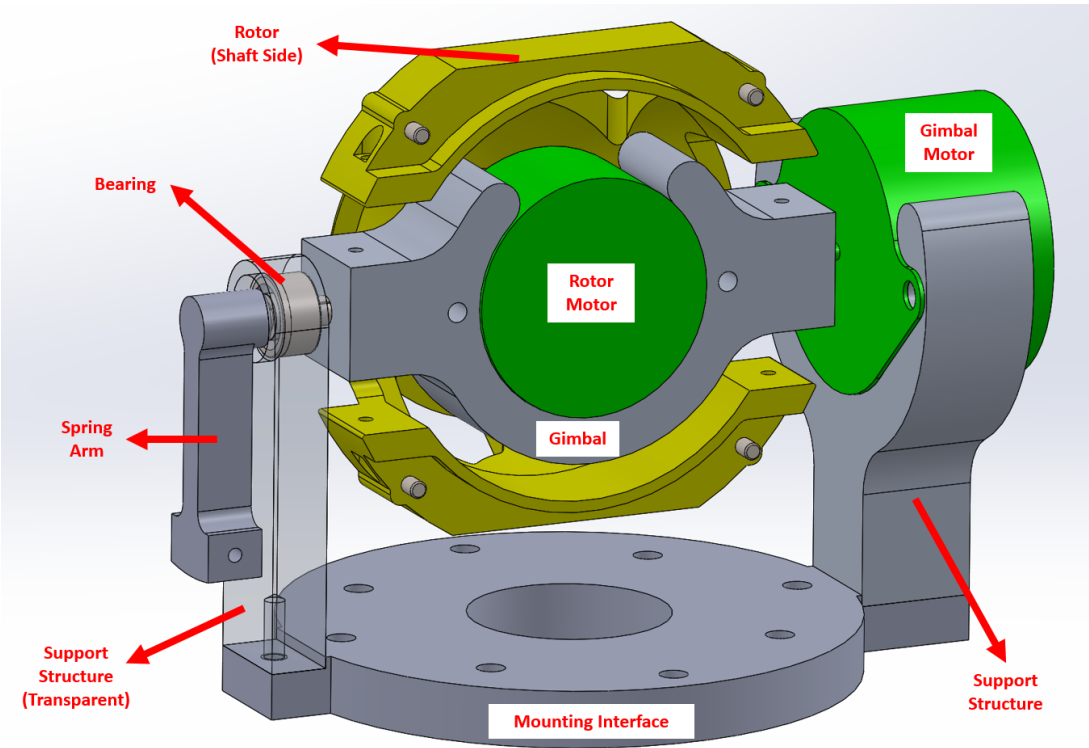


Figure 3.5. The Gimbal and Its Mechanical Interfaces

On one end, the gimbal is connected to the support structure via bearing whereas its other end is connected to the gimbal motor via a shaft. Gimbal was designed to be axisymmetric in its rotation axis. On the tip of the gimbal structure (at the spring arm), a fixture was later added to enable the mounting of IMU.

3.2.2. Springs

There are several purposes for the existence of the spring elements in the actuator. The ultimate aim of the project is to remove the need for the bearing equipment, but as it was mentioned earlier, for the time being, they are included in the current prototype. This is not a deviation from the initial aim, the main purpose of the current prototype is to explore the possibility of the vibration-based actuation hence it is not the intended final product.

Thus, the spring elements were introduced to represent the flexible mechanical connection between the gimbal and the support structure as well as the rotor and gimbal; hence adequately representing the VBA architecture. Another purpose of spring implementation was to tune the fundamental frequencies of the gimbal and rotor to be coincident or close. The VBA is able to function only if the gimbal and rotor are vibrating at identical or sufficiently close frequencies.

Another use of springs was to constraint the rotary motion of stepper motors to their single step mechanically. Recall that the stepper motors were utilized in a nontraditional way; oscillating within a single step. Initial operations without springs exhibited that stepper motors may tend to switch to the next step inadvertently even though sinusoidal waveforms were being applied at selected coils. This was not a desired event for the current application. Hence, springs restrict the rotor and gimbal motion within $\pm 7.5^\circ$.

Another challenge in the implementation of the springs was the realization of torsional springs. Torsional springs were impossible to be utilized due to the practical implementation problems. Instead as evident from Figure 3.6, the implementation of the rotary springs had to be carried out by linear spring with moment arms. This was a non-ideal case and their influence can be observed in the results in the upcoming chapters. Especially, the gimbal axis springs have a substantial effect on the z- axis output of the actuator.

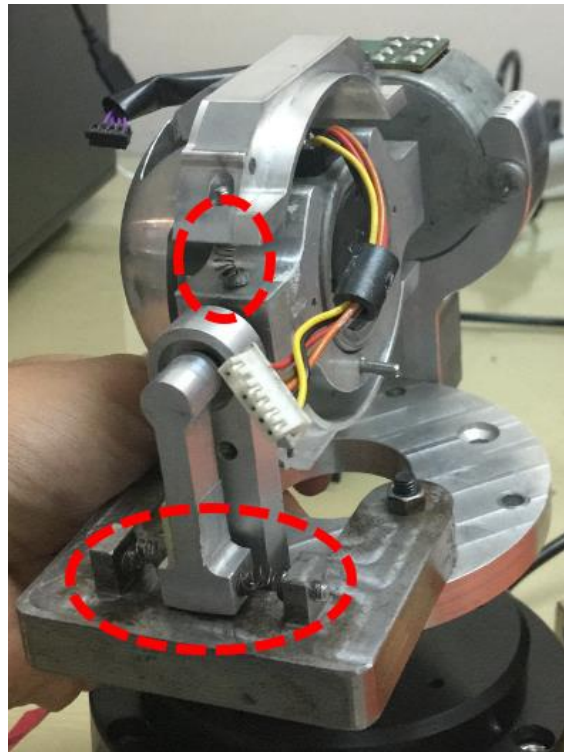


Figure 3.6. Spring Elements at Gimbal and Rotor

The natural frequencies of 14 Hz and 16 Hz were observed in the gimbal and rotor responses, respectively. The device has to be driven at resonance frequency to maximize the kinetic energy of the actuator. To rationalize this approach, consider the equation of motion of a single mass and spring system:

$$m\ddot{x}(t) + kx(t) = g(t) \quad (3.1)$$

Assuming that the forcing function $g(t)$ is described to be sinusoidal,

$$g(t) = F\sin(\omega t + \sigma) \quad (3.2)$$

Where F is the amplitude of the forcing function, ω is the excitation frequency in radians and σ is the phase. Assuming the response $x(t)$ to be in the form:

$$\begin{aligned} x(t) &= X\sin(\omega_r t + \sigma_r) \\ \dot{x}(t) &= -\omega_r^2 X\sin(\omega_r t + \sigma_r) \end{aligned} \quad (3.3)$$

Plugging expressions in Eq. (3.3) back into Eq. (3.1) and rearranging:

$$X(k - \omega_r^2 m) \sin(\omega_r t + \sigma_r) = F \sin(\omega t + \sigma) \quad (3.4)$$

Thus, the parameters of the response function Eq. (3.3) is obtained as,

$$\begin{aligned} \omega_r &= \omega \\ \sigma_r &= \sigma \\ X &= \frac{1}{m} \frac{F}{\left(\frac{k}{m} - \omega^2\right)} \end{aligned} \quad (3.5)$$

Consequently, the linear momentum of the hypothesized system can be described as:

$$p(t) = m\dot{x}(t) = F \frac{\omega}{\left(\frac{k}{m} - \omega^2\right)} \cos(\omega t + \sigma) \quad (3.6)$$

The kinetic energy of the system can also be described as:

$$KE(t) = \frac{1}{2} m\dot{x}^2(t) = \frac{F^2}{m} \frac{\omega^2}{\left(\frac{k}{m} - \omega^2\right)} \cos^2(\omega t + \sigma) \quad (3.7)$$

Note that both linear momentum and kinetic energy can be increased by increasing the forcing function amplitude F or the excitation frequency ω . But, as it can be observed, the theoretical maximum (which is ∞) can be reached when the excitation frequency is sufficiently close or identical to the natural frequency of the system, $\omega_n = \sqrt{k/m}$. Thus, the system should be excited at or near the natural frequency of the system to maximize the kinetic energy available for a set value of F . To excite both the gimbal and rotor sufficiently close to their natural frequencies, an excitation frequency of 15 Hz was picked for the current prototype's operation.

3.2.3. Support Structures & Cabling

Other mechanical components can be summarized as the balancing mass, motor housing support structures, and the mounting interface. These elements are already annotated in Figure 3.2 and Figure 3.5. Balance mass is utilized to minimize the prototype COG offset caused by the large gimbal stepper motor and to bring back the COG closer to the air bearing rotation (*i.e.* z-) axis. It also acts as a mounting point for the gimbal linear springs. Support structures enable the housing of gimbal motor and

carry the gimbal itself. In the course of experimentation campaign, it was envisioned that the prototype will require to be mounted to different experimental devices such as air bearing or load cell. Mounting interface provides the necessary mechanical connection interface for rigid mounting of the actuator to the aforementioned devices.

Last but not least, one other important (yet under-appreciated) element of the actuator is the cabling distributed throughout the actuator. As mentioned earlier; since only limited angle of rotation would be carried out, no slip-ring elements were implemented. Instead, flexible wiring was utilized for power and signal transmission between the mount, gimbal, and rotor. For their flexible effect to be minimal, very thin copper wire of AWG 32 size was utilized. Their implementation can be observed from Figure 3.7.

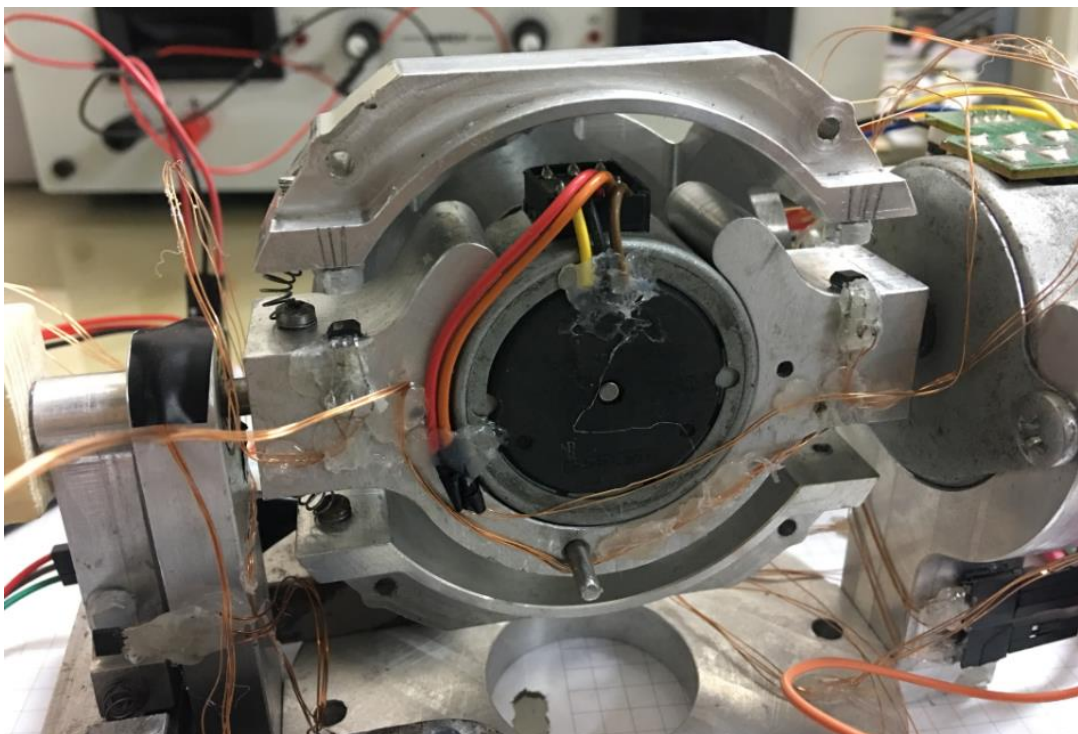


Figure 3.7. Inner View of the Actuator Displaying Extensive Cabling within the Gimbal Stage. Also Note the Rotor Stage Springs Visible due to The Removed Sensor Side Hemisphere

3.2.4. Structural Analysis

Structural modes of the design were investigated to make sure that the structural modes of the VBA mechanical components were sufficiently away from the planned system excitation (*i.e.* 15 Hz) so that they would not disturb the expected output. For this, finite element models of such components were built and simulated via MSC ADAMS. The first four lowest modes of the overall device and the corresponding structural components are shown in Figure 3.8 and Figure 3.9. The lowest fundamental mode is observed in the gimbal shaft element which is 3014 Hz. Remembering that the excitation is planned to be in the vicinity of 10-20 Hz, it was concluded that natural frequencies of the system are sufficiently (*i.e.* two orders of magnitude) away from the operating frequency of the actuator. In other words, the structure is much stiff in comparison with the gimbal and flexible modes.

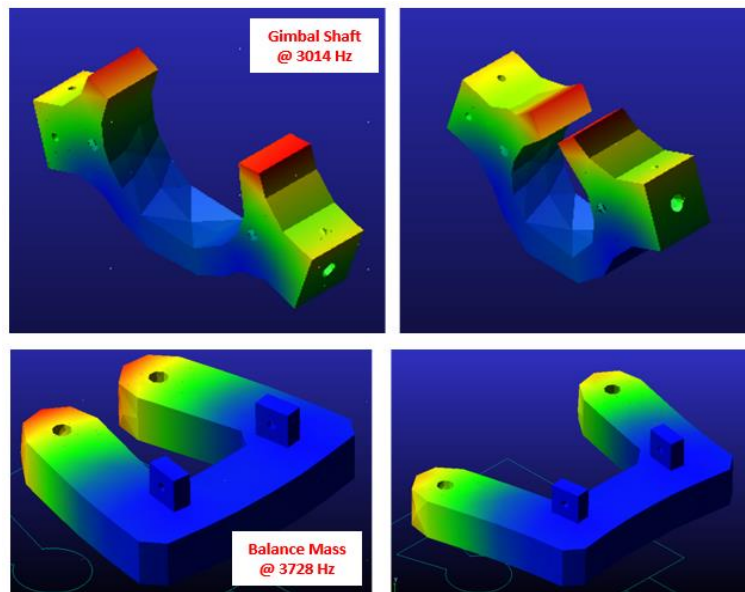


Figure 3.8. Fundamental Modes of the Gimbal Shaft and the Balance Mass

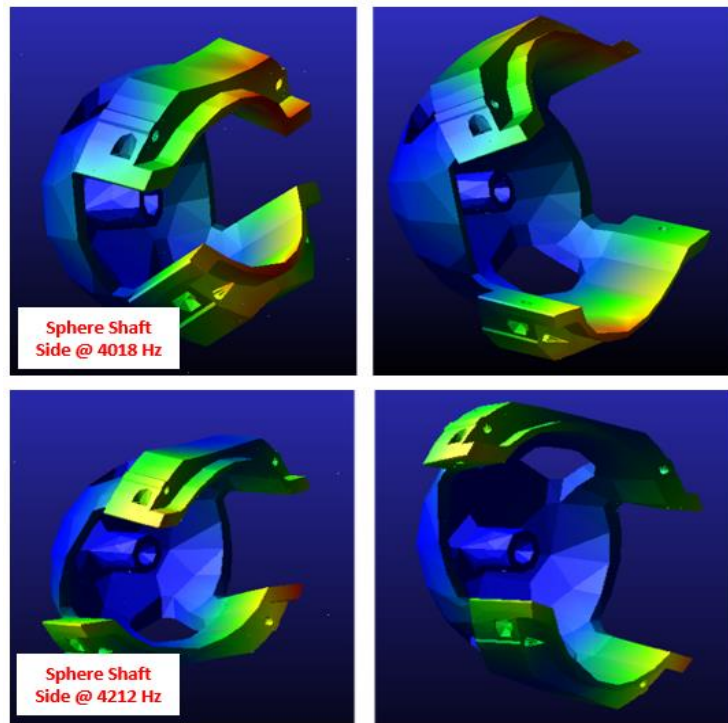


Figure 3.9. Fundamental Modes of the Shaft Side Rotor Hemisphere

3.3. Electrical Architecture

3.3.1. Power Interface

Power buses required to operate the actuator have the following potential differences: 3.3V, 5V and +/- 7.4 V. MEMS gyroscopes in the actuators are powered by the 3.3V bus whereas the Hall effect sensors are utilizing the 5V bus. The buffer amplifier circuitry requires the much larger +/- 7.4 V for amplifying purposes.

3.3.2. Stepper Motors

Two separate stepper motors are utilized for gimbal and rotor actuation, which are not used in the traditional stepping sense in which consecutive coil groups are energized to generate stepping rotary motion. Rather, one or at most two coil groups are energized with a sinusoidal voltage signal in order to create oscillating rotary motion.

The rotor stepper motor is of unipolar architecture and has five input leads. As mentioned earlier, the rotor stepper is located in gimbal and fixed to the gimbal with screws and bolts. The wiring needed to power it is transferred over the support structure through the gimbal structure and since only small angles of travel are concerned no slip ring implementations were carried out. In contrast, the gimbal motor is of bipolar type with four input leads connections. Rotor motor has a maximum torque capability of 80 mNm whereas the gimbal motor has 125 mNm capacity.

3.3.3. Driving Circuit

The driving voltage signals for the rotor and the motor are generated by electronic components with low operating current values. On the other hand, at the actuator end of the circuit, we have high current demanding elements such as the stepper motors. This demand by the stepper motor cannot be met by the waveform generating electronic components. Thus, a “buffer amplifier”, or in other words “voltage follower circuit”, was implemented; first to protect the relatively delicate electronics and secondly, to provide necessary operating current to the stepper motors from the high current (maximum 2.8A) capable batteries. This type of circuitry was realized through an operational amplifier circuit utilizing ON semiconductor’s LA6500 power opamp. Capacitors were also included in the design for noise rejection.

Additionally, during the load cell experimentation, it was observed that if the opposing coil groups in the gimbal motor were excited with an inverted signal waveform; there were substantially fewer disturbance torques. A similar effect was not observed in the rotor motor. The difference probably caused by the different architectures of the motors. Hence, an additional inverting circuit was also implemented which inverts the signal already being applied to the first coil. All in all, this resulted in the driving circuit architecture presented in Figure 3.10, together with its physical realization in Figure 3.11.

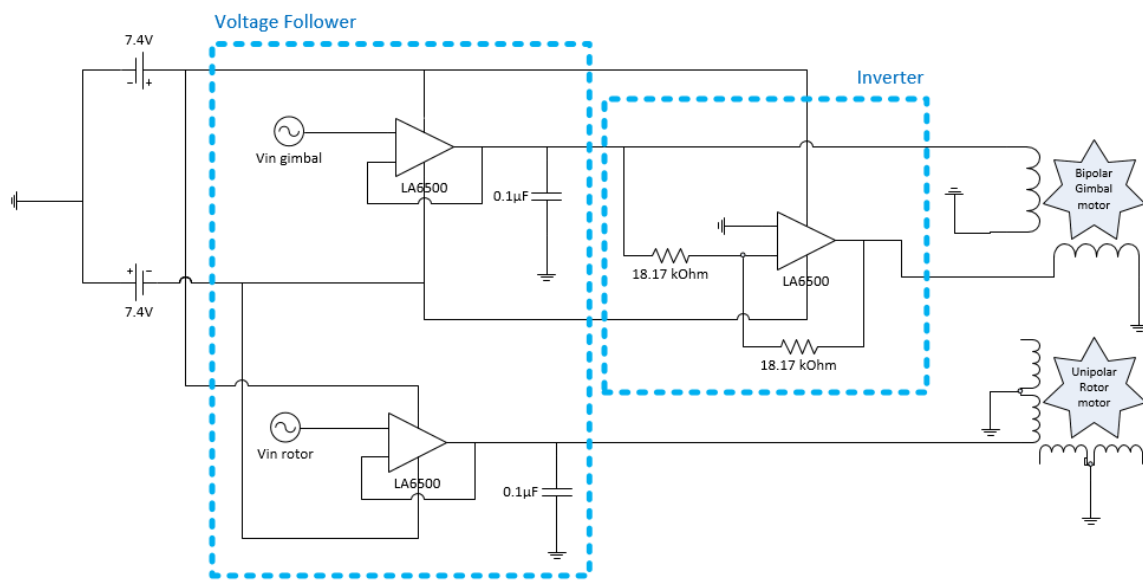


Figure 3.10. Electrical Diagram of the Driver Circuit

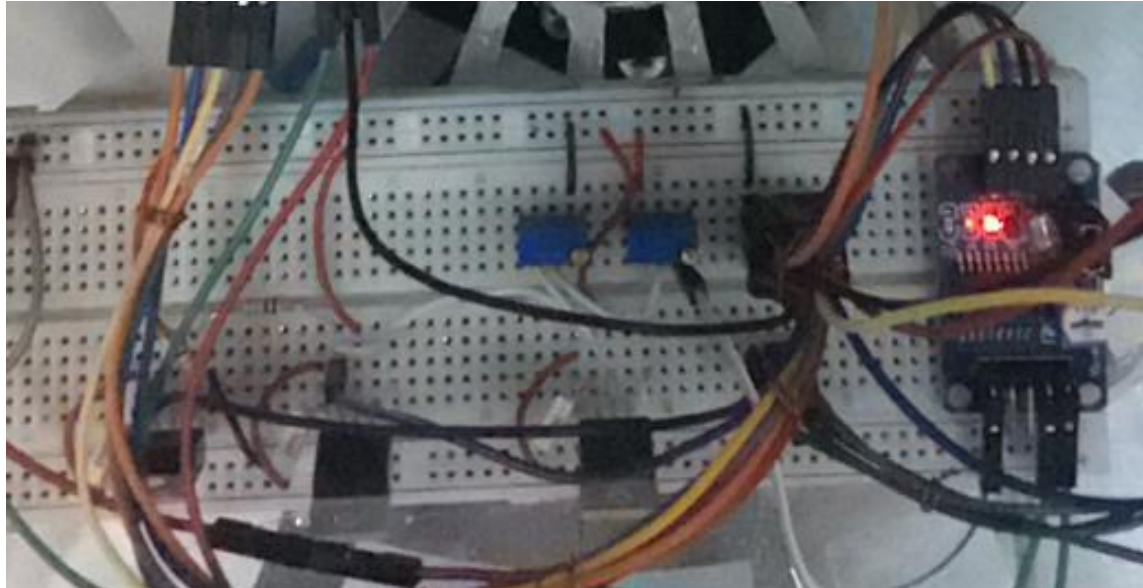


Figure 3.11. Circuit Implementation

3.3.4. Instrumentation

The instrumentation in the actuator consists of gyroscopes and hall effect sensors for each stage. For gimbal, a single IMU for angular rate detection and two hall effect sensors for the angle detection was utilized. A similar set of elements are also used in the rotor for angle and angular rate detection. As mentioned in section 3.2.1, a special mount was designed for IMU placement for the rotor and an additional part was integrated to the gimbal for ease of IMU integration. For IMUs, a COTS MEMS IMU MPU6050 from Invensense was utilized. This IMU included both 3-axis accelerometer and 3-axis angular rate sensors. It is commanded via I2C bus and operates with 3.3 Volts. During the actuator operations, its angular rate sensing function was utilized whereas its accelerometer function was utilized during gyroscope and hall effect sensor calibration.

Utilized IMUs that are very common to consumer electronics such as cellular phones and are substantially low cost. However, they did not arrive together with calibration information. Hence, a separate calibration campaign for each IMU had to be carried out to identify their measurement parameters, before being integrated into the actuator. These parameters were the scale factor and sensing element orientation. The calibration campaign was conducted as outlined in Ref. [82] where the IMU was put in consecutive stable poses numbering around 20. Instances from such calibration campaigns are exhibited in Figure 3.12.

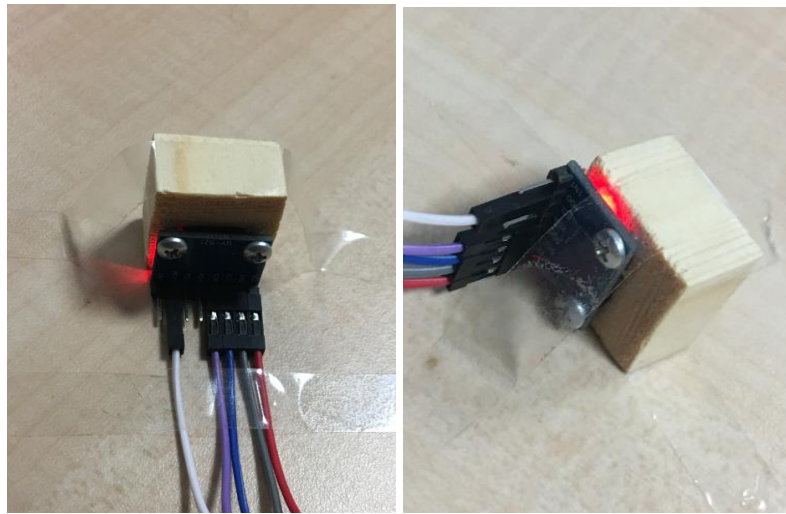


Figure 3.12. Gimbal IMU in Different Stable Poses for Calibration Data Acquisition

Having the Earth's gravity as an absolute reference vector and knowing Earth's gravitational acceleration magnitude, the calibration parameters for the accelerometer were obtained which are shown in Table 3.1.

Table 3.1. Calibration Parameters for the Accelerometers

Parameter	Symbol	Unit	Gimbal	Rotor
Offset Angles	ε_{yz}	direction cosine	-0.00048	-0.00119
	ε_{zy}	direction cosine	-0.00388	-0.00287
	ε_{zx}	direction cosine	-0.00190	-0.00376
Scaling Factors	s_x^a	NA	0.99358	0.99761
	s_y^a	NA	1.00201	0.99734
	s_z^a	NA	0.98811	0.98882
Bias	b_x^a	g	-0.04046	0.03938
	b_y^a	g	0.01609	0.01365
	b_z^a	g	0.09282	0.05159

The algorithm for obtaining IMU calibration parameters can be described as follows; while using Earth's gravity vector as a reference, the IMU is put through consecutive

different poses with smooth (*i.e.* slow) transition between them. The instances when IMU is static is detected using a classifier depending on the variance in acceleration measurements. For the static periods, the measurement model Eq. (3.8) was utilized. A least-squares optimization method was then utilized for identifying the parameters in the model that fits it best to the accelerometer measurements in the static intervals.

These parameters were then utilized to populate the measurement model for the accelerometer;

$$\bar{a}^r = \begin{bmatrix} 1 & -\varepsilon_{yz} & \varepsilon_{zy} \\ 0 & 1 & -\varepsilon_{zx} \\ 0 & 0 & 1 \end{bmatrix} \begin{bmatrix} s_x^a & 0 & 0 \\ 0 & s_y^a & 0 \\ 0 & 0 & s_z^a \end{bmatrix} \left(\bar{a}^m + \begin{bmatrix} b_x^a \\ b_y^a \\ b_z^a \end{bmatrix} + \bar{v}^a \right) \quad (3.8)$$

where \bar{a}^r is the real acceleration values, ε terms correspond to the rotational angles transforming the accelerometer measurement axes to orthogonal axes, s terms correspond to scaling values, \bar{a}^m is the accelerometer measurement, b terms are the bias values, and \bar{v}^a is the accelerometer measurement noise.

Similarly, the calibration parameters for the gyroscope were also obtained as presented in Table 3.2. Note that, since the bias values for the gyroscopes change at each turn on-off cycle; these values are collected at the initialization time of each new run.

Table 3.2. Calibration Parameters for the Gyroscopes

Parameter	Symbol	Unit	Gimbal	Rotor
Offset Angles	γ_{yz}	direction cosine	0.00787	0.01213
	γ_{zy}	direction cosine	0.00054	0.02692
	γ_{zx}	direction cosine	-0.00610	0.00996
	γ_{xz}	direction cosine	-0.00098	0.02834
	γ_{xy}	direction cosine	0.01409	0.13236
	γ_{yx}	direction cosine	-0.01230	0.02497
Scaling Factors	s_x^{gyr}	NA	1.04255	0.97341
	s_y^{gyr}	NA	1.01511	1.11397
	s_z^{gyr}	NA	1.02379	1.08229

These parameters were then utilized in the gyroscope measurement model:

$$\bar{\omega}^r = \begin{bmatrix} 1 & -\gamma_{yz} & \gamma_{zy} \\ \gamma_{xz} & 1 & -\gamma_{zx} \\ -\gamma_{xy} & \gamma_{yx} & 1 \end{bmatrix} \begin{bmatrix} s_x^{gyr} & 0 & 0 \\ 0 & s_y^{gyr} & 0 \\ 0 & 0 & s_z^{gyr} \end{bmatrix} \left(\bar{\omega}^m + \begin{bmatrix} b_x^{gyr} \\ b_y^{gyr} \\ b_z^{gyr} \end{bmatrix} + \bar{v}^{gyr} \right) \quad (3.9)$$

where $\bar{\omega}^r$ is the real acceleration values, γ terms correspond to the rotational angles transforming the gyroscope measurement axes to orthogonal axes, $\bar{\omega}^m$ is the accelerometer measurement and \bar{v}^{gyr} is the gyroscope measurement noise.

Thus, for several consecutive poses the IMU's orientation with respect to the local gravitational vector was obtained. Later, having obtained this information and the recorded angular rates between each consecutive pose the sensor parameters for the gyroscope functionality were also obtained, completing IMU calibration.

For angular sensing combination of hall effect sensor and permanent magnet were utilized. The Hall sensor of question is Allegro's UGN3503. It is an analog sensor that gives out different voltages levels in relation to the intensity of a magnetic field (or in other words, proximity of a magnetic element). For angle sensing of each stage with Hall sensors, two of such sensors in symmetric configuration were utilized. Gimbal and rotor implementations can be observed from Figure 3.13.

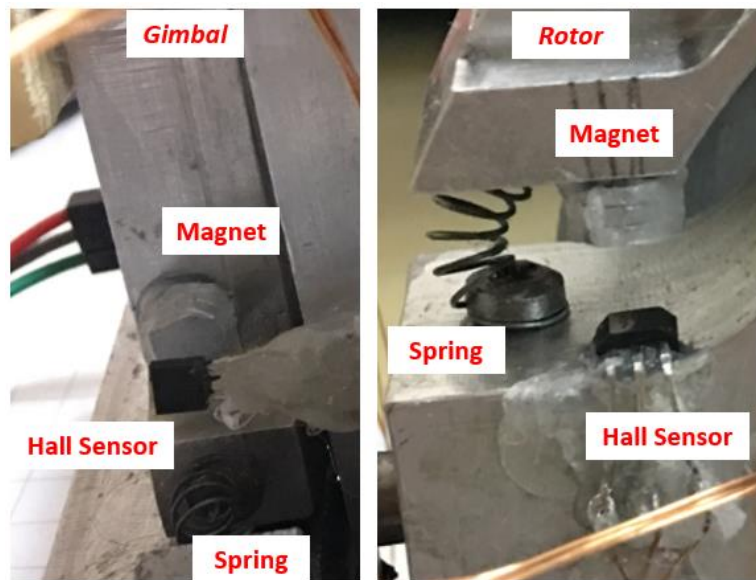


Figure 3.13. Gimbal and Rotor Hall Effect Sensor Implementation Together with Magnet

Note the symmetric placement of the Hall sensors and magnets to mitigate nonlinearity and hysteresis. The calibration campaign with two such sensors for each stage was carried out utilizing with the angle data derived from IMU measurements to obtain a look-up table (or a polynomial fit), that can relate the Hall sensor voltage reading to a specific angle. Such curve fits are exhibited in Figure 3.14 for the gimbal and Figure 3.15 for the rotor. In these figures, x- axis is the voltage measurement by the ADC in bits (refer to PCF8591 information on Appendix B for its voltage resolution). The ADCS is operated in differential mode for combining two Hall sensor measurements. More information on Hall sensor signal acquisition will be presented in section 5.2.2.

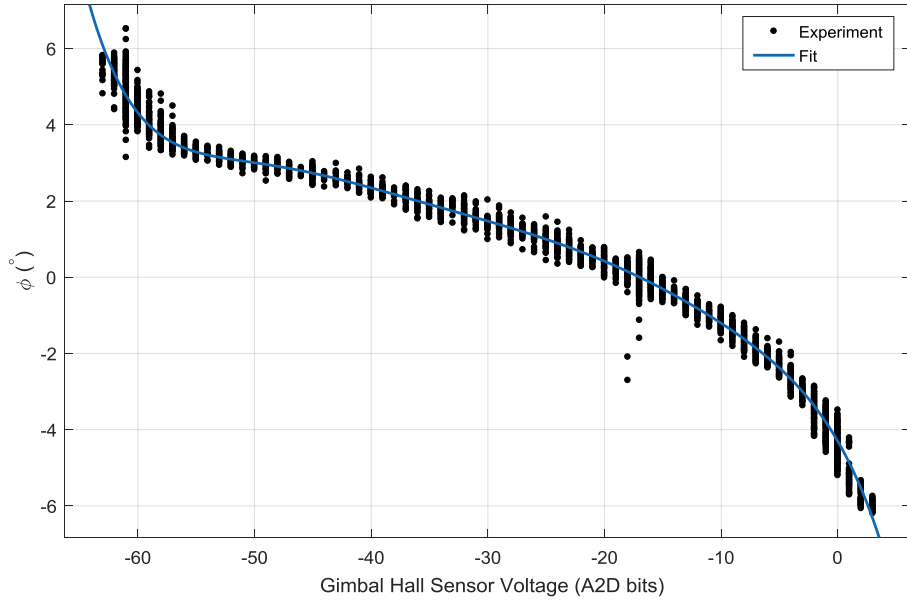


Figure 3.14. Curve Fit for the Gimbal Angle.

The 7th degree polynomial fitted for the gimbal angle calculation in degrees is:

$$\varphi(\tilde{x}) = -0.292\tilde{x}^7 - 0.353\tilde{x}^6 + 0.561\tilde{x}^5 + 0.344\tilde{x}^4 - 0.828\tilde{x}^3 - 0.911\tilde{x}^2 - 2.15\tilde{x} + 0.992 \quad (3.10)$$

where the intermediate function $\tilde{x}(gbits)$ is defined as (since the curve fitting was realized after centering and scaling of the data):

$$\tilde{x} = \frac{1}{20.82} (gbits + 24.96) \quad (3.11)$$

Here, $gbits$ is the differentially measured potential difference from the gimbal axis hall sensors by PCF8591 ADC in bits.

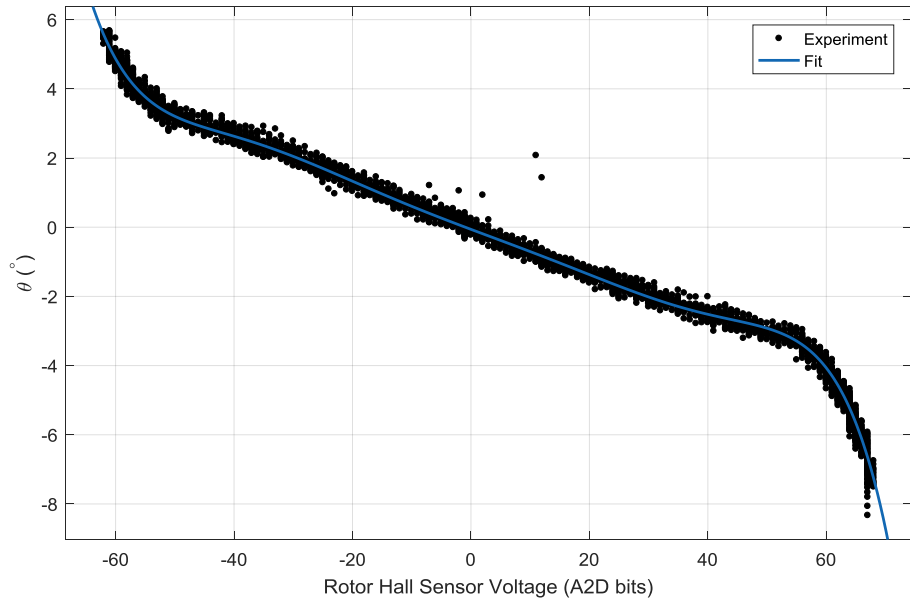


Figure 3.15. Curve Fit for the Rotor Angle.

Similarly, the polynomial fitted for the rotor angle is:

$$\theta(\tilde{y}) = -0.541\tilde{y}^7 - 0.285\tilde{y}^6 + 1.395\tilde{y}^5 + 0.5304\tilde{y}^4 - 0.812\tilde{y}^3 - 0.04\tilde{y}^2 - 2.66\tilde{y} - 0.322 \quad (3.12)$$

Intermediate function $\tilde{y}(rbits)$ is defined as:

$$\tilde{y} = \frac{1}{41.58}(rbits + 24.96) \quad (3.13)$$

This time, $rbits$ is the differentially measured potential difference from the rotor axis hall sensors by PCF8591 ADC in bits.

3.4. Algorithm and Software

There also exists the algorithm and software aspect of the actuator. Software is composed of initialization and configurations scripts, main loop as well as measurement, and filtering and data recording functionalities.

The configuration script communicates with the equipment involved to configure them for the specific ranges of measurements. The gyroscope is utilized within $\pm 1000^\circ/\text{s}$ range whereas accelerometer is configured to measure in $\pm 2\text{g}$ range. This was done by commanding the configuration register of MPU6050 for the specific setting as outlined in the user manual [83]. Similarly, a 20 second initialization time was employed so the bias values of IMU could be extracted. Since IMU has a turn-on bias differing from each turn-on and turn-off cycle, this wait time had to be implemented before each actuator run. After the wait duration is over, the waveforms for the stepper motors are commanded. To prevent abrupt non-linear motion, these sinusoidal waveforms are commanded after being multiplied with a ramp function, which reaches its maximum value in 10 seconds. Thus, the sinusoidal waveforms attain their largest amplitude after 10th second of operation. Meanwhile, the sensing function is utilized to collect angular rate and angle values from the gimbal and the rotor.

The actuator is commanded in an open loop fashion; thus, the measurements form the sensors are only used for data gathering. After a preset duration elapses, the commanding ceases and the data in the memory are recorded to files. The whole implementation is carried out in Python programming language. The existing packages of Python are utilized in the implementation. These packages are “NumPy”, required for utilization of numerical packages and “SMBus”, enabling I2C bus communication.

CHAPTER 4

SIMULATION AND RESULTS

4.1. Justification

In order to better understand the functioning of the vibration based actuator, a dynamics model was built followed by a simulation campaign. Obtaining the theoretically expected results before proceeding with the experimental phase of the study was considered to be beneficial.

For this, one approach would be the utilization of the dynamic equations listed in equations from (2.9) to (2.31). However, these equations do not account for the internal forces and torques; such as gimbal motor torques or joint reaction forces. The dynamics equations have to be reformulated in a multi-body architecture to account for these internal elements.

Such a VBA model had already been built [34]. However, the aim of the current simulation campaign is to develop a model which can mimic the expected results of the actuator described in Chapter 3 as well as its actual experimental implementation provided in Chapter 6.

For the multibody dynamics simulation, MSC ADAMS software was utilized. As it can be recalled from Chapter 3, the resulting system is complex; for instance, torsional springs functionality had to be implemented by utilizing linear springs together with moment arms.

Incorporating such complex solutions from the ground up to the multi-body dynamical model would have been cumbersome. Additionally, whenever such a novel model is introduced, the need for model's verification would also arise. Development of a dynamical model of such a novel actuator is important; yet the main scope of the

current research is not developing high fidelity multi-body dynamics simulation models, but rather proving the concept of vibration-based actuation through experimentation. Additionally, being an industry standard program, any dynamic model developed in MSC ADAMS would automatically be considered to be verified.

Lastly, the CAD design presented previously in Chapter 3 can be imported to MSC ADAMS simulations. Utilizing the same CAD model utilized for manufacturing would yield a model that can represent the prototype with high fidelity in the simulation environment.

All in all, utilization of MSC ADAMS enabled building a reliable and accurate representation of the VBA directly from the design presented in Chapter 3.

4.2. Simulation Model

The simulation model is formed in the MSC ADAMS environment. For this, several elements representing the actuator have to be incorporated into the simulation model. These are the CAD models resulting from the design, flexible elements, definition of joints and degrees of freedom and lastly, the external forces and torques that will be acting on the device. Later, the solver is also configured to run the simulation.

As mentioned earlier, the CAD model was imported from the same design files that were also utilized for manufacturing. These files not only included the shape and dimension data, but also the material information. Hence, MSC ADAMS was able to automatically calculate the mass properties (such as inertia) of various components of the actuator; and subsequently, incorporate them to the simulation.

Mass properties of the experimental tray were taken into account by including its inertia values in the base part which would represent the experimental tray in the simulation. Its inertia values were obtained from the CAD model of the experimental tray (for details, refer to section 6.2.2.1). To better represent the air bearing experimental setup, the inertia of the air bearing itself ($0.75E-3$ kg-m 2) was also

incorporated into the simulation in addition to the experimental setup tray ($20.64E-3$ $\text{kg}\cdot\text{m}^2$).

Later, the degrees of freedom of the actuator were defined in the simulation model through the built-in joint definitions. MSC ADAMS has built-in idealized joint primitives; of which revolute joints assumes no translation and enables single axis only rotation. Thus, gimbal and rotor joints were represented as revolute joints. Moreover, the base of the actuator was left to be free to rotate in space.

Recall that springs were utilized in the prototype to constraint the oscillatory rotational motion to a single step of the stepper motors (section 3.2.2). These springs are also modeled via the flexible element functionality of ADAMS. Their stiffness values were obtained by experimenting with the spring elements and determining their per unit length of stiffness. Linear spring stiffness at each gimbal spring was assumed to be 423 N/m whereas each rotor spring's stiffness was 623 N/m.

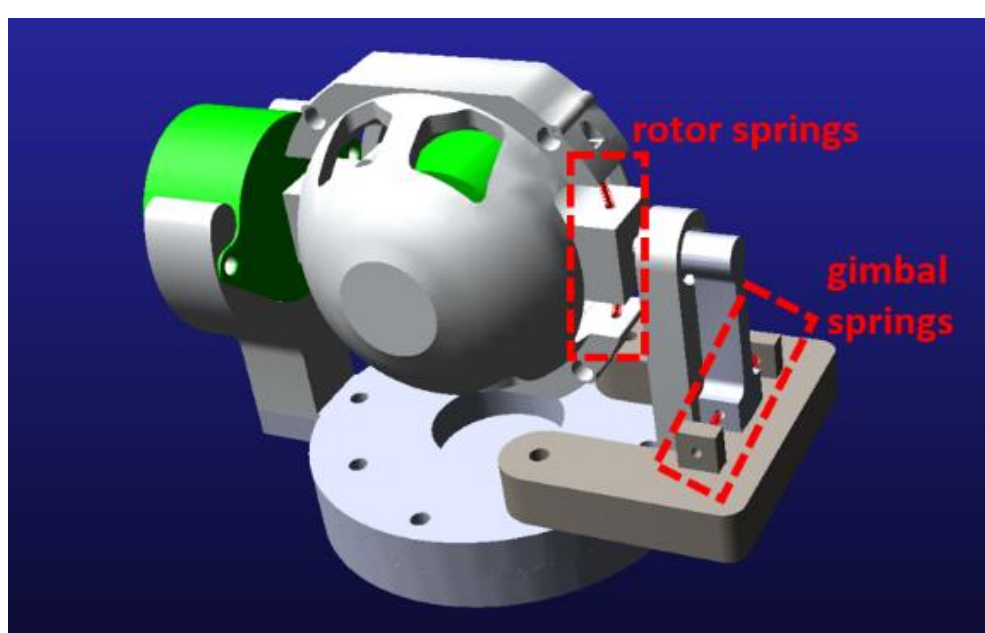


Figure 4.1. The Model Utilized in ADAMS Simulation. Note the Highlighted Flexible Elements Representing Gimbal and Rotor Springs

The following sinusoidal inputs (in N-m) are applied to the gimbal and rotor motors. at 15 Hz frequency with 90° phase difference.

$$\begin{aligned}\tau_{gim,x}^{mot}(t) &= 0.04 \sin(2\pi 15t) \\ \tau_{rot,y}^{mot}(t) &= 0.03 \sin\left(2\pi 15t + \frac{\pi}{2}\right)\end{aligned}\quad (4.1)$$

These inputs are multiplied with a haversine function to facilitate smooth initialization of gimbal and rotor oscillations. Similar to the case of actual actuator this ramp-like function reaches its maximum value of 1 in the 10th second of the operation.

The simulation was run for 320 seconds with 1ms time step. Built-in WSTIFF solver was utilized to solve the dynamic system.

4.3. Results

The resulting motion is presented in Figure 4.2. Note that the vibration based actuator is successful in imparting net angular motion to the tray even though gimbal and rotor undergo purely oscillatory motion. A detail of the air bearing angle around 150th is also presented within the insert. About 20° of rotation was observed for 320 seconds of actuator operation. Angular velocity values were filtered with a low-pass filter at 0.1 Hz to filter out the higher order dynamics and to isolate the secular component of the actuator angular velocity. An average angular velocity of ~0.06°/s was observed.

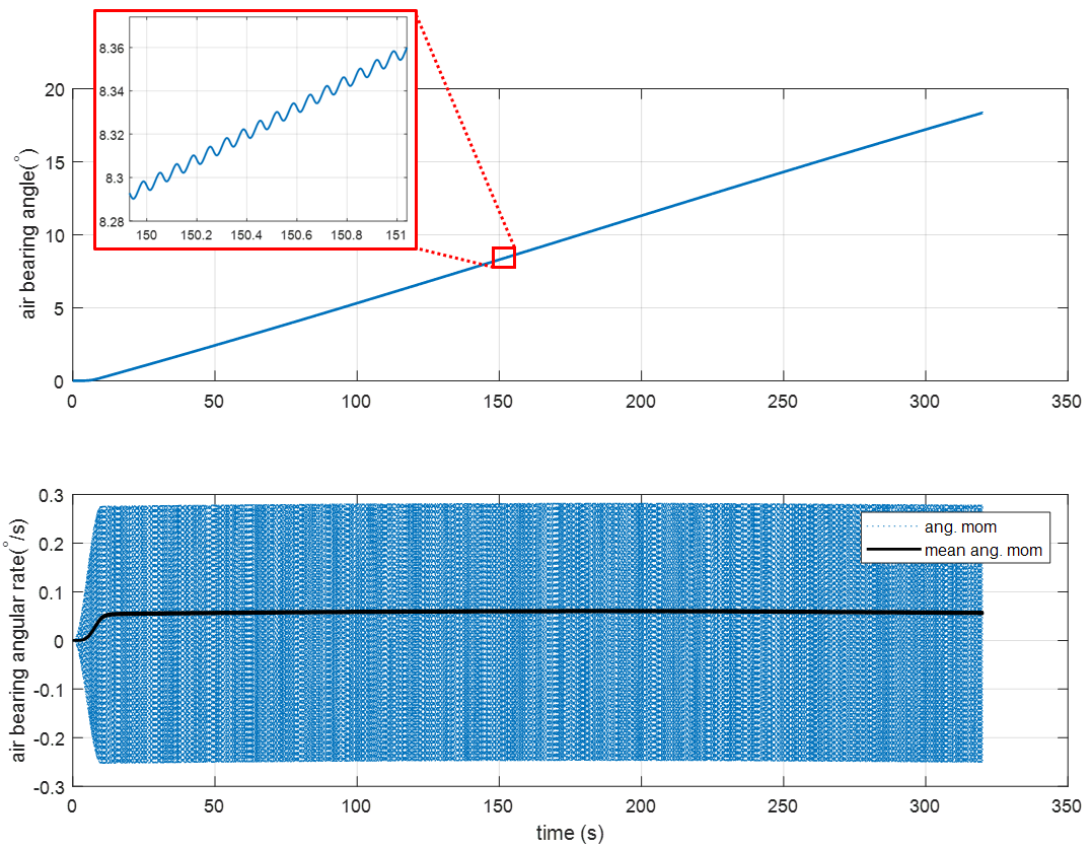


Figure 4.2. MSC ADAMS Simulation Result Predicting the Angular Motion of the Air Bearing Due to Operation of the Actuator.

The frequency spectrum of the angular rate was obtained for the interval spanning from 50th to 300th seconds (*i.e.* during steady-state oscillations). As it can be observed from Figure 4.3, the free-body motion is existing in the spectrum as a DC (*i.e.* 0 Hz) component. Additionally, the frequency content at 15 Hz is apparent; this dynamic is considered to be due to the gimbal spring implementation; whose operation also induces disturbance torques in z- direction with a frequency equaling to that of the excitation. On the other hand, the frequency content observed at 30 Hz corresponds to the expected output of the device. As predicted in Eq. (2.45), the operation of the device introduces an angular momentum in the z- direction at twice the frequency of excitation. Another (third) harmonic at 45 Hz also exists, but its three orders

magnitude smaller than the second harmonic; therefore, not having a substantial contribution to the overall output.

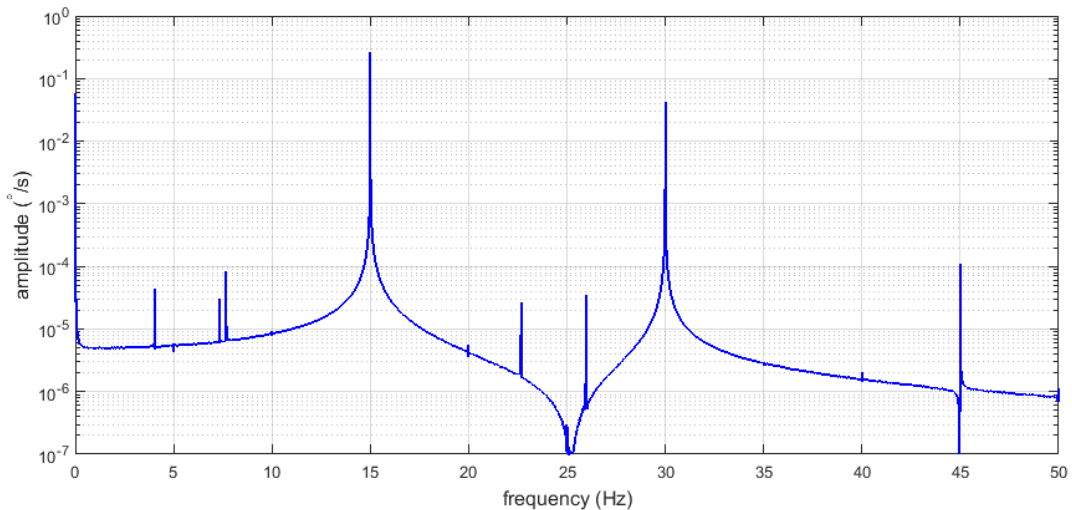


Figure 4.3. Spectrum of Air Bearing Angular Velocity.

As observed from Figure 4.4, the rotor oscillates between -1.54° and $+1.54^\circ$ whereas the gimbal oscillates between -2.45° and $+2.45^\circ$. The phase difference of 90° is evident between the rotor and gimbal, as evident from the following plot.

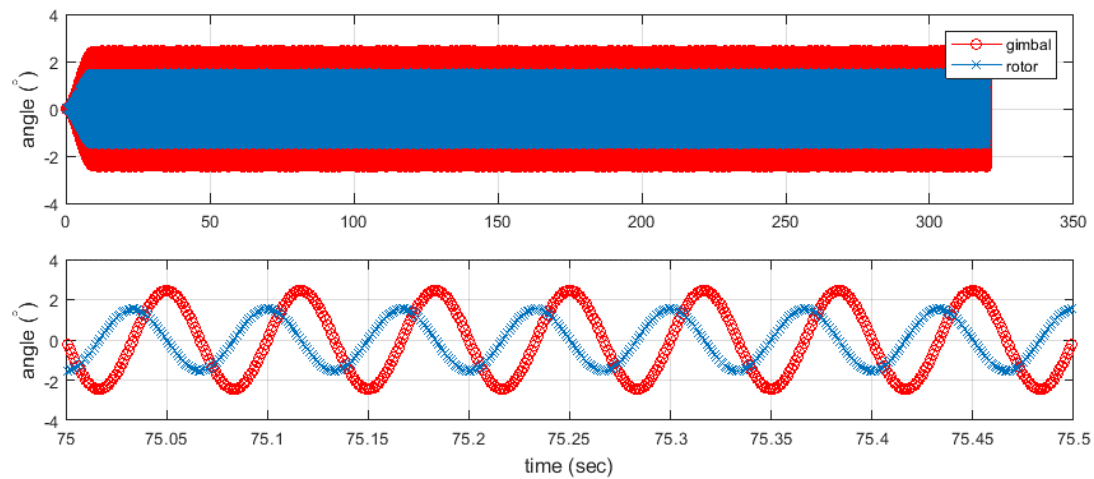


Figure 4.4. Simulated Rotor and Gimbal Angles with Specific Detail at the 75th Second.

The frequency content of the gimbal and rotor is presented in Figure 4.5. Again, it was extracted from the interval spanning the 70th to 320th seconds. Second and third harmonics of the excitation frequency at the 30 and 45 Hz are also present at the rotor, but they are not as evident as the principal excitation at 15 Hz.

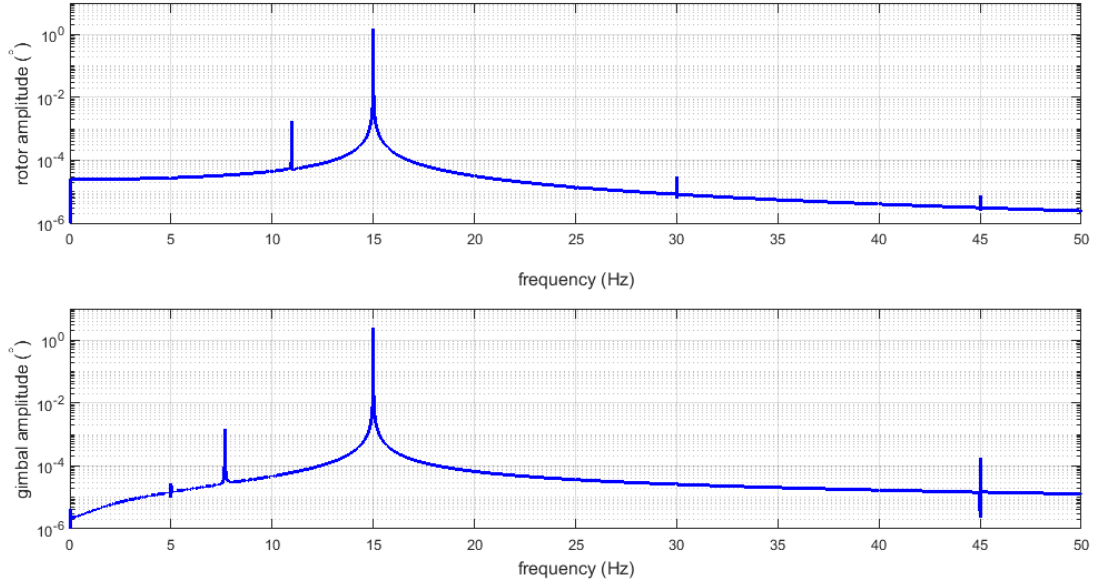


Figure 4.5. Frequency Content of the Rotor (Above) and Gimbal (Below) Angular Motion.

The angular rate for the gimbal and rotor are given in Figure 6.13 for the duration of the simulation. Again, the details from the run are also presented the lower plot. The angular rate for the rotor oscillates within $\pm 144.9 \text{ } ^\circ/\text{s}$ whereas the gimbal oscillates between $\pm 230.9 \text{ } ^\circ/\text{s}$. Similar to the angle measurements, the intended phase difference between rotor and gimbal are also evident.

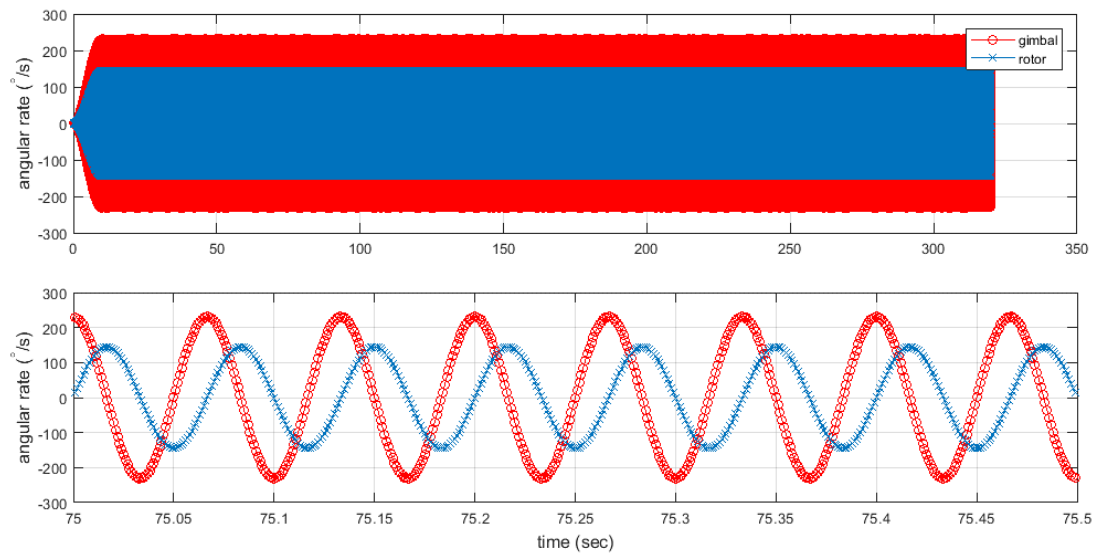


Figure 4.6. Rotor and Gimbal Angular Rates with Specific Detail at the 75th Second.

The angular momentum of the air bearing is obtained by combining the previously obtained angular rate data with the estimate of the setup tray moment of inertia (Figure 4.7).

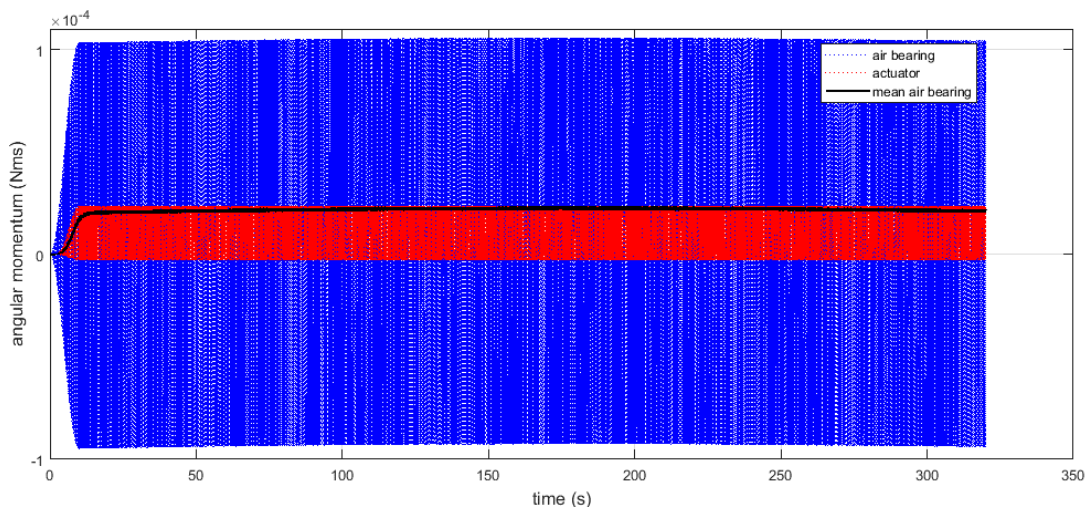


Figure 4.7. Comparison of Result Together with the Actuator Output.

As it can be inferred from above, even though the angular momentum of the air bearing is sinusoidal in nature, it also has a constant component which leads to the rotation. As can be observed from Figure 4.7, angular momentum expression of the vibration based actuator obtained through Eq. (2.63) corresponds to this mean motion experienced by the air bearing. The excessive vibration observed in the air bearing is itself considered to be stemming from the moment arm implementation of the gimbal spring.

CHAPTER 5

EXPERIMENTAL SETUPS

Two different setups have been utilized in the experimentation campaign. One setup focused on measuring the torques resulting from the operation of the device whereas the other one assessed the angular motion actuating capability of the VBA device by utilization of a single axis air bearing.

5.1. Load Cell

The experimental setup with the load cell is presented in Figure 5.1. High-resolution NI PCI-4461 signal generator card is utilized to generate sinusoidal voltage signal input to the stepper motors. The waveform is commanded through NI's propriety software. In the experimentation, only pure sinusoidal waveforms were utilized. The measurements were carried out by AMTI's MC3A-250 transducer with Gen 5 amplifier (datasheet available in Appendix B). The settings of the amplifier were selected such that reaction torques in the range of ± 1.18 N-m in-plane, and ± 1.47 N-m out of plane (i.e. perpendicular to the table) directions are measured, with 0.1% accuracy.

The reaction torques due to the oscillation of gimbal and rotor are measured around the in-plane axes whereas the output is measured in out-of-plane axis.

The load cell itself is resting on an elastic padding providing stable resting on the relatively massive table below (when such a padding was not utilized, the load cell underwent motion during actuator motion, disturbing the measurement process since it has only a few contact points if the surface below is solid and non-elastic).

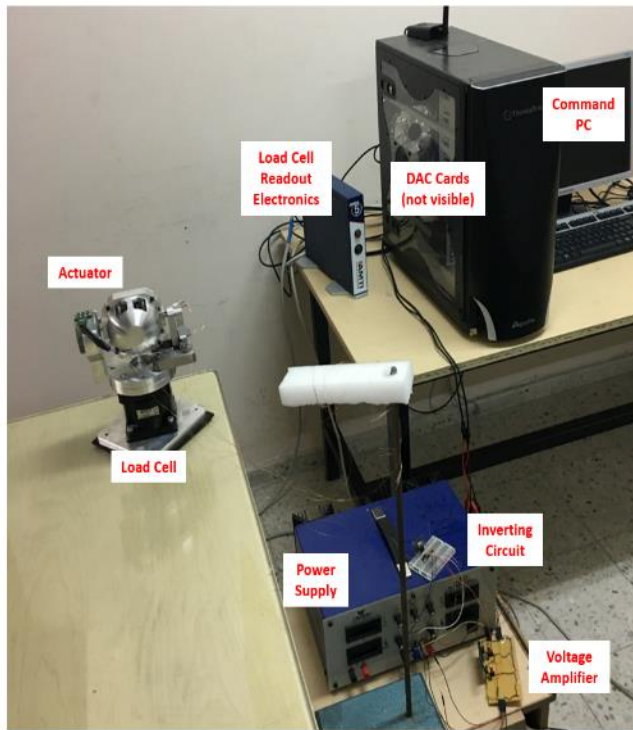


Figure 5.1. Load Cell Experimental Setup

5.2. Frictionless Air Bearing

For frictionless air bearing experiments, two different configurations were utilized.

5.2.1. Tethered Configuration

The tethered configuration setup is shown in Figure 5.2. The command generation and driving circuitry are identical to the load cell setup. The command signals are being carried to the actuator through overhung very thin copper wires (size AWG 32) to minimize their effect on rotary motion. In addition to these, a MATLAB script is also run to collect data from the air bearing encoder. The air bearing utilized is a PI Glide RT-100 rotary air bearing model A-603.050H. It has a built-in incremental encoder with a resolution of 21 arc-seconds per count. It is being air fed with an oil-less Atlas Copco LFx 0.7 medical air compressor through various air filters. The air bearing itself is mounted on a relatively massive mounting pedestal to act as a low-pass motion

filter against outside disturbances. This pedestal has three legs, the height of which can be independently adjusted via screw mechanisms. This configuration enables level adjustment to prevent gravity gradient torque acting on the experimental setup.

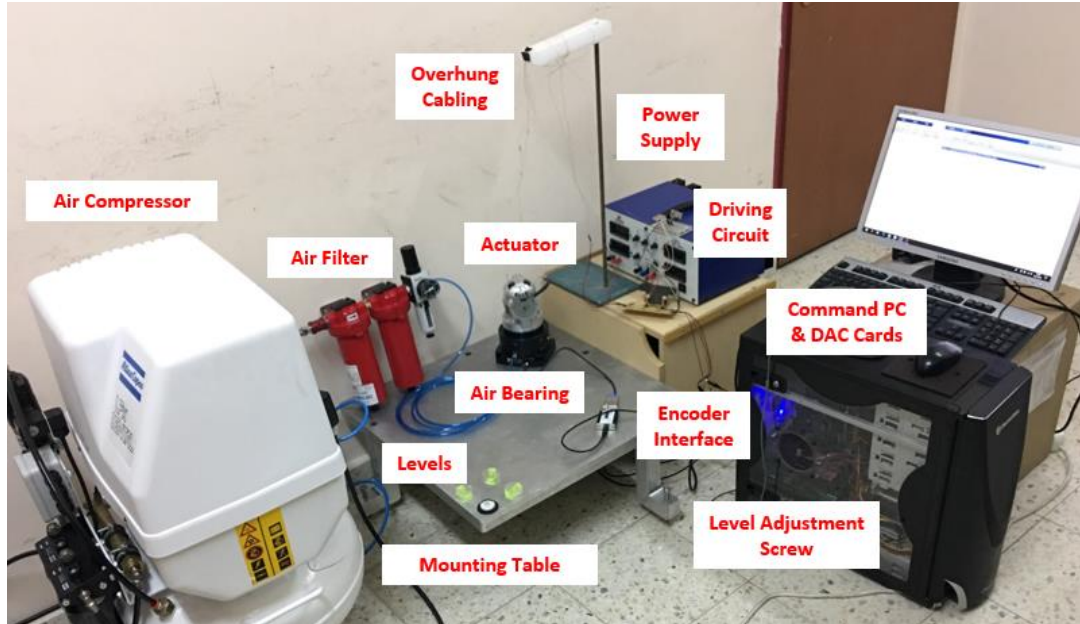


Figure 5.2. Air Bearing Experimental Setup in Tethered Configuration

The water level devices on the mounting pedestal enable level adjustment before operation (Figure 5.3).



Figure 5.3. Levels Present on the Mounting Table for Level Adjustment

5.2.2. Un-Tethered Configuration

The untethered configuration is the main setup utilized used for proving the VBA concept. The architecture for the experimental setup is presented in Figure 5.4.

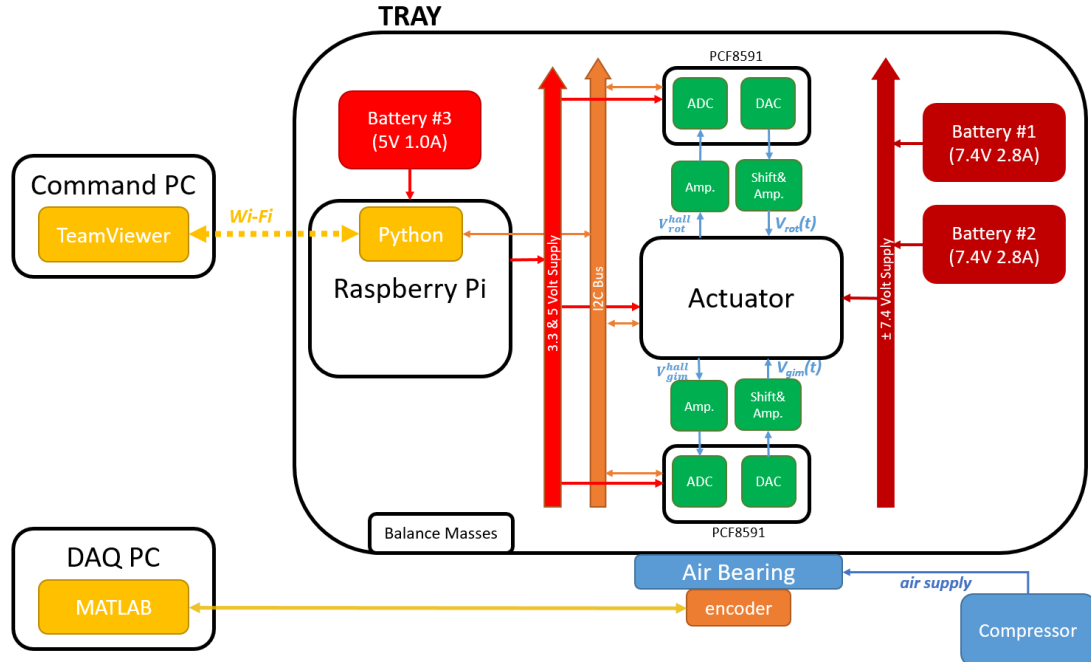


Figure 5.4. Architecture for Untethered Experimental Setup

This configuration is identical to the previous setup, except wireless communication and commanding is now possible to remove the disturbing effects of tethers. Air bearing, air supply, and mounting pedestal are identical to that of the previously introduced tethered setup.

The device is operated in completely wireless fashion to enable a completely independent and frictionless single-axis motion. For this, wi-fi connection with a Raspberry Pi Model B+ single-board computer acting as the main control hub was realized. This computer was accessed from a command PC via a remote connection established over TeamViewer software. The Raspberry Pi also provides 3.3V and 5V voltage supply to the IMUs, ADC/DAC and Hall effect sensors. It is supplied by a

common powerbank capable of providing 5V potential difference with up to 1000mA current supply.

The Raspberry Pi is connected to the PCF8591 ADC/DAC via I2C interface, which supplies sinusoidal waveform to the driving circuitry. Driving circuitry is identical to that defined previously in section 3.3.3, but this time it is commanded via the output DAC output of PCF8591 instead of NI-PCI 4461 signal generator. The PCF8591 output can generate an analog signal in the range of 0V to 4.2V; hence an intermediate command shifting and amplification circuit had to be designed and implemented as presented in Figure 5.5 using a TL082 operational amplifier.

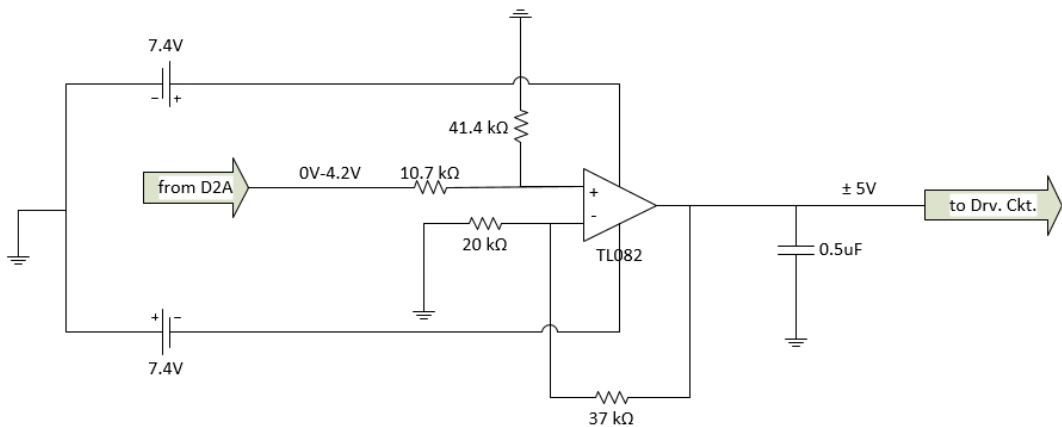


Figure 5.5. Command Shifting and Amplification Circuit

The resulting signals can be observed in Figure 5.6.

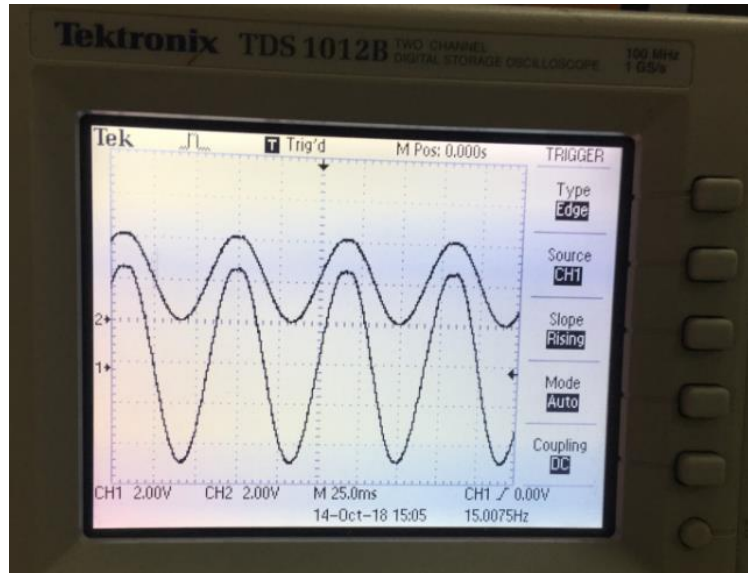


Figure 5.6. Oscilloscope View of the PCF8591 DAC Signal (Channel #2) Shifted and Amplified (Channel #1) to be Fed into Driving Circuit.

ADC functionality of the PCF8591 was also utilized to collect the analog position measurement signals from Hall effect sensors. A Hall effect sensor amplifying circuit was also implemented for this purpose (Figure 5.7). It consists of a voltage dividing circuit followed by an amplifier circuit again employing a TL082 operational amplifier. It amplifies the signal from the Hall effect sensors ranging from 0.8V to 2.3V to a range spanning from 1.4V to 4.4V.

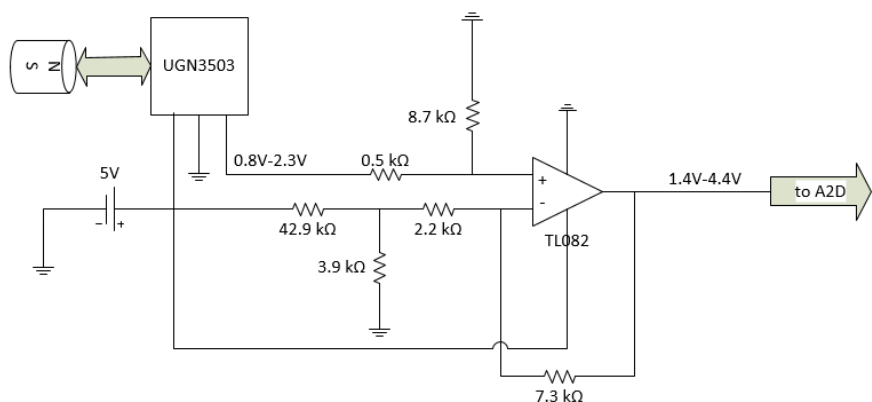


Figure 5.7. Hall Effect Sensor Amplifying Circuit

The required 7.4V potential difference for the operation of the actuator is supplied by two Lithium-ion 2S batteries capable of 2800mA current supply. They are reversely connected to provide both +7.4V and -7.4V supplies. All the above-mentioned equipment is mounted on a tray. This tray would be representing the “spacecraft” carrying the VBA prototype. It is the only element that has a mechanical interface with the air bearing. However, it also needs to be balanced to minimize the disturbing gravity torque in order to efficiently represent single-axis frictionless rotational motion. Hence, lead balance masses were also added to ensure that tray COG was coincident as much as possible with the air bearing rotational axis. The experimental setup elements on the tray are indicated in Figure 5.8.

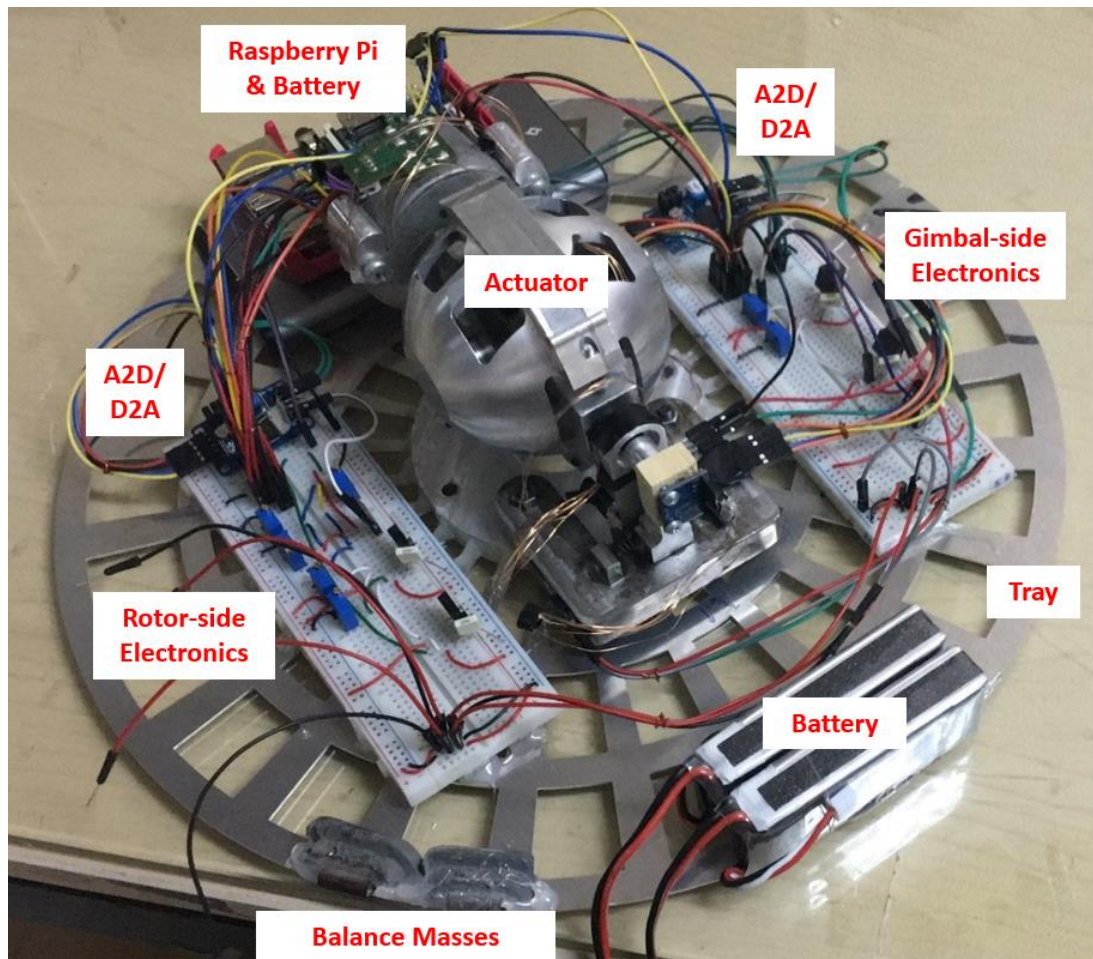


Figure 5.8. Setup for Wireless Experimentation

CHAPTER 6

EXPERIMENTAL RESULTS

6.1. Load Cell

First, a tuning campaign was carried out to determine to optimal input parameters such that gimbal and rotor actuation can produce sinusoidal torque response. The input parameters sought can be defined as:

$$\begin{aligned} v_{gim}^{in}(t) &= V_{gim}^{in} \sin(2\pi ft) \\ v_{rot}^{in}(t) &= V_{rot}^{in} \sin(2\pi ft + \sigma_{in}) \end{aligned} \quad (6.1)$$

Here f is the excitation frequency, σ_{in} is the phase difference among the input potential difference signals. V_{gim}^{in} and V_{rot}^{in} are the corresponding amplitudes of the signals which are being applied to the ports described in Figure 3.1. By carrying out a tuning campaign, it was determined that applying voltage signals with amplitudes 0.6V and 1.2V to gimbal and rotor respectively provided the most sinusoidal-like response in those axes (Figure 6.1). An excitation frequency of 16 Hz was utilized. In such a case, the torques measured by the load cell in the gimbal and rotor axes were obtained for a phase difference of 90° as:

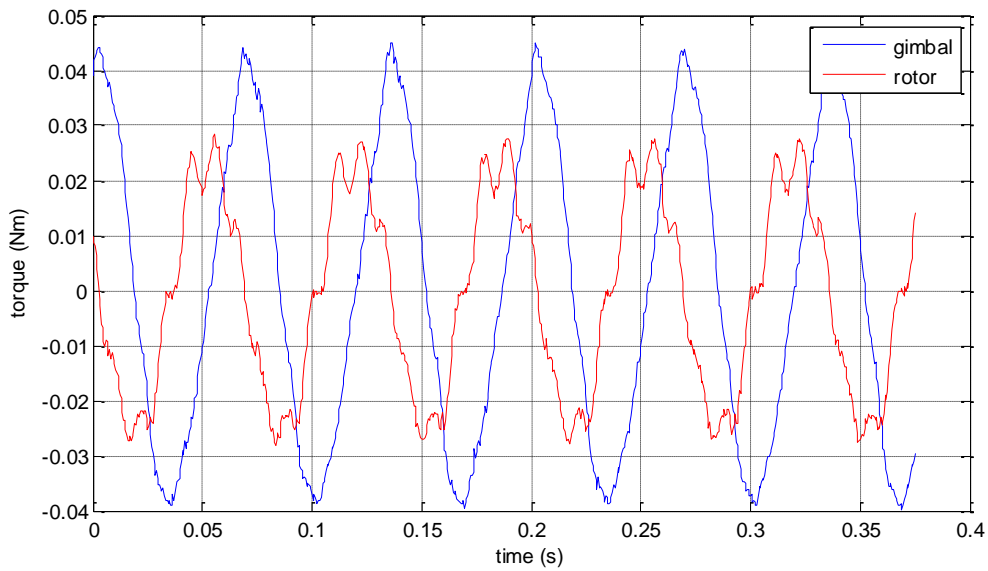


Figure 6.1. Torque Measurements for the Gimbal and Rotor Axis with Sinusoidal Excitations Having 0.6V and 1.2V Amplitudes, Respectively

Similarly, the torque in the output (*i.e.* out-of-plane) axis was measured as:

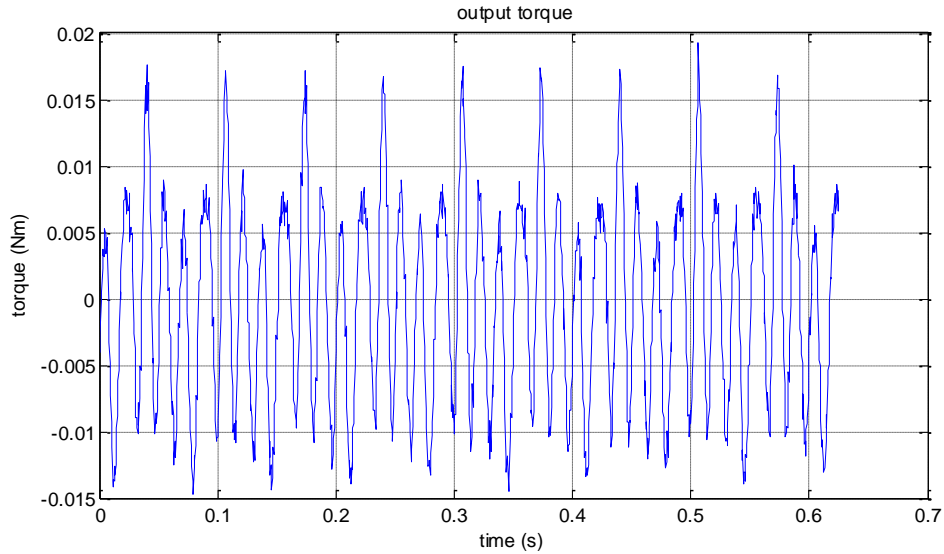


Figure 6.2. Torque Measurements for the Output Axis for the Given Input Parameters

The frequency content of the above measurements is presented in Figure 6.3.

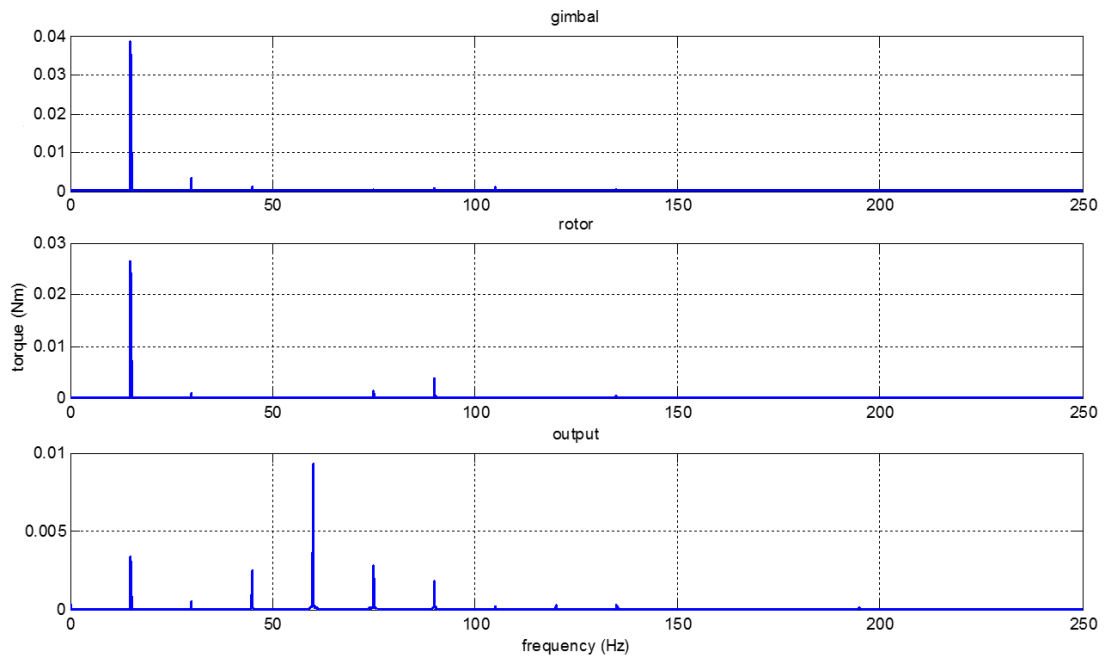


Figure 6.3. Frequency Content of the Torque Measurements. Y- Axis Is in Newton-Meters.

Notice that, even though nearly a pure sinusoidal with almost single frequency content was obtained in the gimbal and rotor axes, the output axis measurement is composed of multiple frequencies, especially emphasized around 64 Hz. However, the mathematical model provided in Ref. [12] was predicting a pure output at the double of the excitation frequency (*i.e.* at 32 Hz). One explanation for this is the existence of additional modes that are being excited due to the existence of padding (and its associated dynamics) between the table and the load cell (recall the padding between the load cell and the table in Figure 5.1).

To better discern whether the content is observed at 32 Hz was indeed the sought output, another experimental campaign was designed. In this case, the variability of the output torque with respect to the input phase difference was utilized, as predicted in Eq. (2.69). In Ref. [12], it was further predicted that the output torque was dependent on the phase difference between input gimbal and rotor torques and reaches its maximum value at 90° and its multiples. Hence, a phase sweep campaign was carried

out to check whether this variation will be observed. First, the variance of the measured gimbal and rotor torque phase difference with respect to the change in the input voltage phase difference, recalling Eq. (6.1), is checked.

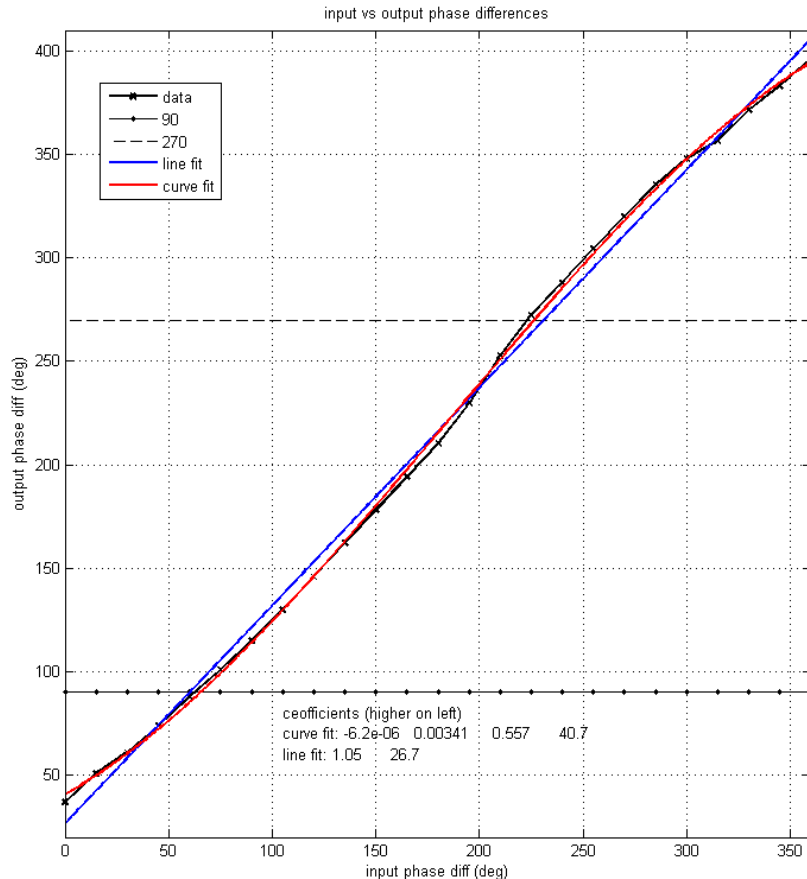


Figure 6.4. Relation Between Input Rotor and Gimbal Voltage Phase Difference with Measured Rotor and Gimbal Torque Phase Difference

As evident from Figure 6.4, phase difference between gimbal and rotor at the voltage input and the torque output exhibit a linear relationship. A first order curve can be fitted to quantify the relationship as:

$$\sigma_{out} = 1.05\sigma_{in} + 26.7^\circ \quad (6.2)$$

After the linearity of this relationship was established, phase sweep campaign was conducted for the output torque.

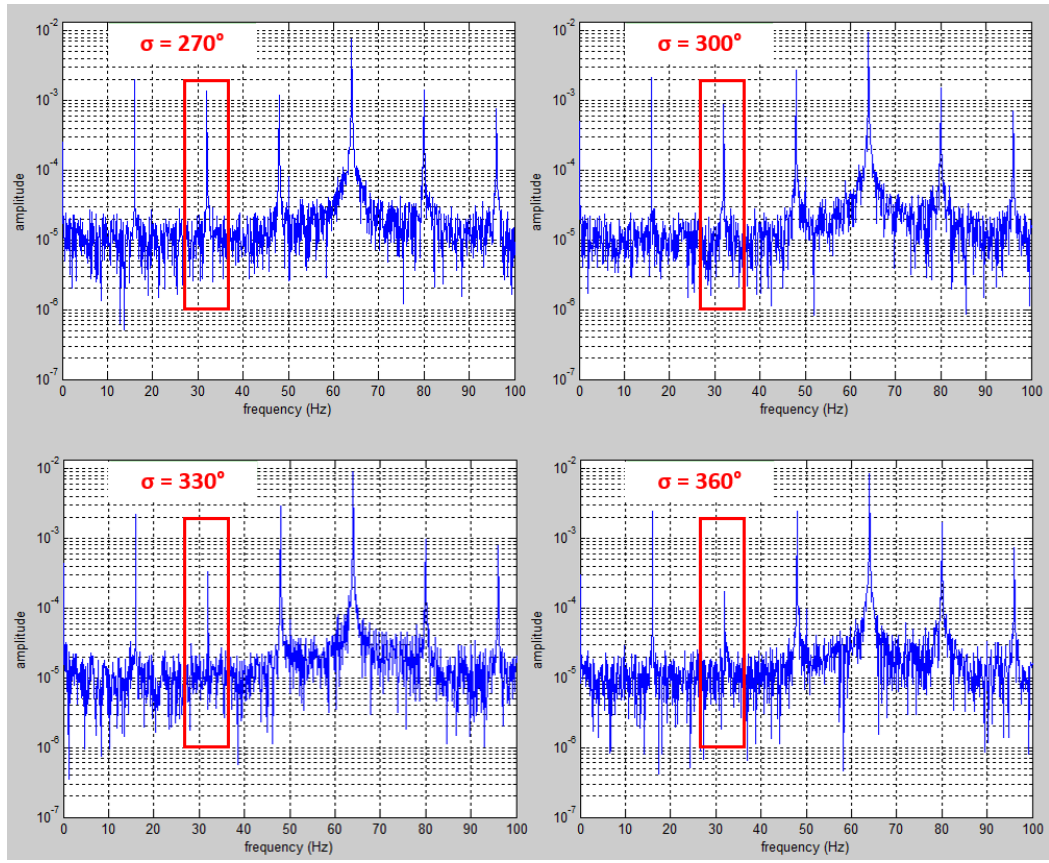


Figure 6.5. Output Torque Frequency Content in Log-Linear Plot for Varying Phase Values

Note that in Figure 6.5, with the varying input voltage phase difference, there exists a visible change in the output torque frequency component at the second harmonic (*i.e.* 32 Hz) of the excitation frequency, as predicted by the previous mathematical model [34] and in Eq. (2.56). Also of note is the relative indifference of the other frequency components in the spectrum to phase sweep. These confirm the fact that observed torque is related to the torque output of the vibration based actuator.

6.2. Frictionless Air Bearing

Due to the fixed nature of load cell experiments, only reaction torques due to device operation was able to be observed. To investigate the mathematical model postulated in Chapter 2 experimentally, a different setup capable of single axis frictionless

rotation was required. Therefore, such a setup was procured and experiments were run first in tethered, and later, in completely free conditions.

6.2.1. Tethered Configuration

The tethered experiment was carried out using single-axis air bearing to get an initial grasp of its functioning as well as its interaction with the actuator. Angular position history of an experimental run is as shown in Figure 6.6. Here, the gimbal and rotor motors are excited at 15 Hz sinusoidal waveforms with 0.6 and 1.6 Volts, respectively (since 15 Hz turned out to be the prototype's fundamental frequency). Utilizing the information presented in Figure 6.4, voltage phase difference of 232° is applied, resulting in a torque phase difference of nearly 270° . Encoder data was sampled at 100 Hz. The air bearing was initially stationary, at 40th second the VBA was initiated. Around 220th second VBA was shut off.

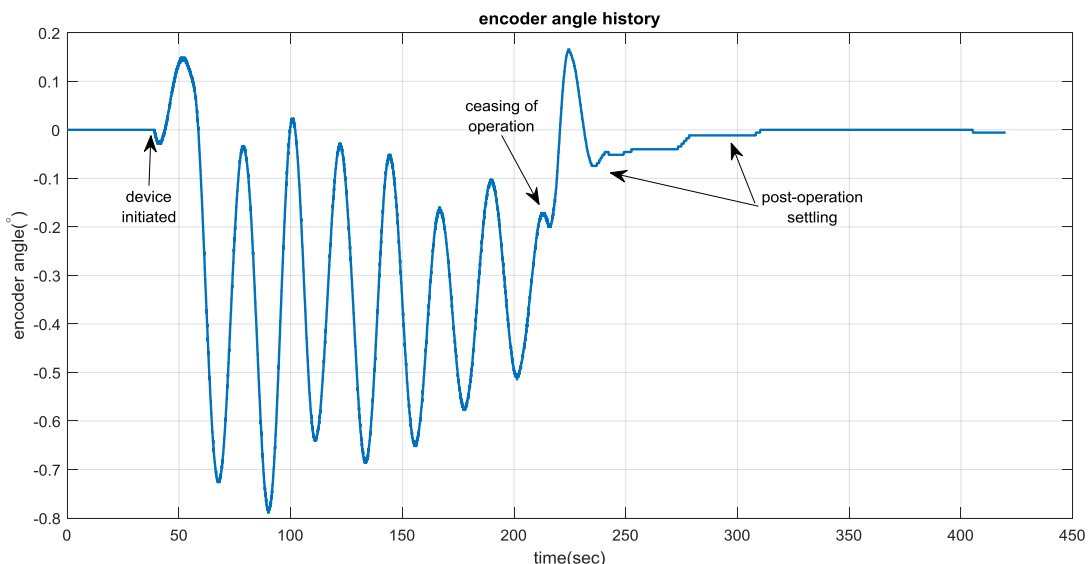


Figure 6.6. Air-Bearing Encoder Angle History

Note that the system oscillates at an offset angle from the starting condition. This is considered to be due to the restoring force from the overhung thin wires carrying the command signals. Hence, an angular history similar to Figure 4.2 is impossible to

obtain because of the captive (*i.e.* tethered) testing condition. Alternatively, the frequency spectrum of the angular motion was investigated. Similar to the MSC ADAMS simulation results (recall Figure 4.3), and as predicted by the Eq. (2.69), the output at the double of the excitation frequency was observed.

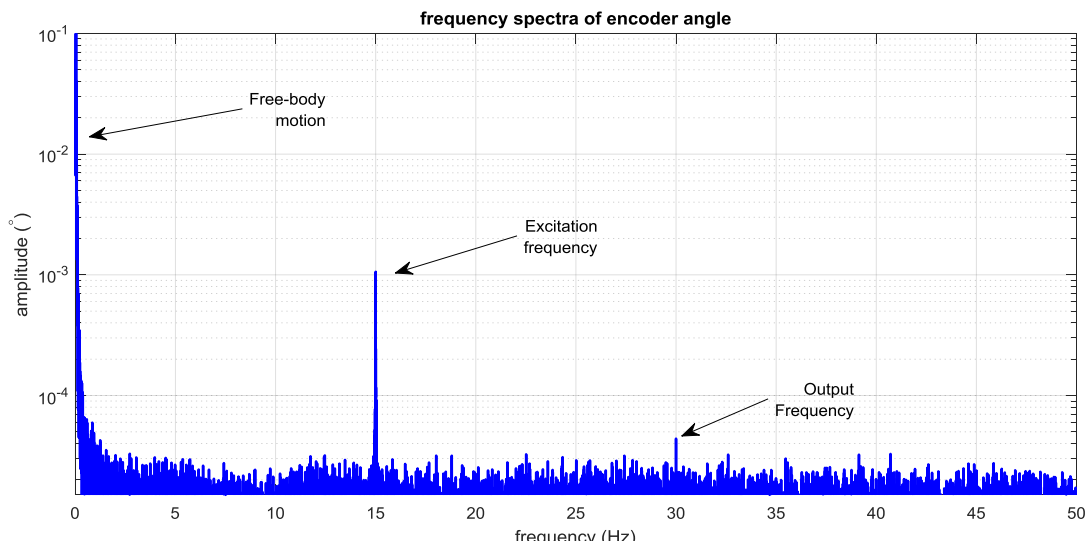


Figure 6.7. Air-Bearing Encoder Angle Spectral Content. Note That Orthogonal Axis Is in Logarithmic Scale Whereas X-axis is in Linear Scale

6.2.2. Un-Tethered Configuration

The results for air bearing experimentation campaign are exhibited in Figure 6.8. The results for four distinct test runs are provided. These runs were carried out for nearly 7 minutes, differing among the test runs slightly. The actuator was initiated at around 40th second and operated for 5 minutes. The actuator managed to rotate the experimental tray mounted on the air bearing in all the runs. About 3° of rotation was observed for nearly five minutes of actuator operation. It is evident that the input phase difference determines the direction of rotation, as predicted earlier by the mathematical model. Different input voltage phase difference settings were utilized; 60° and 232°. This corresponds to output angular motion phase differences of 89.7° and

270.3° , respectively. Also note that the phase differences are 180° apart, leading to motion in the opposite direction as predicted from the z- axis output of Eq. (2.69).

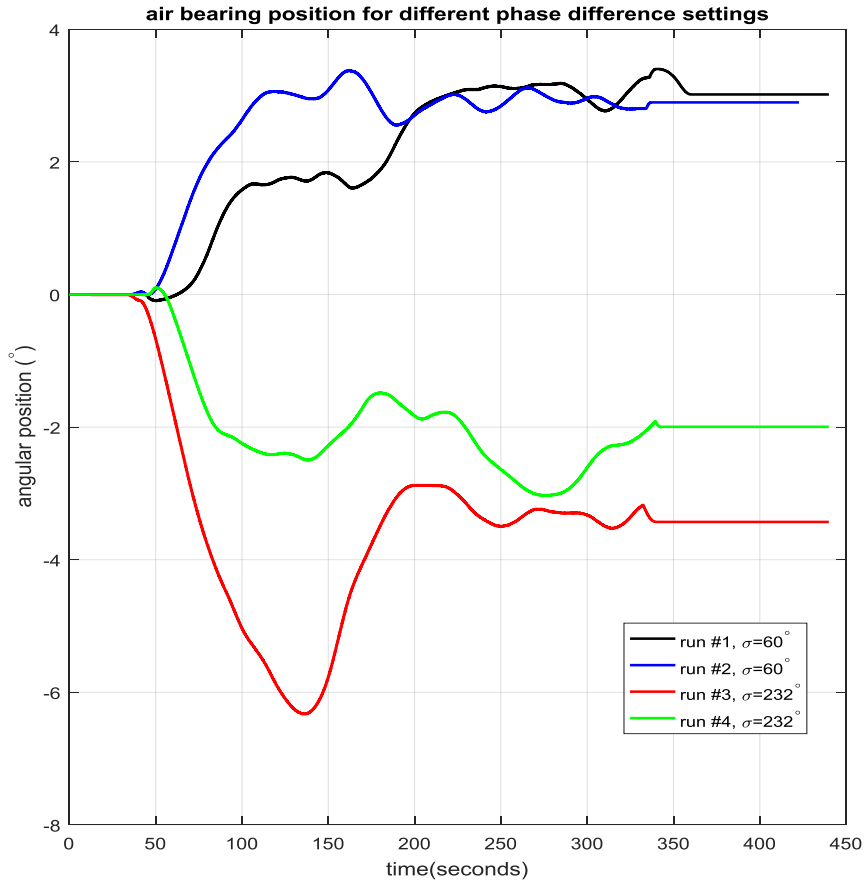


Figure 6.8. Air Bearing Position for Various Input Phase Difference Settings

Also of note, unlike the simulation, the operation of the device did not rotate the experimental setup indefinitely. Disturbances were evident; the rotational motion halts and even reverses at some specific points. This is due to having the center of gravity of the experimental setup higher above the tray; since all the elements of the system are situated on the upside of the tray; resulting in a system more susceptible to the gravity disturbances even though precise leveling had been carried out. Upon coupling with the tilt of the setup table, this leads to a restoring torque around air bearing rotation axis. An equilibrium point would be formed and whenever the system rotates

away from it, a restoring torque would consequently act. Even though extensive work had been done to ensure the system is well balanced, it was observed that the gravity gradient had a substantial effect on the system. Due to the existence of a restoring torque, the actuator can rotate the bearing up to a certain point; where the ability of the actuator is overcome by it.

More detailed telemetry from the test runs #2 and #4 are presented in the forthcoming subsections.

6.2.2.1. Telemetry from run #2

The open loop gimbal and rotor input voltages applied to the driving circuitry in this particular test run can be formulated via the following mathematical expressions,

$$\begin{aligned} V_{gim} &= 2.25 \sin(2\pi 15t) \\ V_{rot} &= 1.95 \sin\left(2\pi 15t + \frac{60}{180}\pi\right) \end{aligned} \quad (6.3)$$

which are in Volts. Note the voltage input phase difference of 60°.

These values were not commanded immediately; rather they were initiated at the 20th second of the experiment. Furthermore, as explained in section 3.4, they were multiplied with a ramp function which reached its maximum value of 1 at the 30th second so that smooth excitation of gimbal and rotor would be carried out.

The resulting encoder data history from run #2 is presented in Figure 6.9. Angular speed derived from encoder angle measurements are also presented. Note that the maximum angular rate imparted by the device on the setup was 0.0548 °/s, which is close to the value obtained via simulation in section 4.3.

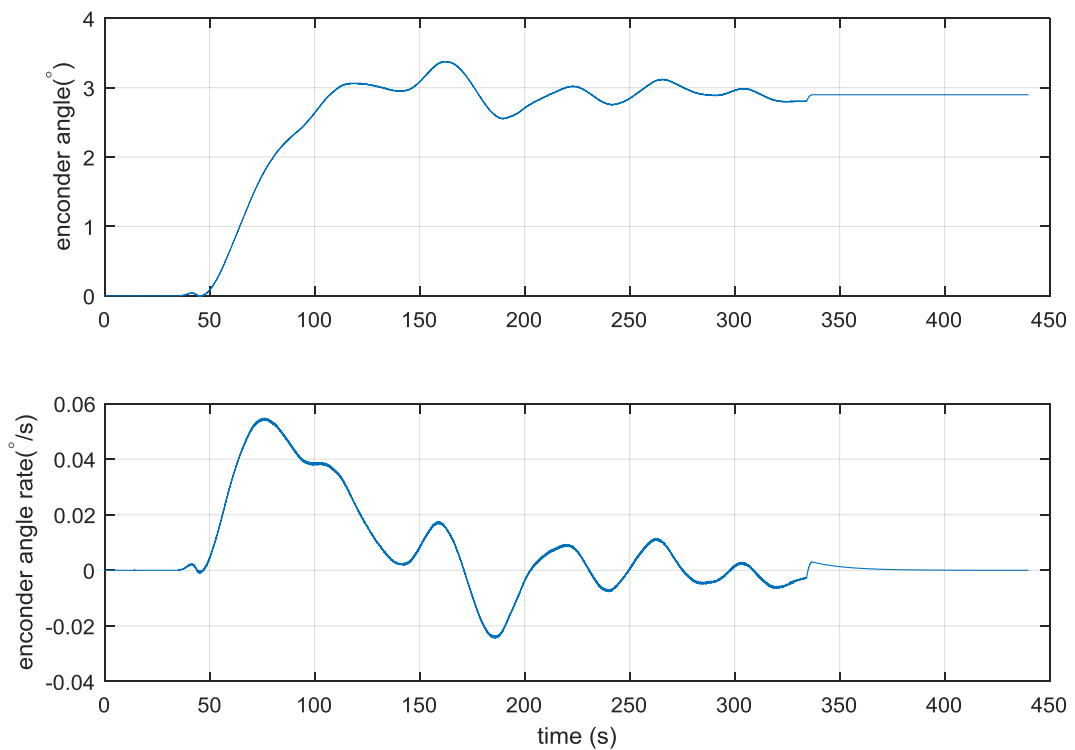


Figure 6.9. Encoder Angle and Angular Rate for Test Run #2

The frequency content derived from the air bearing angular data is shown Figure 6.10. This content is extracted from 70th to 320th seconds (*i.e.* after steady state oscillations were reached). Note the DC content corresponding to the rigid body motion and the specific harmonic at the double (*i.e.* 30 Hz) of the applied input excitation frequency (*i.e.* 15 Hz), as predicted by the mathematical model.

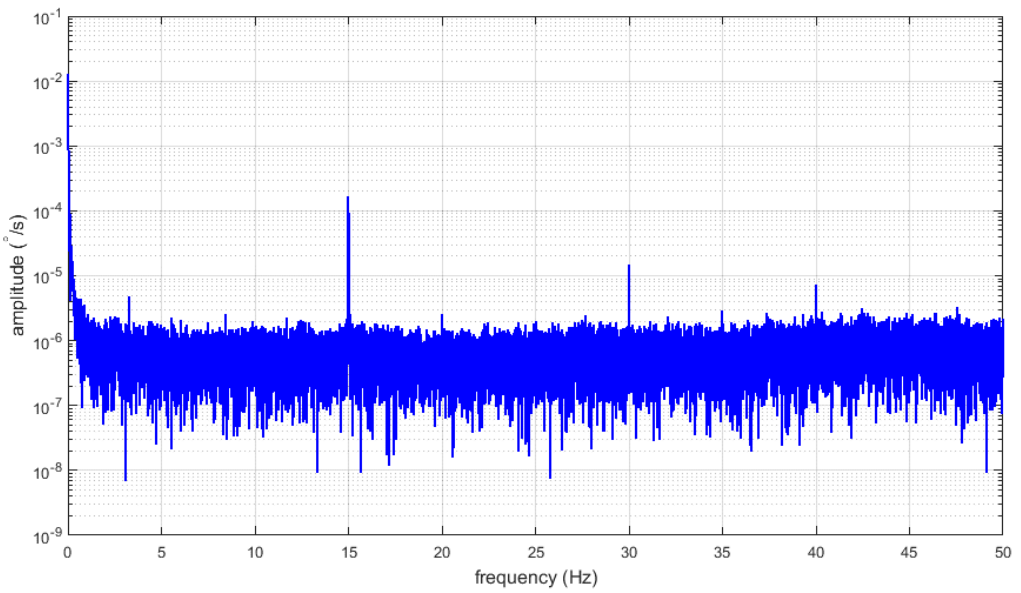


Figure 6.10. Frequency Content of Run #2 Derived from Air Bearing Angle Data

The applied voltages in Eq. (6.3) result in the following rotor and gimbal angles:

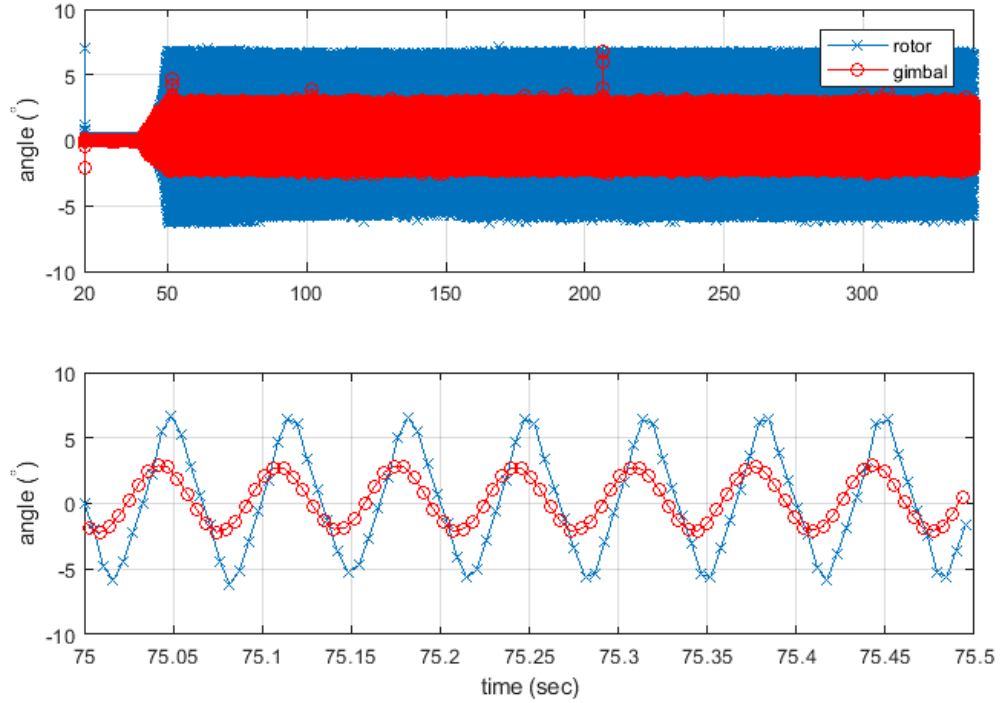


Figure 6.11. Rotor and Gimbal Angles with Specific Detail at the 75th Second

It can be observed from the Figure 6.11 that the rotor angle oscillates between -6.35° and $+7.13^\circ$ whereas the gimbal oscillates between -2.61° and $+2.72^\circ$. Also of note is the phase difference between the rotor and gimbal angles as evident from the lower plot. The frequency content of the gimbal and rotor is provided in Figure 6.12. The frequency content was again, extracted from the interval spanning from 70th to 320th seconds.

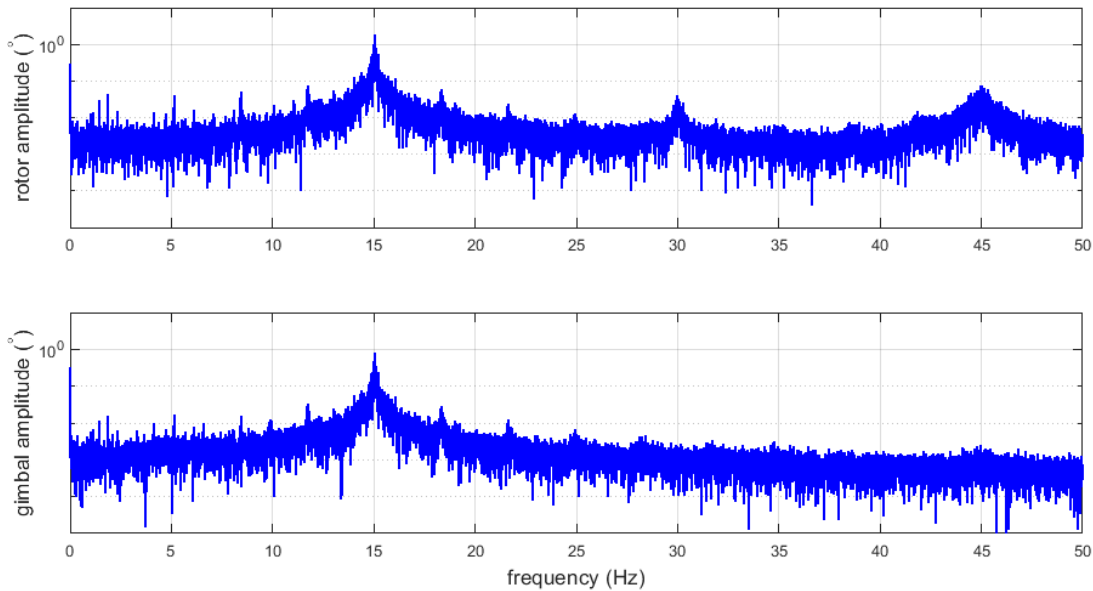


Figure 6.12. Frequency Content of the Rotor (Above) and Gimbal (Below) Angular Motion

Note that special effort went into keeping the fundamental frequencies of the rotor and gimbal close enough, as explained in the rotor and gimbal design section. Also, as evident from Figure 6.12, harmonics of the excitation frequency at the 30 and 45 Hz are also present at the rotor, but they are not as evident as the principal excitation at 15 Hz. The angular rate for the gimbal and rotor are given in Figure 6.13 for the duration of Run #2.

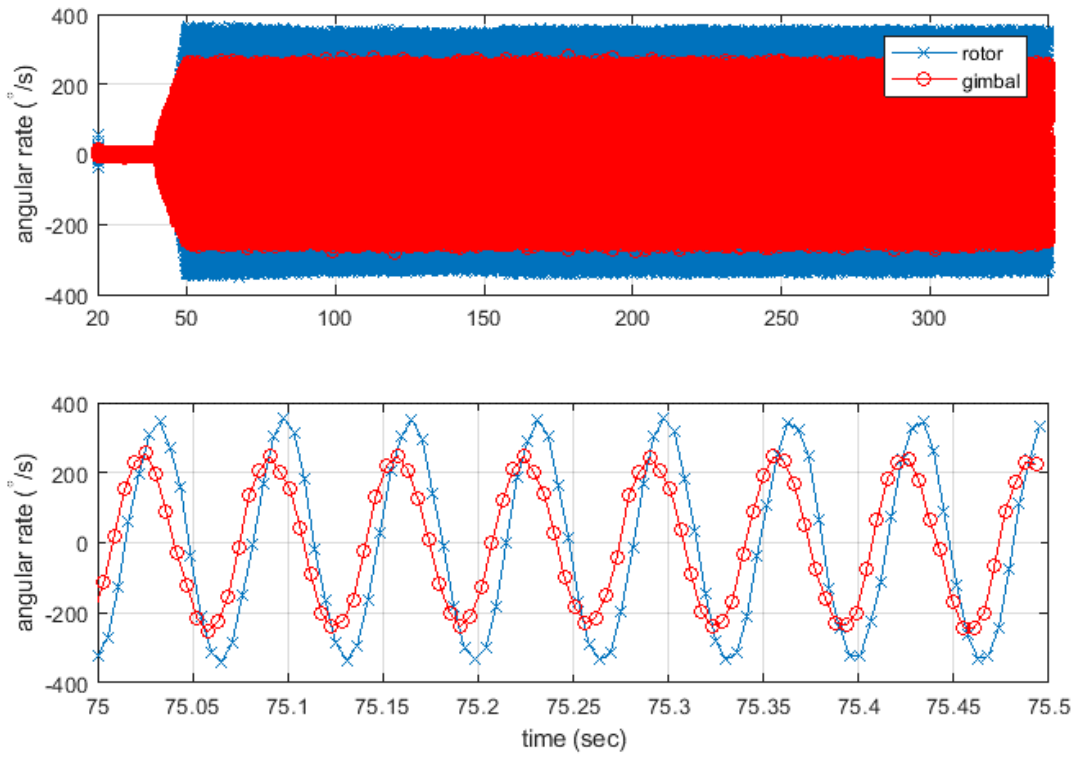


Figure 6.13. Rotor and Gimbal Angular Rates with Specific Detail at the 75th Second

Again, the details from the run around the 75th second are also presented the lower plot. The angular rate for the rotor oscillates from $-348.8 \text{ } ^\circ/\text{s}$ to $364.8 \text{ } ^\circ/\text{s}$ whereas the gimbal oscillates between $-283 \text{ } ^\circ/\text{s}$ and $280.9 \text{ } ^\circ/\text{s}$. Similar to the angle case, the intended phase difference between rotor and gimbal are also evident.

The angular momentum of the setup tray is obtained by combining the previously obtained air bearing angular rate data with the estimate of the setup tray moment of inertia.

To get such an inertia estimate, components of the experimental setup was first weighed (Figure 6.14) and their centers of mass were identified using the already existing load cell. Later, these were input to the existing CAD model of the setup (Figure 6.15) to get an estimate for the total inertia of the experimental setup tray and air bearing which was calculated to be $2.139\text{E-}2 \text{ kg-m}^2$.

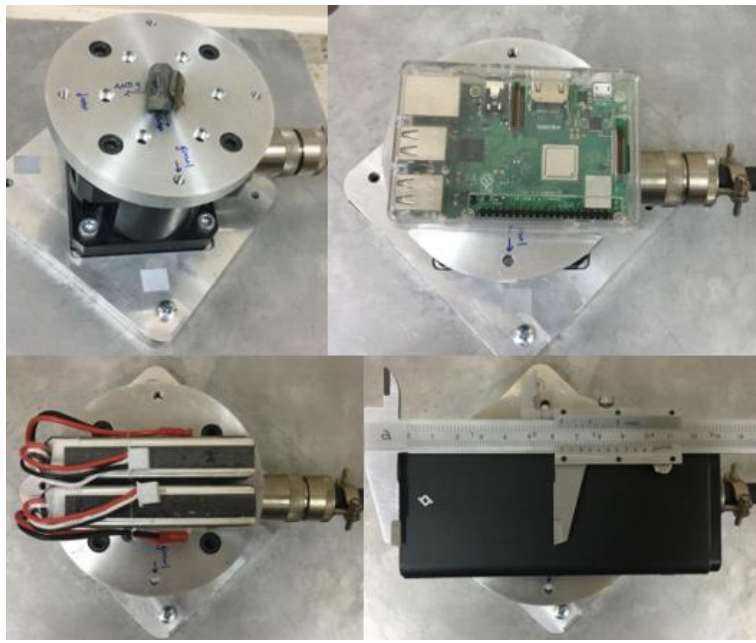


Figure 6.14. Weighing Campaign for the Setup Tray Elements to Identify Mass Properties. Starting from Top Left in Clockwise Direction; The Balance Mass, Raspberry Pi Computer, Battery Pack for The Computer and Battery Pack for The Actuator.

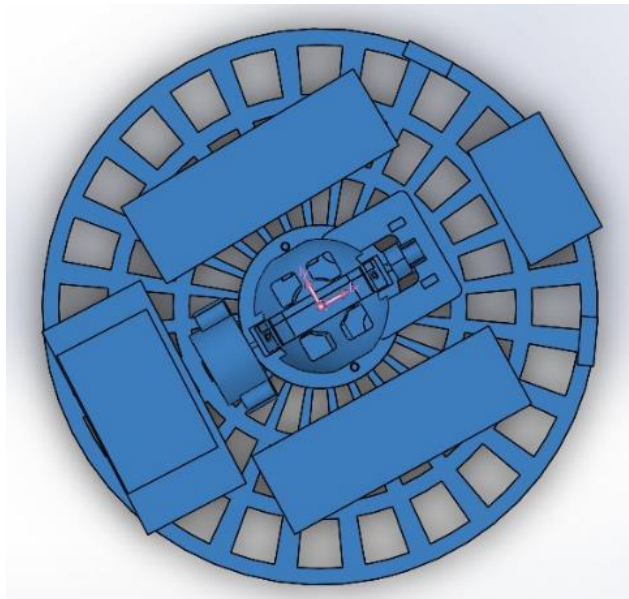


Figure 6.15. CAD Model to Which the Mass Measurements were Input and Moment of Inertia Estimate was Obtained.

Similarly, the angular momentum of the actuator is calculated utilizing the telemetry obtained from gimbal and rotor as formulated in Eq. (2.43). For the inertia value of the rotor, the estimates from CAD model was used, which corresponds to 2.139E-4 kg-m². The resulting values were filtered with a low-pass filter at 0.1 Hz to filter out the higher-order dynamics and to isolate the secular component of the actuator angular momentum, as previously done in section 4.3. Both the raw and the filtered actuator angular momentum data is presented in Figure 6.16 together with the air bearing angular momentum derived from the air bearing angular rate data provided in Figure 6.9.

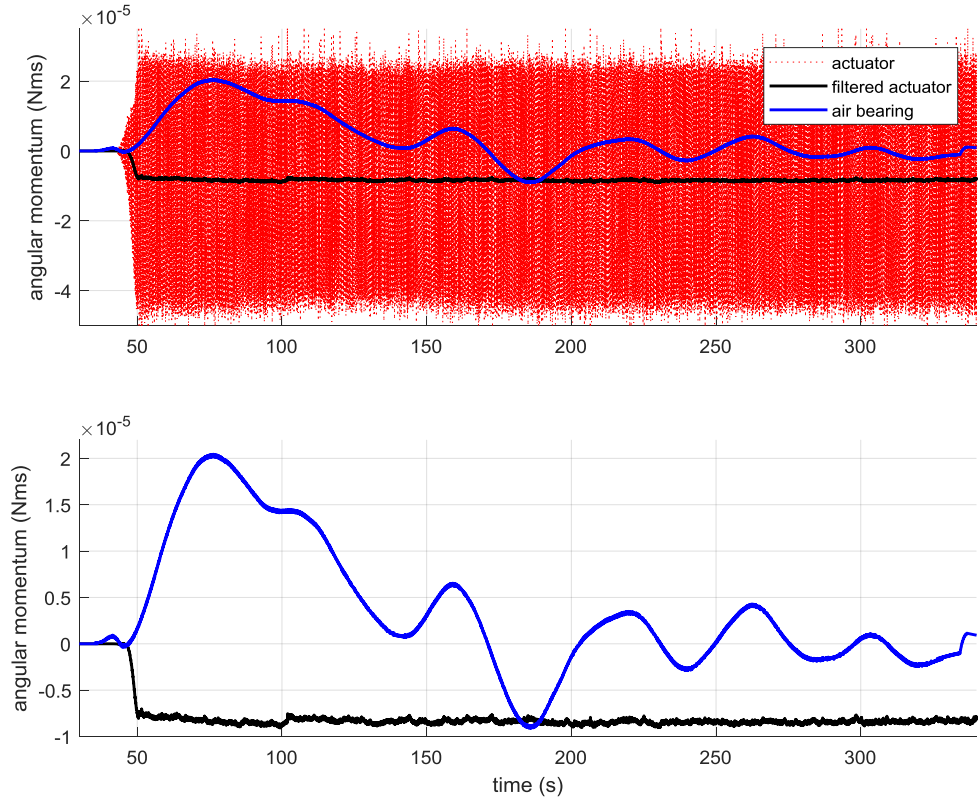


Figure 6.16. Comparison of Run #2 Encoder Derived Results with the Actuator Output.

As it can be inferred from Figure 6.16, even though the angular momentum output of the vibration based actuator is sinusoidal in nature, it also has a constant component. By conservation of angular momentum, this component leads to the rotation of the air bearing setup. However, air bearing settles (*i.e.* 0 Nms) after the 150th second, and starts oscillating about an equilibrium. This is possibly due to the inability of the device to overcome disturbance torques, such as gravity induced torques due to the inherent imbalance of the experimental setup. Nevertheless, even under such adverse conditions, the operation of the device managed to rotate the air bearing.

6.2.2.2. Telemetry from run #4

In this particular run, open loop gimbal and rotor input potential differences are as the following:

$$\begin{aligned} V_{gim} &= 2.25 \sin(2\pi 15t) \\ V_{rot} &= 1.95 \sin\left(2\pi 15t + \frac{232}{180}\pi\right) \end{aligned} \quad (6.4)$$

Note the input voltage phase difference of 232°. The resulting encoder angle history as well as angular rate derived from encoder angle measurements from Run #4 is presented in Figure 6.17. Again the maximum angular rate imparted by the device on the setup was 0.058 °/s, but this time in the opposite direction due to the different phase setting as predicted by the mathematical model.

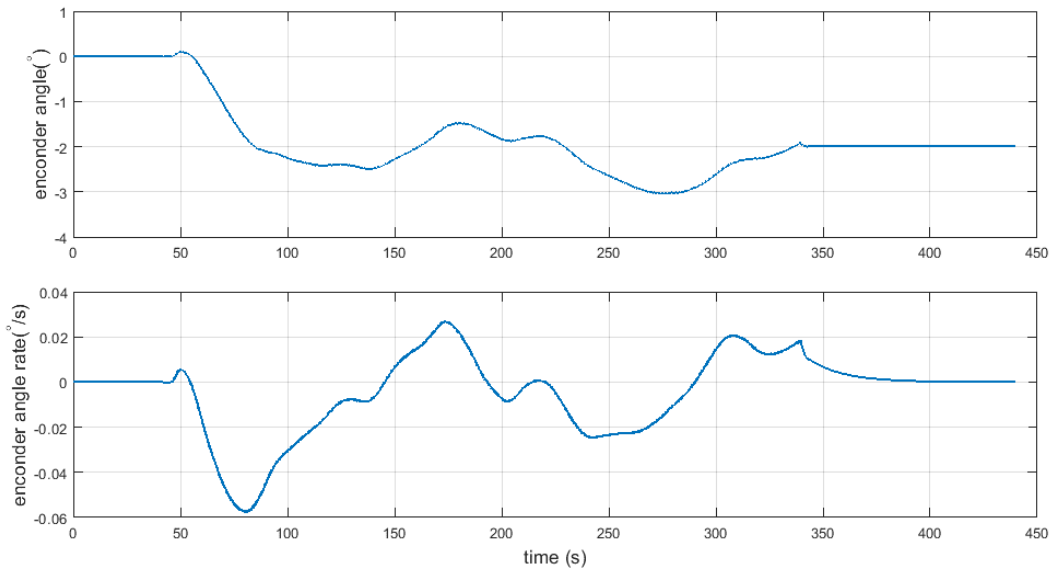


Figure 6.17. Encoder Angle and Angular Rate for Test Run #4

The frequency content of the air bearing angle is shown in Figure 6.18. Similarly, the spectrum is again extracted from 70th to 320th seconds. The DC content and the specific harmonic at the double of the applied input frequency are again observable. Recall that the DC content is observed since the air bearing conducts a rigid body rotation.

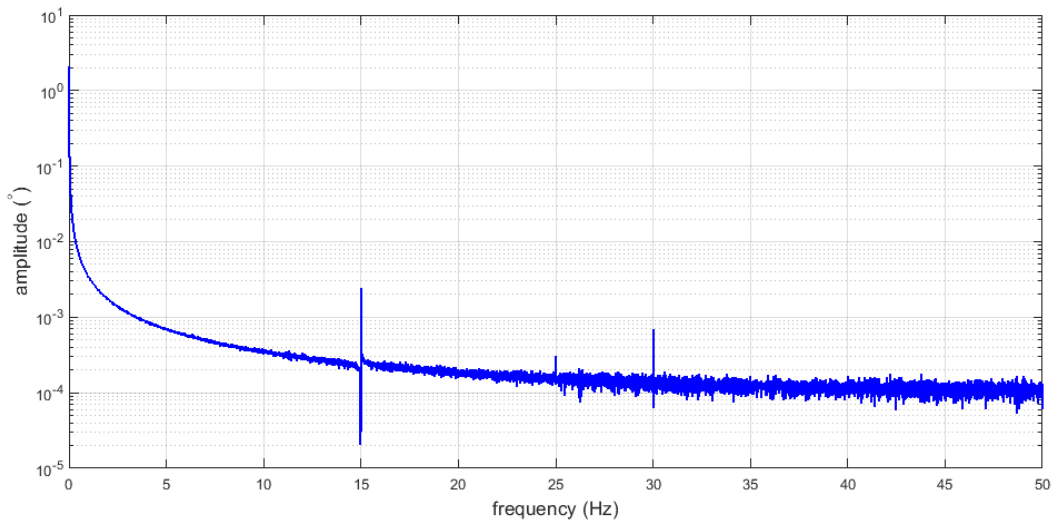


Figure 6.18. Frequency Content of Run #4

The resulting rotor and gimbal angles are presented in Figure 6.19:

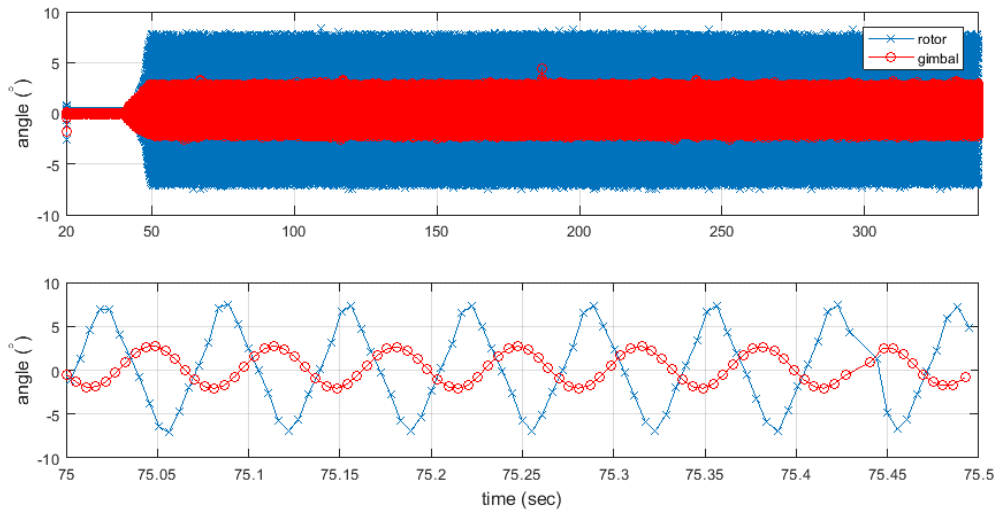


Figure 6.19. Rotor and Gimbal Angles with Specific Detail at the 75th Second

In Run #4, the rotor angle oscillates between -7.5° and $+7.8^\circ$ whereas the gimbal oscillates between -2.60° and $+3.10^\circ$. This time, the phase difference between the rotor and gimbal is much evident due to the increased phase difference value. The frequency content of the gimbal and rotor is again provided utilizing the angle data extracted from the interval spanning the 70th to 320th seconds.

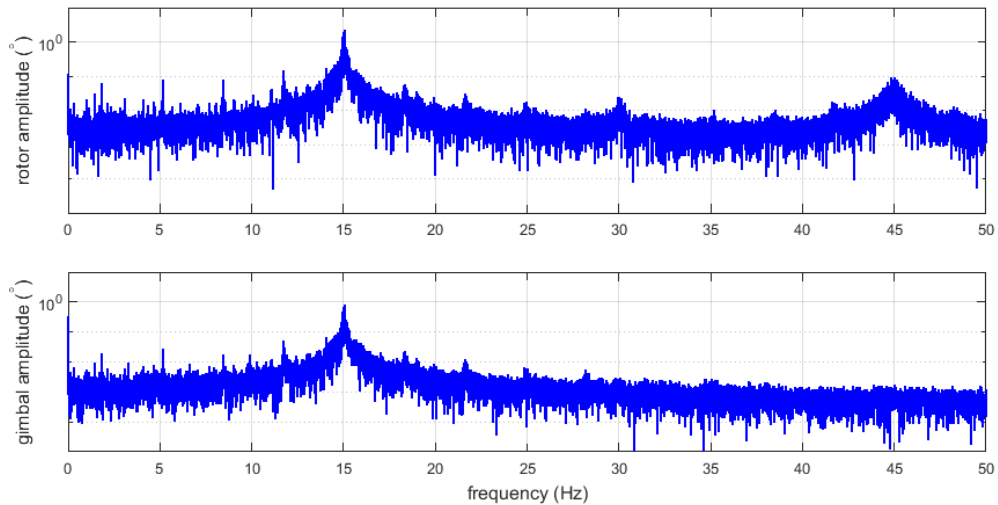


Figure 6.20. Frequency Content of the Rotor (Above) and Gimbal (Below) Angular Motion

Similar to the previous case, harmonics of the excitation frequency at the 30 and 45 Hz are also present at the rotor, but again they are not as emphasized as the principal excitation at 15 Hz. The angular rate for the gimbal and rotor are given in Figure 6.13 for the duration of Run #4.

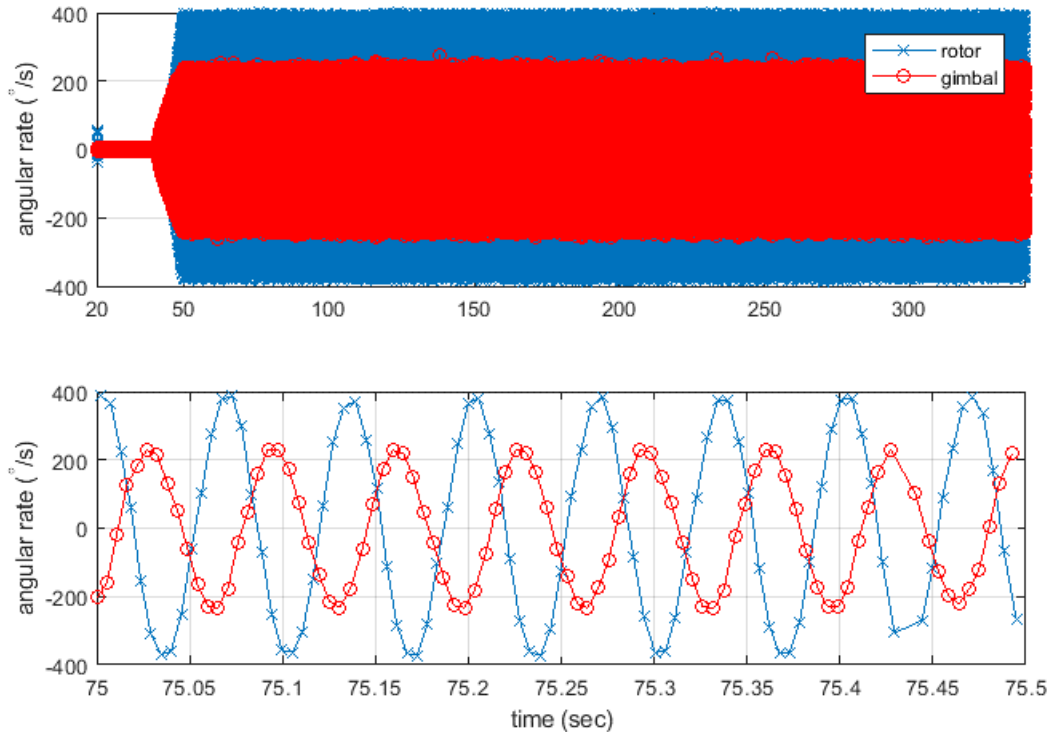


Figure 6.21. Rotor and Gimbal Angular Rates with Specific Detail at the 75th Second

Rotor angular rate oscillates from $-400 \text{ } ^\circ/\text{s}$ to $400 \text{ } ^\circ/\text{s}$ whereas the gimbal oscillates between $-227 \text{ } ^\circ/\text{s}$ and $230 \text{ } ^\circ/\text{s}$. Similar to the angle case, the intended phase difference between rotor and gimbal are also evident.

The angular momentum of the setup and the actuator were again obtained with the previously described method:

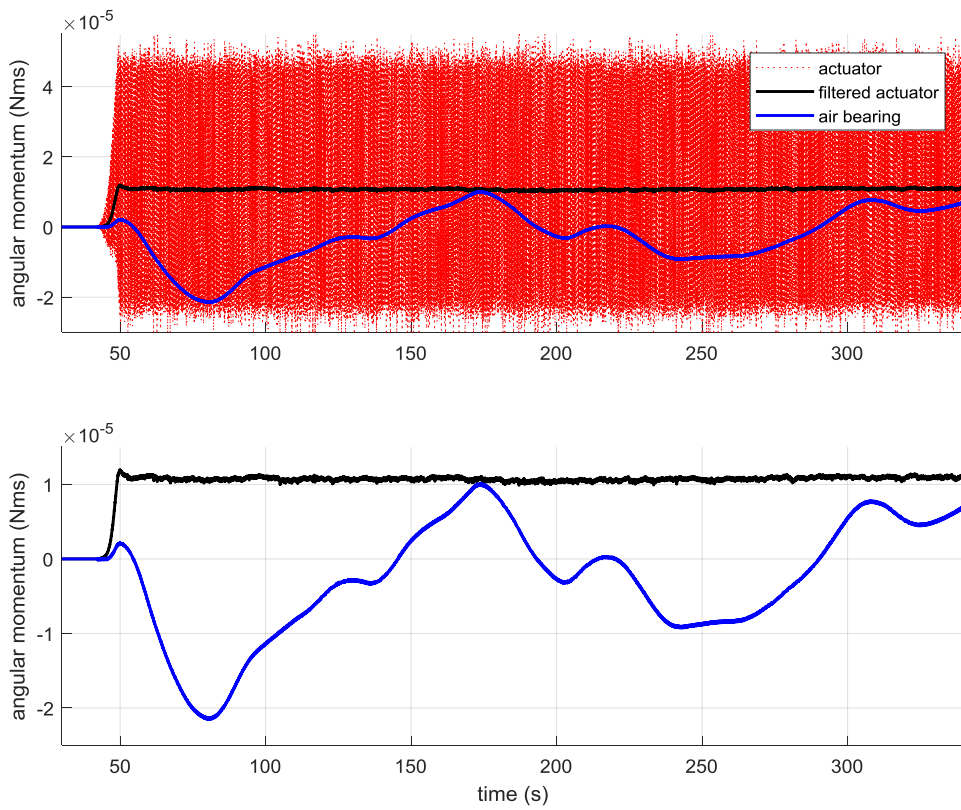


Figure 6.22. Comparison of Run #4 Encoder Derived Results with the Actuator Output

Note the opposite sense of motion in contrast with the results from Run #2, which was expected due to nearly 180° difference in the input phase (232° instead of 60°) as outlined by the $\sin(\sigma)$ term in (2.69). Again, the air bearing undergoes a limited rotation followed by oscillation around a certain equilibrium position. This is again probably due to imbalance disturbance torques.

6.3. Summary of Results

The actuator whose principals were provided in section 2.6 and design was elaborated in Chapter 3 was experimented upon utilizing different setups including a load cell and single-axis air bearing.

Results indicate close agreement with the analytical predictions even though disturbances from non-ideal experimental conditions were present. These were the

additional disturbances observed in load cell experiments (Figure 6.5) due to the dynamics introduced by padding and the effects of gravitational restoring torque stemming from experimental setup imbalance. However, in both experimental setups, the following indicative characteristics of a vibration based actuator outlined by Eq. (2.69) was observed; the presence of the main output having the frequency double that of the excitation and the ability to control the amplitude and direction of the output with the adjustment of input phase difference. Recall that, these are also the properties theorized in Ref. [12], confirming the “mechanical rectifier” nature of the current device.

All in all, the concept of satellite attitude manipulation via a vibration based actuator with a spherical rotor is experimentally proven. The next step would be to identify the application domains where such a device would be more advantageous than the traditional attitude actuators.

CHAPTER 7

A MEMS VIBRATION BASED ACTUATOR

Having proved the concept of VBA, the possibility of miniaturized attitude actuators will now be explored. As identified in section 1.4, miniaturizability is one of the key performances of next-generation satellite attitude actuators. The first half of the chapter assesses VBA performance in comparison with reaction wheels upon scaling down. This is done by carrying out dimensional analysis for important physical actuator parameters such as inertia and angular momentum. Such analyses are common in Microelectromechanical Systems (MEMS) domain to identify whether a device is suitable (and worthwhile) for miniaturization [86][87]. In this case, the ultimate aim is to determine if VBAs become more efficient performance-wise with respect to traditional reaction wheels upon scaled-down and if so, at what dimensions. Subsequently, an exploratory design study is conducted with that particular dimension to assess the feasibility of a MEMS based VBA. Furthermore, the operational concept and the resulting performance of such MEMS VBA is studied assuming a chip-scale host satellite.

7.1. A Case for Miniaturization

The aim of this section is to justify the miniaturization need of the spacecraft equipment. For this, first, the existing and prevalent trends of nanosatellites were introduced. Later, basic performance parameters of reaction wheels were introduced together with the parameters of rod-type VBA. These parameters were obtained as a function of equipment size. Subsequently, this model was utilized to carry out a scale-down study. This model was also correlated with the existing reaction wheel data from the market to further validate the approach.

7.1.1. Satellite Miniaturization Trend

An emerging trend in the satellite industry for the extensive utilization of small satellites (*i.e.* satellites having mass lower than 600 kg) exists. The number of satellite launches rose from about 150 in 2012 to over 450 satellites in 2018 while small satellites contributing to the majority of this figure. Over 1300 small satellites were launched in the 2012 – 2018 time span, 961 of them being CubeSats [36]. Cubesats are mainly being utilized in Remote Sensing missions, which can be described as “ADCS intensive” missions. One highlight is the deployment of 88 CubeSats of 3U size in a single launch by Planet Labs in 2017. Planet Labs operates a distributed system of nearly 200 small satellites to enable persistent imaging of the globe.

Having usually a volume of 10 cm by 10cm with a 30 cm of height and maximum mass of 4 kg (*i.e.* “the 3U size”) [37], it can be inferred that CubeSats now dominate the satellite market. The introduction (and subsequent adoption) of CubeSat standard lead to this proliferation.

To make space missions further accessible, other standards are also being proposed. PocketQube is such a standard [38], whose one unit (“1P”) corresponds to a cube of 5 cm side with a mass of no more than 250 grams. It is highly likely that this format would also proliferate across to industry as the CubeSat standard once did.

All in all, novel satellite equipment producers have to take trends such as miniaturization into account for introducing products that can easily be adopted, in addition to the usual equipment design goals such as low power, high performance, reliability, etc.

7.1.2. Actuator Performance and Dimensional Analysis

The purpose of this subsection is to point out the actuator performance parameters as function of actuator dimensions. Furthermore, figures of merit such a specific and volumetric angular momentum are also introduced. These activities are carried out for reaction wheel and rod-type VBA introduced previously in Ref. [30].

The rod-type VBA was specifically utilized instead of the spherical design that have been treated so far in this study. The rationale behind is to keep design adaptable to MEMS production. MEMS devices are planar structures; they are produced via micromachining (*i.e.* successive lithography and etching) of thin silicon wafers. A rod is a two dimensional planar structure whereas a sphere is a three dimensional construct. Hence, spherical rotor type VBA would have been incompatible with MEMS processes, thus rod-type VBA was chosen for further miniaturization analysis.

The CMGs were not included in the study. This is due to the fact that it is already established by Ref. [35] that reaction wheels are more suitable for small satellites. In that particular study, it was further identified that the reaction wheels are more efficient for spacecraft having moment of inertia lower than 0.1 kg-m^2 . The spacecraft discussed so far (CubeSats and PocketQubes) have substantially lower inertia than this particular value.

In order to carry out a dimensional analysis, the performance parameters of reaction wheels as well as VBAs have to be obtained as a function of actuator dimensions. Starting off with an expression of RW angular momentum,

$$H_{rw} = J_{rw}\omega_{rw} \quad (7.1)$$

where, J_{rw} is the wheel moment of inertia and ω_{rw} is the wheel angular speed. Assuming the reaction wheel rotor to be thin hollowed out disc with inner radius r_1 and outer radius r_2 ; its moment of inertia can be obtained from the expression:

$$J_{rw} = \frac{1}{2}m_{rw}(r_1^2 + r_2^2) \quad (7.2)$$

where m_{rw} is the rotor mass and can be obtained via:

$$m_{rw} = \rho\pi h(r_2^2 - r_1^2) \quad (7.3)$$

Here, ρ is the density and h is the disc height. Inserting Eq. (7.3) into Eq. (7.2):

$$J_{rw} = \frac{1}{2} \rho \pi h (r_1^4 - r_2^4) \quad (7.4)$$

Upon inspection, it is evident from the above identity that the moment of inertia has 5th order dependency to the equipment dimensions (*i.e.* r and h). Assuming a scaling factor η , a scaled moment of inertia would take the form:

$$J_{rw}^* = \eta^5 \underbrace{\frac{1}{2} \rho \pi h (r_1^4 - r_2^4)}_{J_{rw}} \quad (7.5)$$

Now, let us determine the relationship between the dimension of the reaction wheel and the rotation speed. For this, data from the existing reactions wheels in the market were compiled. Figure 7.1 presents the maximum angular speeds of various reaction wheels together with their size:

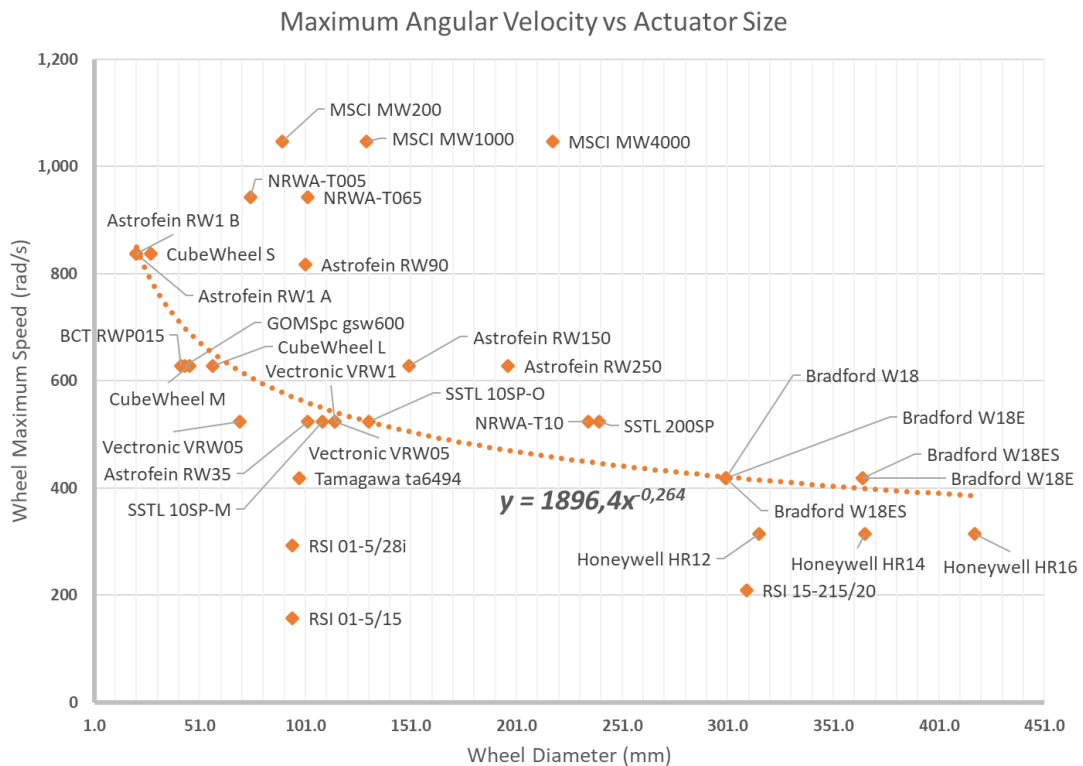


Figure 7.1. Correlating Maximum Reaction Wheel Angular Speed with Respect to Their Size

Note that, even though the fitted curve does not provide a one-to-one representation, the following mathematical identity establishing a relationship between reaction wheel physical size and speed is obtained:

$$\omega_{rw} = 1869.4 \times (2r_2)^{-0.26} \quad (7.6)$$

Note that, this mathematical relation identifies the trend of higher rotational speeds with more compact reaction wheels. Carrying out a similar analysis as done with the wheel inertia, the angular speed of the scaled reaction wheel will have the following relationship in terms of the initial reaction wheel's angular speed:

$$\omega_{rw}^* = \eta^{-0.26} \omega_{rw} \quad (7.7)$$

So, the angular momentum of a re-dimensioned rotor can be obtained as:

$$H_{rw}^* = J_{rw}^* \omega_{rw}^* = \eta^{4.74} J_{rw} \omega_{rw} = \eta^{4.74} H_{rw} \quad (7.8)$$

We may conduct a similar analysis also for the rod-type VBA. Recalling from Eq. (2.66), its output can be quantified by:

$$H_{rod} = 2\pi f \Phi \Theta J_{rod} \quad (7.9)$$

The angles Θ and Φ are indifferent to scaling. Recall that the moment of inertia scales independent of the rotor shape as follows:

$$J_{rod}^* = \eta^5 J_{rod} \quad (7.10)$$

However, VBA has the frequency excitation term f in contrast to the wheel angular momentum expression. Henceforth, a scaling analysis of this term also has to be carried out. Recalling the definition of natural frequency:

$$f = \frac{1}{2\pi} \sqrt{\frac{k}{m}} \quad (7.11)$$

Where k is the stiffness and m is the mass. Assuming a cantilever structure (which is common in MEMS devices), the stiffness can be formulated from the definition of a cantilever beam:

$$k = \frac{3EI}{L^3} = E \frac{Wt^3}{4L^3} \quad (7.12)$$

Here, E is the modulus of elasticity; I is the section moment of inertia; L, t and H are the beam length, thickness and height respectively. Let us also assume a rectangular prismatic proof mass m :

$$m = \rho hwl \quad (7.13)$$

Similar to the previous case, multiplying all the dimensional parameters with η for scaling:

$$f^* = \frac{1}{2\pi} \sqrt{\frac{\eta}{\eta^3} E \frac{Wt^3}{4L^3} \frac{1}{\rho hwl}} \quad (7.14)$$

Upon simplification:

$$f^* = \underbrace{\frac{1}{\eta} \frac{1}{2\pi} \sqrt{E \frac{Wt^3}{4L^3} \frac{1}{\rho hwl}}}_{f} = \frac{f}{\eta} \quad (7.15)$$

Thus, introducing Eqs. (7.15) and (7.10) into Eq. (7.9), the scaled VBA expression for the angular momentum is obtained as:

$$H_{rod}^* = \eta^4 H_{rod} \quad (7.16)$$

Upon comparing equations (7.8) and (7.16), one can arrive at the following conclusion; for scaling up (*i.e.* $\eta > 1$) the classical reaction wheel outperforms the rod since its angular momentum expression scales with 4.74th power in comparison; having a power to the 0.74 advantage. However, for the opposite case of “scaling down” (*i.e.* $\eta < 1$), the VBA becomes advantageous. Hence, it is mathematically shown that VBA actuators are more suitable for miniaturization in comparison with the classical reaction wheel actuator.

7.1.3. Results

In the previous section, the trends in miniaturization for the angular momentum of both reaction wheel and VBA were identified. The remaining question is at which dimensions VBA angular momentum capabilities surpass the classical reaction wheel's capabilities. To determine this, data from actual equipment were utilized. The equipment presented in Table 7.1 and Table 7.2 were utilized. In Table 7.1, data representing the Rockwell Collins RSI 15-215 reaction wheel are presented. To construct the reaction wheel angular momentum scaling curve, this data was utilized as the starting point. Similarly, data in Table 7.2 is obtained from the Ref. [30]. It is adjusted to account for the utilization of silicon as rotor material in contrast to the steel which was the actual material utilized in the rod-type VBA prototype.

Table 7.1. *RSI 15-215 Reaction Wheel Estimated Data [39]*

Parameter	Value	Unit
Outer Rotor Diameter	296	mm
Inner Rotor Diameter	244	mm
Max Angular Velocity	263	rad/sn
J_{rw}	0,0742	kg-m ²
ρ_{rotor}	2700	kg/m ³

Table 7.2. *Rod-type VBA [30]*

Parameter	Value	Unit
Rod Length	181.5	mm
Rod Diameter	15	mm
Natural Frequency	38	Hz
J_{rod}	2.06x10 ⁻⁴	kg-m ²
ρ_{rod}	2328	kg/m ³

Additional figures of merit were also introduced. These are the specific angular momentum and volumetric angular momentum. Specific angular momentum

corresponds to the angular momentum per unit mass of the actuator; it is a figure of merit exhibiting how effective is the mass of the actuator being utilized. Similarly, the volumetric momentum showcases the effectiveness of the actuator per unit volume.

Additional data were also collected from the available reaction wheels in the market [40]-[73]. This data was utilized to assess whether their angular momentum capacities and dimensions corroborate the scaling model developed in the previous section. The result is presented in Figure 7.2.

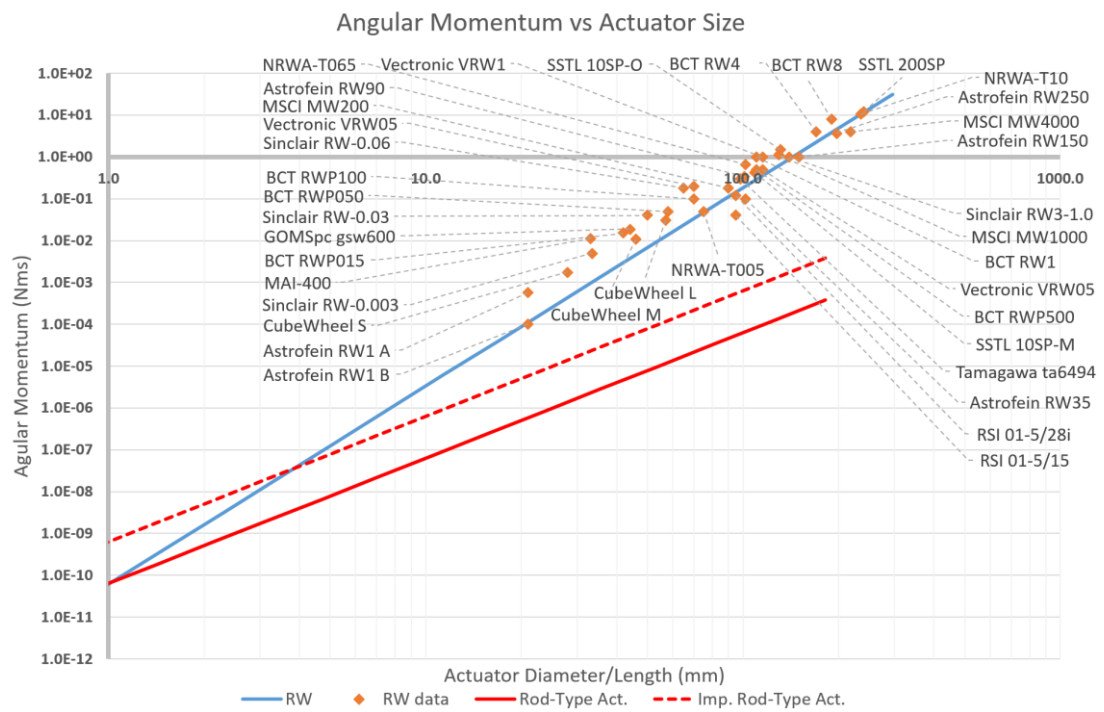


Figure 7.2. Scaling Analysis Comparison of VBA and RW Angular Momentum

Upon inspection of Figure 7.2, it is evident that the scale-down model is in close agreement with the existing RW data. Additionally, a curve named “Improved Rod-type Act.” can also be observed. Its purpose is to showcase the capability of VBA if a performance optimized design was made. The existing designs so far (*i.e.* the spherical VBA and the rod-type VBA in Figure 2.3) are laboratory prototypes manufactured to prove the VBA concept, they are not the optimized industrial products. For instance,

notice how small are the magnets in Figure 2.3 in comparison to the actuator itself. An optimized actuator would have more of that elements, likely yielding higher performance. Hence, it can be assumed that VBA performance can be increased tenfold with an optimized design, and the previously mentioned curve accounts for this possibility and provides a more objective comparison.

Also, note that the smallest commercially available RW has a diameter of 20 mm (*i.e.* Astrofein RW1 A & B). No COTS momentum exchange device smaller than this have been observed. As a side note, recall that the size of PocketQube standard satellite is 5 cm; hence even the smallest RWs can be considered too large for that particular platform.

The volumetric angular momentum scale-down analysis is presented in Figure 7.3:

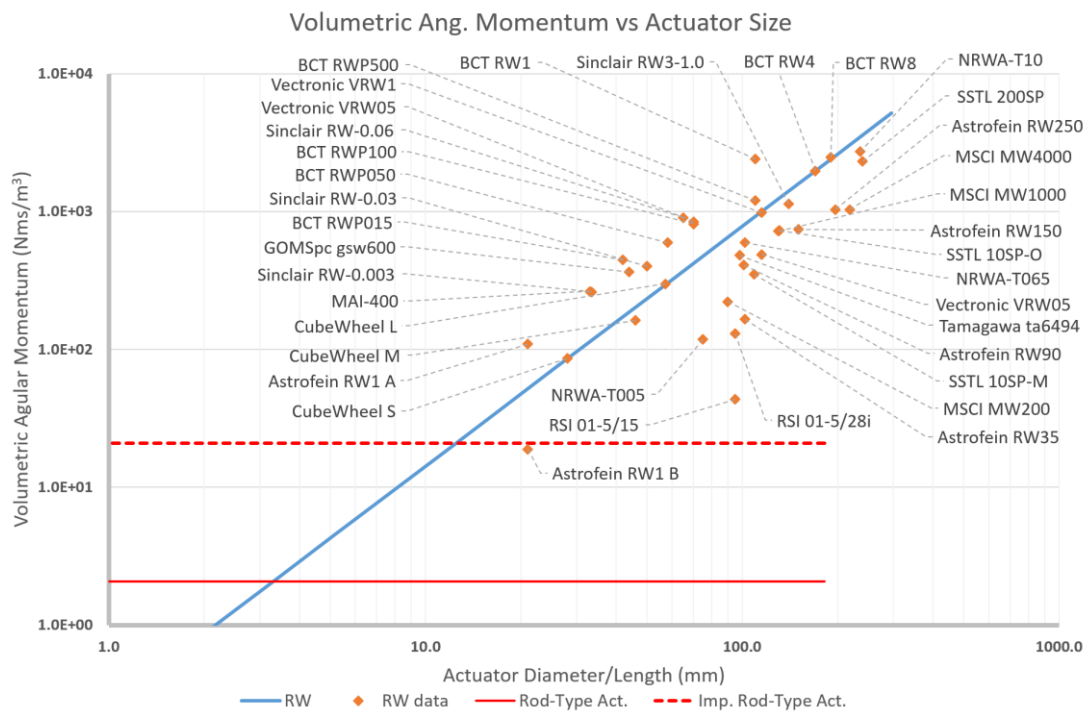


Figure 7.3. Scaling Analysis Comparison of VBA and RW Volumetric Angular Momentum

It can be observed that the ultra-small reaction wheels mentioned earlier have substantially lower volumetric angular momentum performance. This may be due to the fact that in those cases inner elements of such RWs are not specifically manufactured, and are commercially existing components that are not specially designed for the particular RW.

The specific angular momentum comparison is exhibited in Figure 7.4:

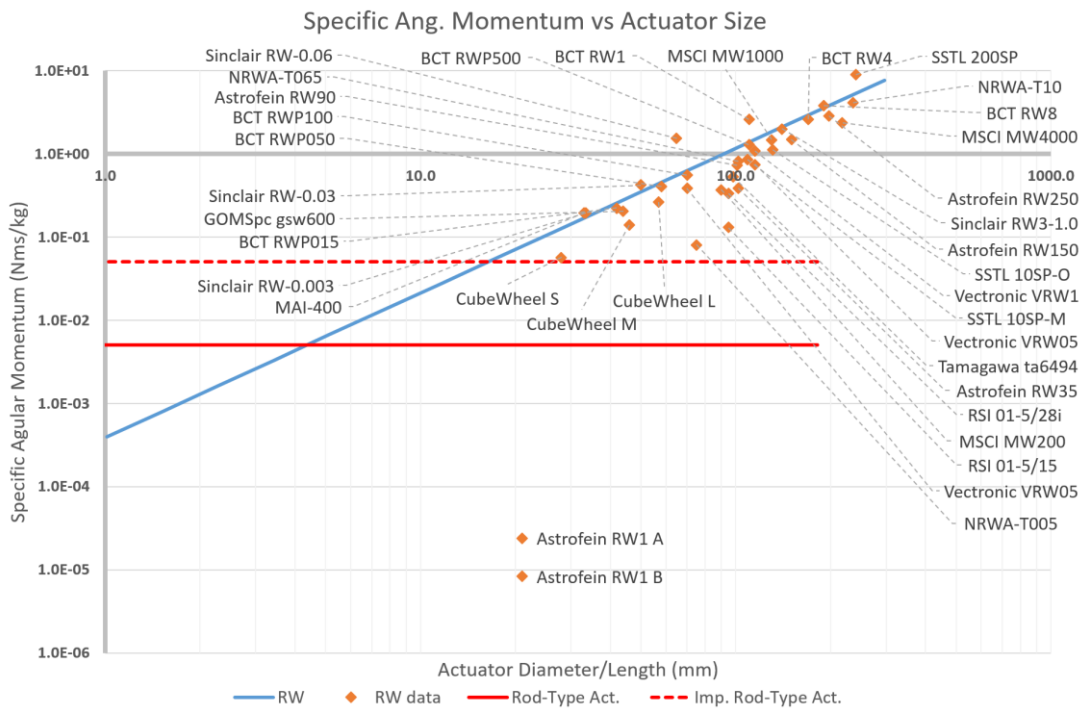


Figure 7.4. Scaling Analysis Comparison of VBA and RW Specific Angular Momentum

One striking observation from Figure 7.3 and Figure 7.4 is the invariance of VBA volumetric and specific angular momentum against actuator dimension. This is in sharp contrast with respect to the traditional RW actuator.

The poor performance of RW also exist in the specific angular momentum domain. All in all, it can be deduced from the figures that, for a diameter/length lower than 20 – 30 mm, VBAs tend to surpass the traditional momentum exchange devices from the

performance perspective. Next, a rod-type VBA within the aforementioned dimension envelope will be designed and studied, but this time utilizing MEMS approach.

7.2. MEMS Based VBA Architecture

The architecture of a MEMS based VBA involves the rotor, actuators and spring structures utilized to set the device to certain operating frequency. For the MEMS VBA, the rotor is a rod-type structure which carries out sinusoidal motion in different axis with phase difference as outlined in Eq. (2.65).

A general depiction of the actuator is presented in Figure 7.5. Here, four chevron thermo-mechanical actuators (TMA) can be observed as connected to a rod-like structure. A symmetric set of TMAs are also situated underneath (the system is symmetric with respect to the plane defined by x- and z- axes). These total of eight actuators pull the rotor in a pre-selected order to create the oscillation described in Eq. (2.1), around x- (*i.e.* gimbal) and y- (*i.e.* rotor) axes respectively.

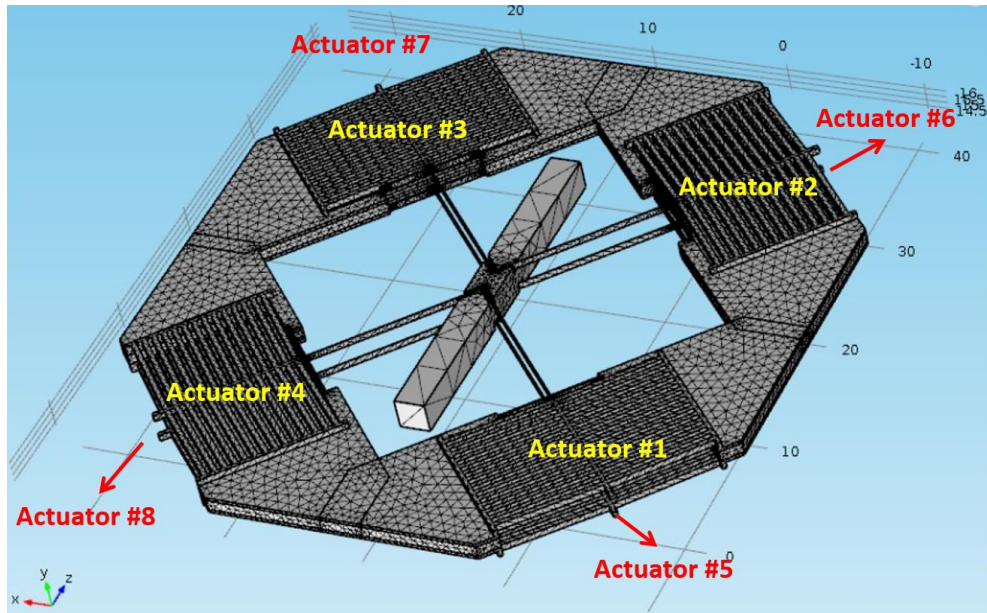


Figure 7.5. Enumerated Actuators. Topside and Bottom Actuator Placement are Indicated by Different Coloring.

This particular choice of actuators (*i.e.* TMAs) will be elaborated upon in the upcoming parts of this chapter. Near the actuators, are the spring structures made of

cantilever beams. These ensure the actuator, to be compliant with the rod motion. The spring and shaft structures are utilized to adjust the operating frequency and compliance of the system. They are composed of MEMS beam like structures. The spring and shaft structures can be observed from the detail presented in Figure 7.5.

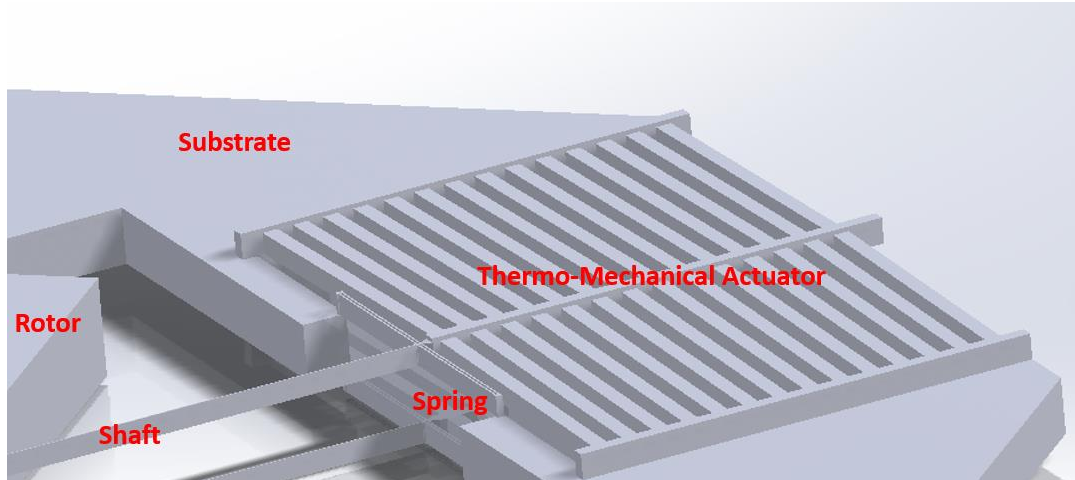


Figure 7.6. Spring and Shaft Structures Together with Their Connection to the TMA

One ultimate note would be that the resulting device is not intended to be a final product or a blueprint for production, ready to be sent to a MEMS foundry. Rather, it should be considered as a design exploration aimed to identify the underlying challenges that awaits MEMS VBA design process.

7.3. Actuator Design

7.3.1. Justification for TMA Utilization

Thermo-mechanical actuators (TMA) are chosen for their several different advantages over other MEMS actuation methods. They enable high force application in combination with large travel distances, unlike electrostatic actuators such as comb drives. As it will be described in the following sections, high force and displacement capability is the main driver for the current application. Other contenders at this

category are piezoelectric and magnetic actuators, however, they lack the simpler fabrication ease of thermal actuators [74].

Another shortcoming of TMAs in comparison to piezoelectric actuators is the lack of fast switching capability, yet TMAs can reach switching frequencies up to 1000 Hz which is more than adequate for the use case considered in this study [74].

An additional advantage of TMAs is the availability of room for improvement and optimization depending on the application. For instance, by altering the TMA beam cross-section; TMAs can be optimized to have 30% more thermal strain, actuator stroke can be improved by four folds and power consumption can be reduced 90% [76]. Chevron type TMAs are preferred over parallel (or bimorph) type TMAs because they are more area efficient and do not sacrifice stroke length for a given force output [75]. One point of discontent for chevron type TMA is the fact that such devices can reach temperatures such as 1000 Kelvins during operation, yet the heated elements are small and thermal energy can dissipate rather promptly [75].

7.3.2. TMA Placement

As mentioned earlier, TMAs are unidirectional linear actuators. Yet, the rotor has to undergo a complex rotational oscillatory motion. Hence, the design challenge lies in connecting such devices to the rotor in order to facilitate rotational motion.

The force applied by the TMAs are exhibited in Figure 7.7. As mentioned earlier, eight TMAs are utilized in conjunction to actuate the rotor. Since TMAs are unidirectional, forces are considered to be in “pulling” direction with respect to the rotor.

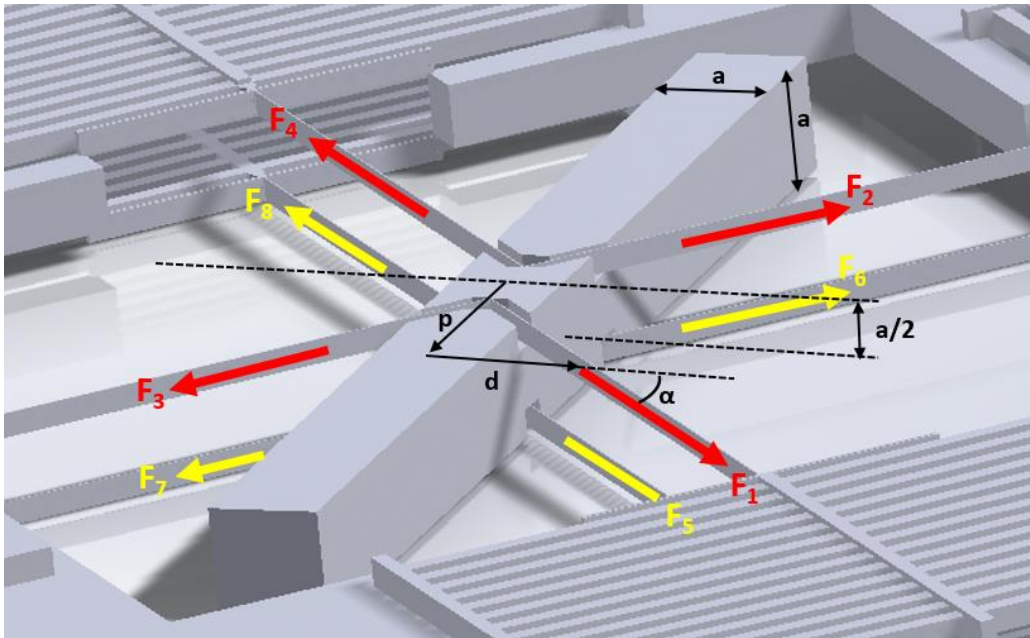


Figure 7.7. Forces Being Applied by TMAs on the Rotor

The resulting torques acting on the rod-type VBA can be formulized by the following equations:

$$\begin{aligned}
 T_x &= (F_1 + F_4 + F_6 + F_7 - F_2 - F_3 - F_5 - F_8) \frac{a}{2} \sin(\alpha) \\
 T_y &= (F_1 + F_3 + F_5 + F_7 - F_2 - F_4 - F_6 - F_8)(p \cos(\alpha) - d \sin(\alpha)) \quad (7.17) \\
 T_z &= (F_3 + F_4 + F_5 + F_6 - F_1 - F_2 - F_7 - F_8) \frac{a}{2} \cos(\alpha)
 \end{aligned}$$

Note that, we desire no torque acting in the z- direction; hence selection of p, d and α must be made in such a fashion that the torque around x- axis T_x must be sinusoidal with a phase difference of σ with respect to the T_y (*i.e.* torque around y- axis) whereas T_z must be kept to a bare minimum or zero, if possible. Moreover, we desire T_x to be equal to T_y in magnitude, so that rotation amplitudes at x- and y- axis would be identical.

An optimization study was carried out with aiming such properties. This involved minimizing,

$$\frac{T_x - T_d \sin(2\pi ft)}{T_y - T_d \sin(2\pi ft + \sigma)} \frac{T_y - T_d \sin(2\pi ft + \sigma)}{T_z} \quad (7.18)$$

By adjusting p, d and α such that,

$$\begin{aligned} p, d, \alpha &\geq 0 \\ F_i &\geq 0 \end{aligned} \quad (7.19)$$

It turned out that the optimal solution would have $p = a/2$ and $d = 0$ and $\alpha = 45^\circ$ with the force application distributed among the TMAs as follows:

$$F_i(t) = \begin{cases} F \sin(2\pi ft + \sigma_i + n_i), & \text{if } \sin(2\pi ft + \sigma_i + n_i) > 0; \\ 0, & \text{if } \sin(2\pi ft + \sigma_i + n_i) \leq 0; \end{cases} \quad (7.20)$$

Where

$$\sigma_i = \begin{cases} 0, & \text{if } i = 1, 4, 5, 8; \\ \sigma, & \text{if } i = 2, 3, 6, 7; \end{cases} \quad (7.21)$$

And,

$$n_i = \begin{cases} 0, & \text{if } i = 1, 3, 4, 7; \\ \pi, & \text{if } i = 2, 5, 6, 8; \end{cases} \quad (7.22)$$

For an illustrative representative case $F = 1$ and $\sigma = 90^\circ$, the forcing functions and the resulting torques are presented in Figure 7.8 and Figure 7.9, respectively.

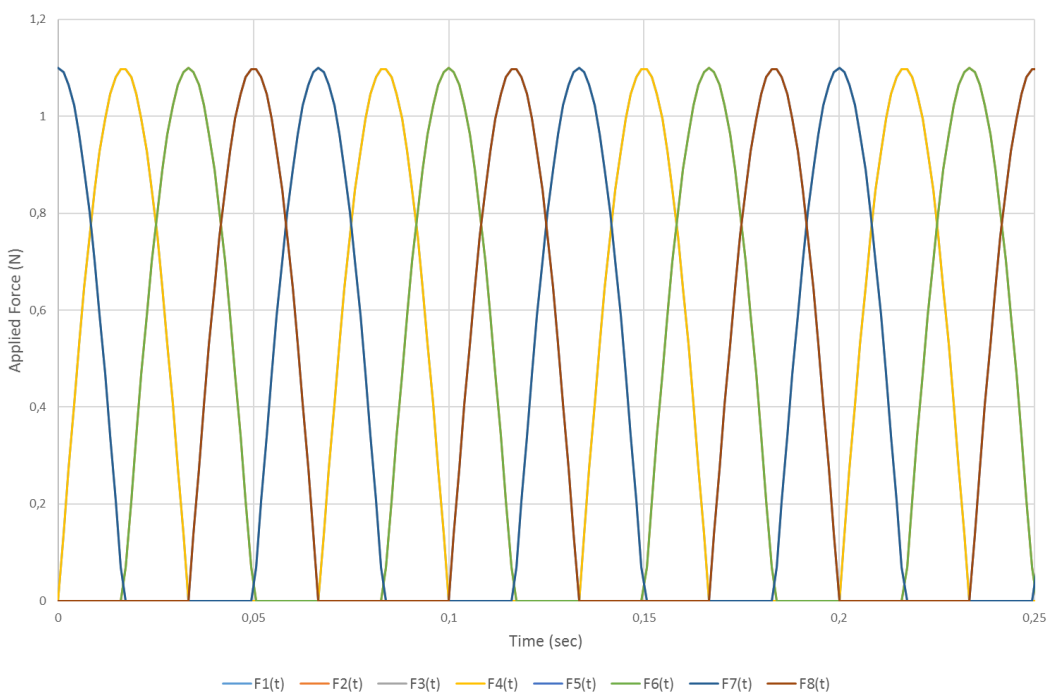


Figure 7.8. Pulling Forces Applied by Individual TMAs

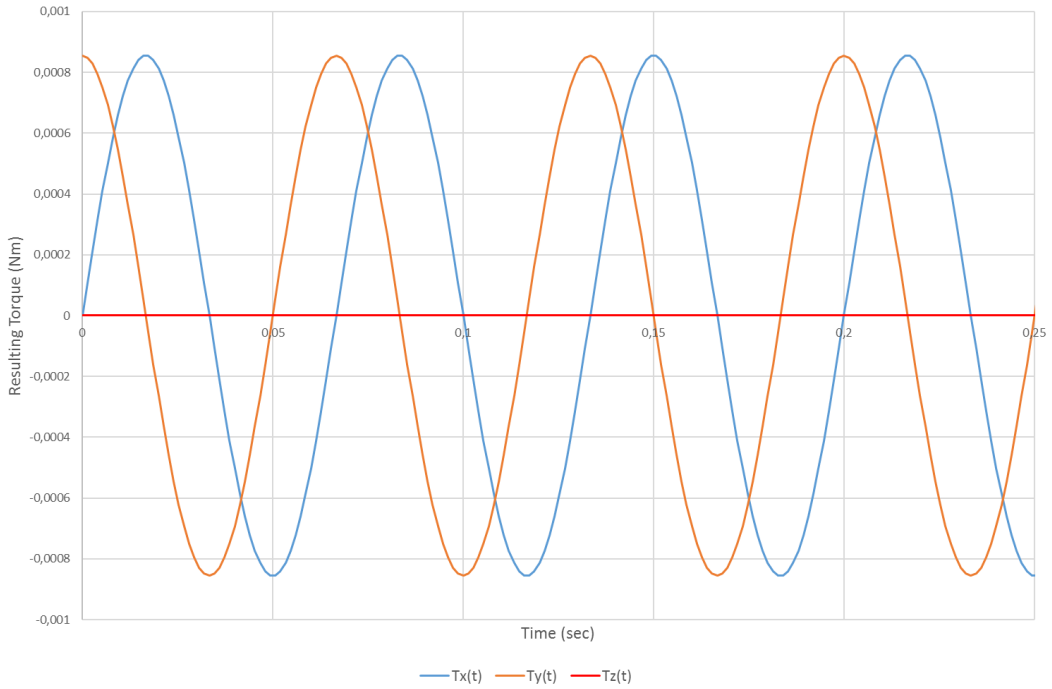


Figure 7.9. Torque Resulting from Compound Application of Force by the TMA array

Note that, at a given instant, at least two forcing functions are non-zero meaning that only two TMAs are active. Also of note is how T_z is minimal yet T_x and T_y have similar magnitudes as well as the desired 90° phase difference

7.3.3. Determining TMA Force and Stroke

From the previous chapter the it was found that

$$m_{rod} = \rho L_{rod} d_{rod}^2 \quad (7.23)$$

The inertia of the rod can be defined as

$$J_{rod} = \frac{m_{rod}}{12} (L_{rod}^2 + d_{rod}^2) \quad (7.24)$$

Recalling the expression for the angular momentum of a rod-type VBA under oscillatory actuation with a phase difference of $\sigma = 90^\circ$ as defined in Eq. (2.65):

$$H_{rod} = 2\pi f \Phi \Theta J_{rod} \quad (7.25)$$

For the sake of argument, assuming the oscillation magnitude are equal such that

$$\Theta, \Phi = \beta \quad (7.26)$$

Hence

$$H_{rod} = 2\pi f \beta^2 J_{rod} \quad (7.27)$$

Under such conditions, the magnitude for angular rate and angular acceleration can be defined as:

$$\begin{aligned} |\omega_{rod}| &= 2\pi f \beta \\ |\alpha_{rod}| &= 4\pi^2 f^2 \beta \end{aligned} \quad (7.28)$$

Thus, the torque required to actuate the rod can be obtained via the following identity:

$$\tau_{rod} = J_{rod} |\alpha_{rod}| \quad (7.29)$$

However, we are concerned with linear rather than the rotational actuators. Hence, we would like to have the force expression. Moreover, there would be several actuators

acting on the rod-type VBA to apply rotational motion. Assuming the active number of actuators to be N_{act} , the expression for the force becomes:

$$F_{rod} = \frac{1}{N_{act}} \frac{\tau_{rod}}{d_{arm}} \quad (7.30)$$

Lastly, the displacement expected from the actuators should be quantified. This is calculated via:

$$u_{rod} = \frac{a}{2} \frac{\beta}{\tan(\alpha)} \quad (7.31)$$

7.3.4. Thermo-Mechanical Actuator (TMA) Design

A chevron type TMA was utilized to generate the required force and stroke for the rotor actuation. A simplified depiction of such an actuator is presented in Figure 7.10.

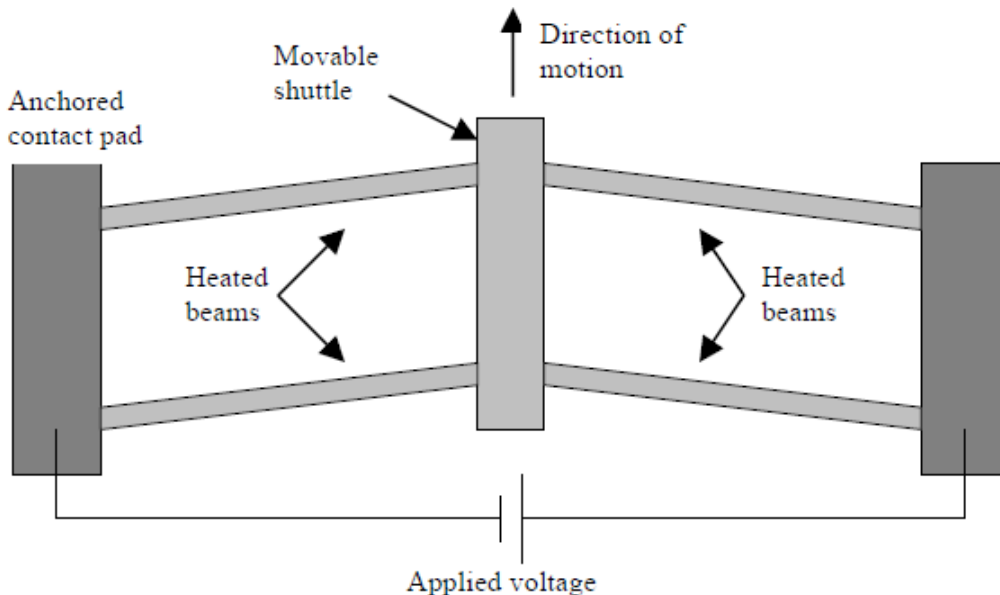


Figure 7.10. A Simplified Depiction of a TMA [77]

Basically, it is a hanging structure composed of beams carrying a shuttle. The TMA is anchored to the substrate at both ends. The beams are angled so that their thermal expansion would move the shuttle in a predefined direction. The thermal expansion is induced by applying a voltage difference at the anchors, resulting in current flow. This current flow leads to Joule heating and hence, thermal expansion of the beams.

Notice that the representative actuator shown in Figure 7.19 is composed of two buckle beam elements. A detail of a single buckle beam element and its dimensions and exhibited in Figure 7.20.

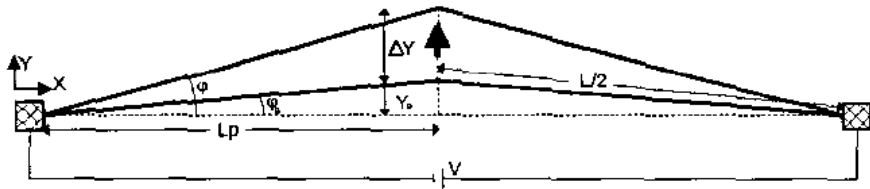


Figure 7.11. A Single Buckle-Beam Element [78]

The stroke of the actuator can be quantified from the following relation [78]:

$$\Delta Y = \left(\frac{L + \Delta L}{2} \right) \sin \left[\cos^{-1} \left(\frac{2L_p}{L + \Delta L} \right) \right] - Y_0 \quad (7.32)$$

Here, L is the buckle beam length, L_p is the lateral projection at L/2 and Y₀ is the initial position of shuttle, and ΔL is the buckle beam elongation due to Joule heating. It can be quantified by,

$$q_{gen} = \frac{V_{ops}^2}{R(T)V_{beam}} \quad (7.33)$$

Here, V_{ops} is the applied voltage, R(T) is the electrical resistance of the buckle beam and V_{beam} is the buckle beam volume. The electrical resistance is formulated by,

$$R(T) = \frac{\rho(T)L}{Wt} \quad (7.34)$$

Where L is the length, W is the width and t is the thickness of the beam. The unit length resistivity $\rho(T)$ is formulated for polysilicon as a function of temperature in Ref. [77] as:

$$\rho(T) = \begin{cases} T(2.9713 \times 10^{-2}) + 20.858, & \text{if } T < 300^\circ C \\ T^2(6.16 \times 10^{-5}) - T(7.2473 \times 10^{-3}) + 26.402, & \text{if } T \geq 300^\circ C \text{ & } T < 700^\circ C \\ T(8.624 \times 10^{-2}) - 8.8551, & \text{if } T > 700^\circ C \end{cases} \quad (7.35)$$

In similar fashion, the coefficient of thermal expansion $\alpha(T)$ is formulated in Ref. [77] as;

$$\alpha(T) = \left(3.725 \left(1 - e^{-5.88 \times 10^{-3}(T-125)} \right) + T(5.548 \times 10^{-4}) \right) \times 10^{-6} \quad (7.36)$$

Where this time temperature T is in Kelvin. Lastly, the thermal conductivity can be described by,

$$K(T) = \frac{1}{-T^3(2.2 \times 10^{-11}) + T^2(9.0 \times 10^{-8}) - T(1 \times 10^{-5}) + 0.014} \quad (7.37)$$

Here temperature is again in C° . The resulting force by the TMA can be calculated using the displacement ΔY obtained previously in Eq. (7.32):

$$F = N_{beam} \frac{EW^3t}{4L^3} \Delta Y \quad (7.38)$$

Here, N_{beam} is the number at buckle beams in the chevron structure whereas E is the modulus of elasticity. Multiple buckle beams can be utilized in parallel to increase TMA force output as evident from the above equation. Thus, with the above information, a TMA can be designed given the force and displacement requirements.

Some of the TMA characteristics in the current design are provided in Table 7.3.

Table 7.3. TMA Characteristics

Property	Value	Unit
Number of parallel beams	14	#
Operating temperature	690	°C
Applied Voltage	2.53	V
Beam Half Length	7350	um
Width	350	um
Thickness	473	um
Force	1131	mN
stroke	316	um

The beam thickness is specifically chosen to be higher than its width in order to prevent out of plane buckling. This is done by making beams more stiff in the out of plane direction. A depiction of the resulting TMA is presented in Figure 7.12.

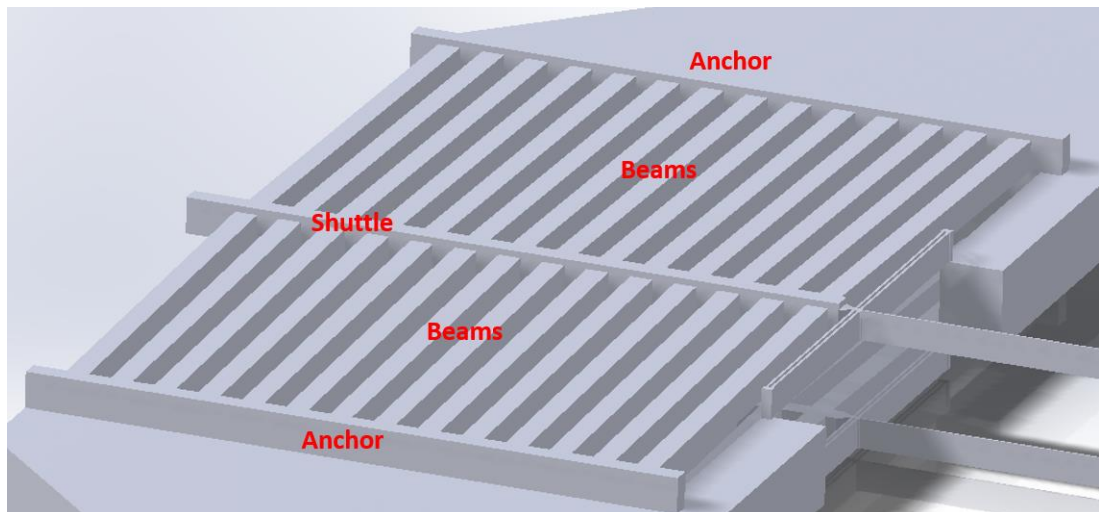


Figure 7.12. TMA Design Detail from MEMS VBA

7.3.5. Spring and Shaft Sizing

Spring element is sized for compliance. Assuming the operating frequency of the device as f , the equivalent spring coefficient should become

$$k_{eq} = \frac{4}{3} \frac{(2\pi f)^2}{d_{rod}^2} J_{rod} \quad (7.39)$$

The spring coefficient for the spring element can be calculated as

$$k_{spr} = \frac{k_{eq} k_{tma}}{(k_{tma} - k_{eq})} \quad (7.40)$$

Where k_{TMA} can easily be deduced from (7.38):

$$k_{TMA} = N_{beam} \frac{EW^3 t}{4L^3} \quad (7.41)$$

The spring beam coefficient presented in (7.40) is related to the shape of the spring beams via the following identity:

$$k_{spr} = 2N_{spr} \frac{EW_{spr}^3 t_{spr}}{L_{spr}^3} \quad (7.42)$$

Where N_{spr} is the number of parallel beams forming the spring element whereas W_{spr} , t_{spr} and L_{spr} are the width, thickness and length of each flexible beam, respectively. The mechanical implementation is exhibited in Figure 7.13. Note that two parallel cantilevered beam type springs were utilized to realize a spring requiring the previously described spring coefficient. In comparison with the equations (7.41) and (7.42) together with Figure 7.13, it is evident that TMA, spring and shaft have the same thickness. This is done in order to ensure that they can be produced in a single MEMS process from the same layer of silicon.

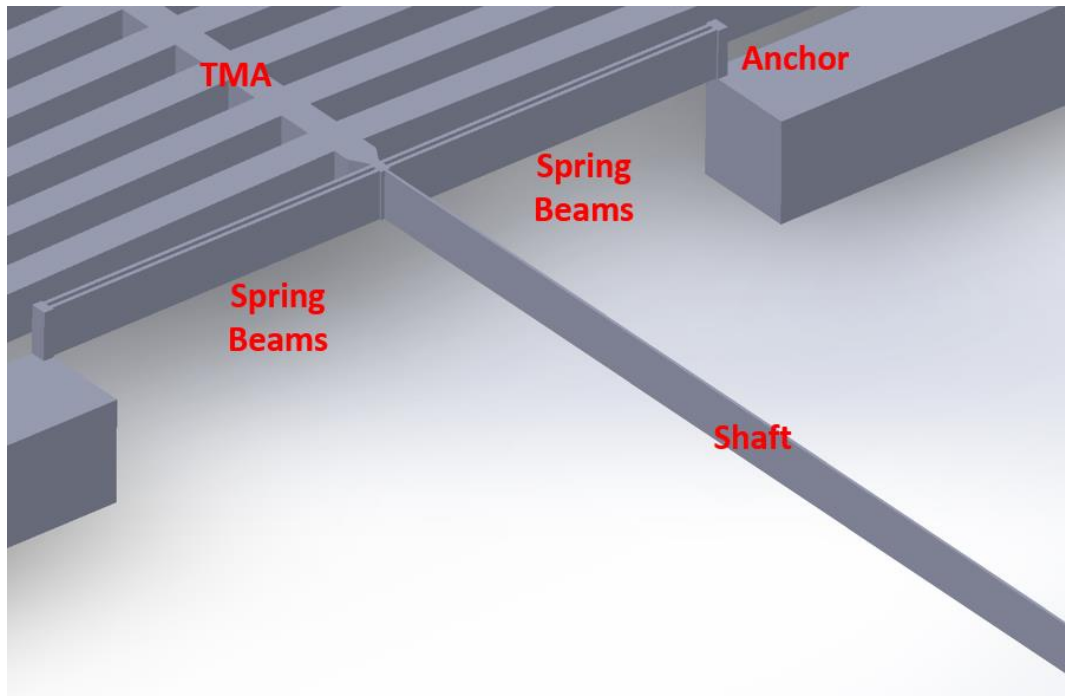


Figure 7.13. Spring Element and Shaft Implemented by Cantilevered Beams

The shaft element was designed to be more “soft” in comparison to TMA and spring.

Note that the TMA direction is “outwards”; it pulls the rod-like structure “away” from the center of the VBA. Hence, shafts apply only a pulling force to the rotor; in a sense they can be considered as “ropes” pulling on the rod-type rotor. Thus the shaft can be considered a “softer” element than the spring. This is actually what is desired since a soft “rope” like device would be compliant with the deformations which rotor would undergo.

A softness ratio was defined for the shaft as follows:

$$\eta_{soft} = \frac{f}{f_{sh}} \quad (7.43)$$

Where f is the design operating frequency of the actuator and f_{sh} is the fundamental frequency of the shaft. Thus the spring coefficient of the shaft can be defined by:

$$k_{sh} = \frac{k_{eq}}{\eta_{soft}^2} \quad (7.44)$$

The shaft is designed such that it realizes the above stiffness coefficient:

$$k_{sh} = \frac{E}{4} \frac{w_{sh} t_{sh}^3}{L_{sh}^3} \quad (7.45)$$

As with the discussion regarding the spring, the shaft is also designed to have the same thickness “t” with the spring structure in order to be produced in the same process. The shaft is also required to resist the tensile loading due to the TMA operation in addition to being able to carry the rotor weight. The tensile stress being endured by the shaft is calculated via:

$$\sigma_{tensile} = \frac{F_{tma}}{w_{sh} t} + \left(L_{sh} \frac{gm_{rod}}{8} \right) \frac{t}{2} \left(\frac{12}{w_{sh} t^3} \right) \quad (7.46)$$

Here, the first term corresponds to the tensile stress due to TMA operation whereas the second term quantifies the tensile stress due to the bending moment generated by the rotor weight. Note that the rotor weight is supported by eight different shafts and it results in bending moment, resulting in additional tensile stress.

The yield strength of the monocrystalline silicon is dependent on the temperature. Hence, the shaft is designed such that the above calculated tensile stress is lower than 361 MPa for operation in 700 °C (or to be conservative, lower than 139 MPa to cover up to 800 °C) [79].

7.4. Results

The design was imported from the CAD program to the COMSOL software platform and further structural and thermal analysis were carried out. First, the natural frequencies of the design were identified. Mode shapes of the first three structural resonance frequencies are provided from Figure 7.14 to Figure 7.16. The first natural frequency occurs at 444 Hz, corresponding to the out of plane motion of rod-type VBA. The second modal shape is located at 689 Hz and corresponds to the rotor

oscillation. Lastly, the third natural frequency correspond to the “gimbal” oscillation and occurs at 792 Hz.

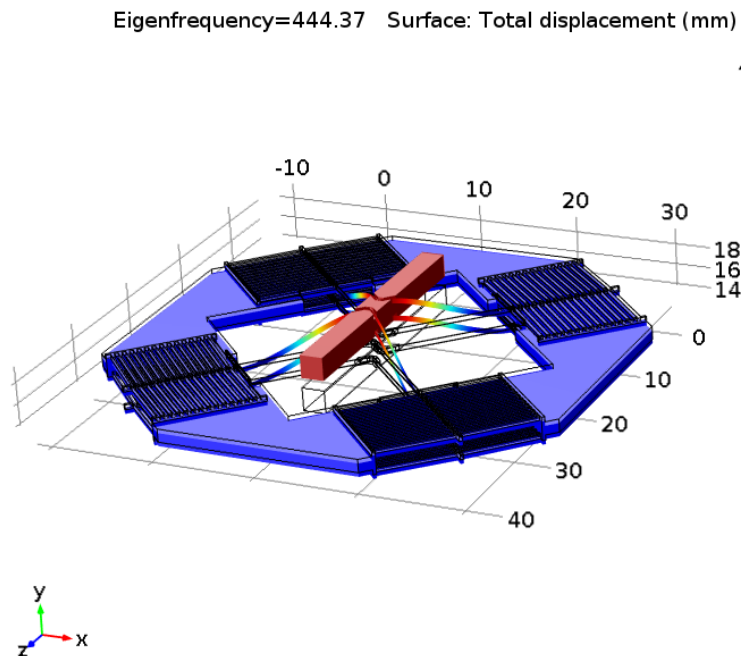


Figure 7.14. First Modal Shape for the MEMS Actuator (@447.37 Hz)

Eigenfrequency=688.71 Surface: Total displacement (mm)

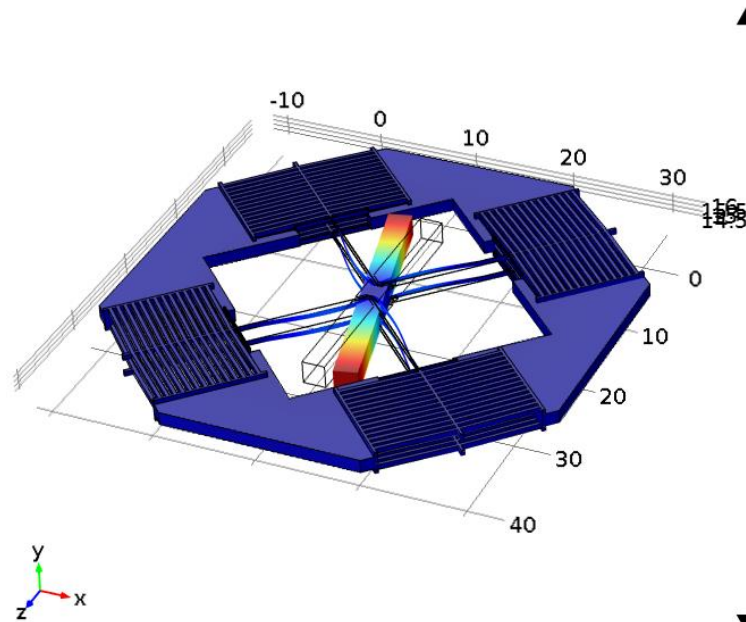


Figure 7.15. Second Modal Shape for the MEMS Actuator (@688.71 Hz)

Eigenfrequency=792.51 Surface: Total displacement (mm)

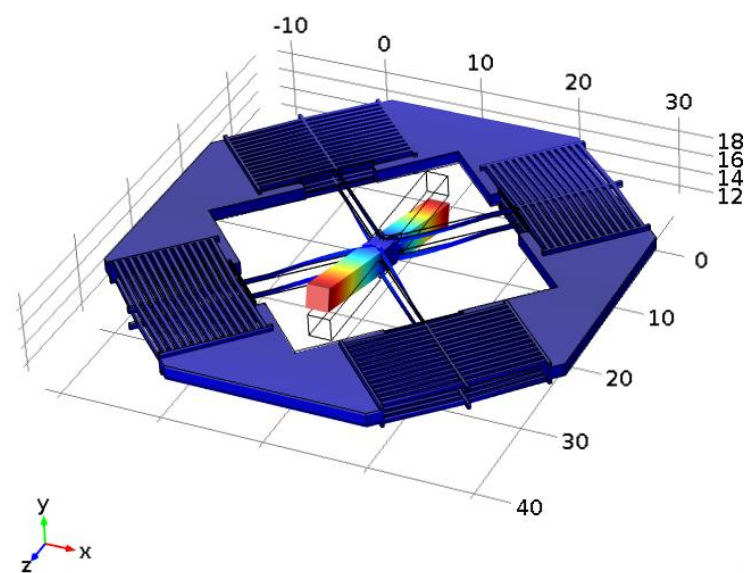


Figure 7.16. Third Modal Shape for the MEMS Actuator (@792.51 Hz)

It is foreseen that the device will operate at frequencies lower than the given frequencies (*i.e.* at 55 Hz) for the current use case. After these analyzes, thermal limiting conditions were applied to the thermal actuator surfaces by using COMSOL thermal stress module and deformations resulting from the operation of thermo-mechanical actuators in the x- and y- axes (*i.e.* gimbal and rotor axes) were obtained. The resulting temperature distributions due to actuation scheme presented from equations (7.20) to (7.22) are exhibited in Figure 7.17 and Figure 7.19. Resulting deformations are shown in Figure 7.18 and Figure 7.20 with 20-fold magnification of the actual deformation for better observability.

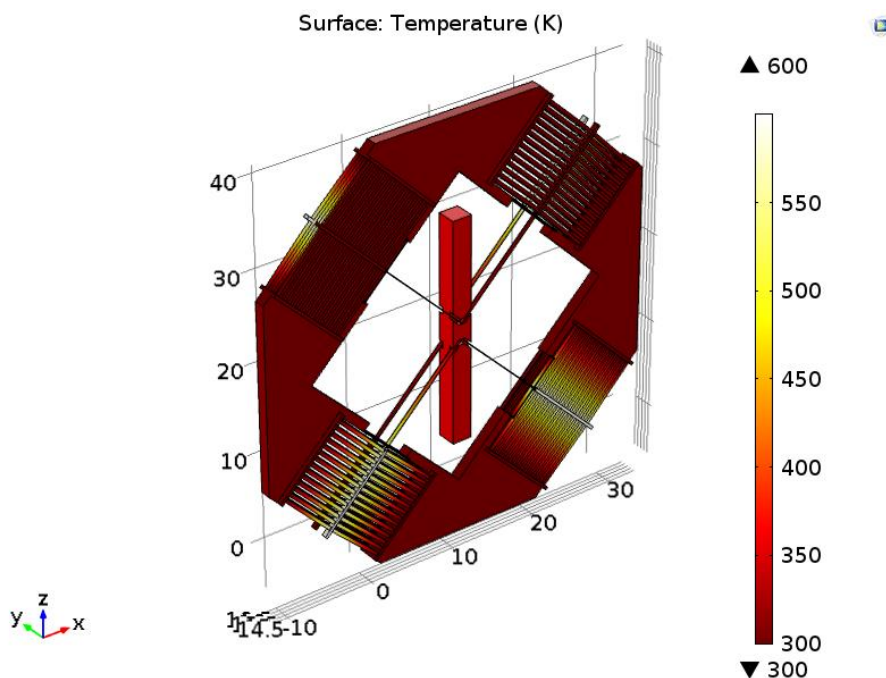


Figure 7.17. Temperature Distribution of Thermal Actuators to Enable x- Axis Rotation

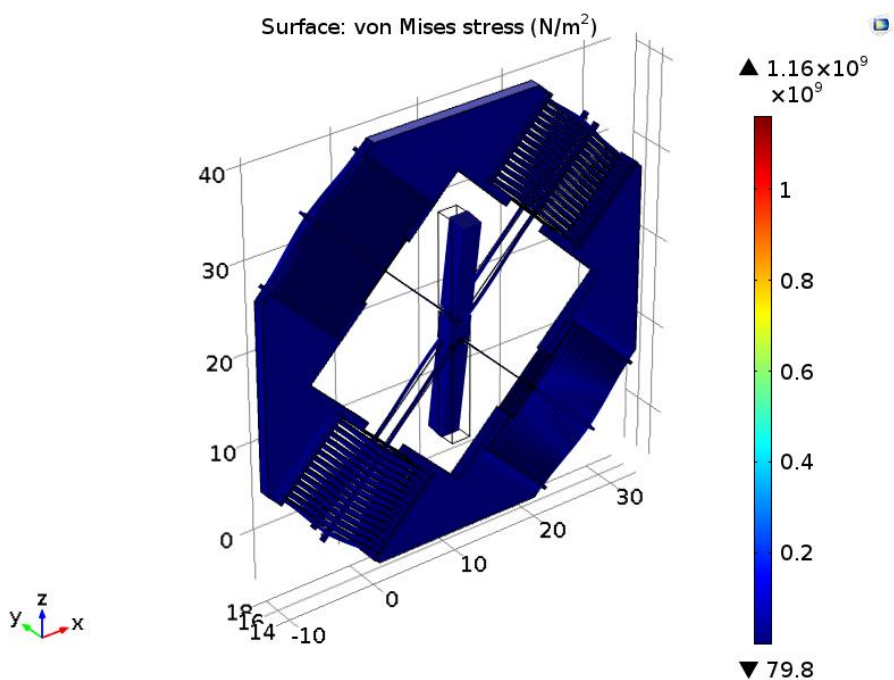


Figure 7.18. Resulting Deformation Leading to x- Axis Rotation

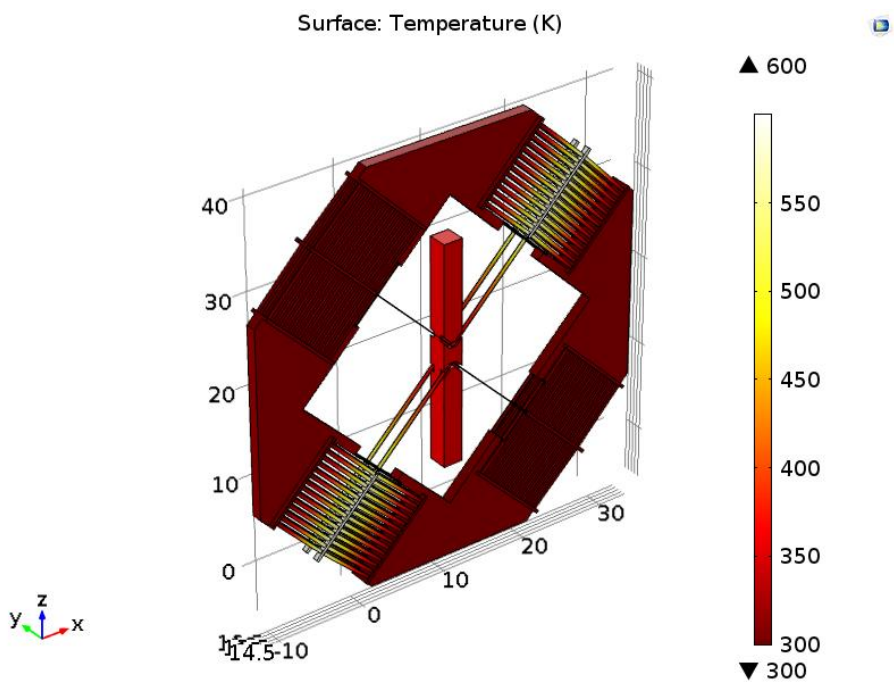


Figure 7.19. Temperature Distribution of Thermal Actuators to Enable y- Axis Rotation

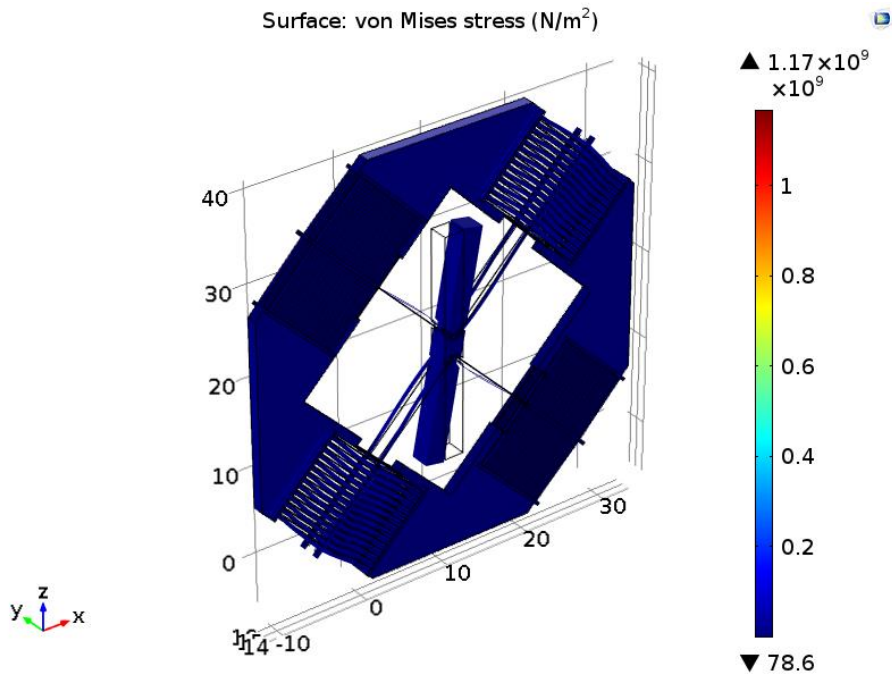


Figure 7.20. Resulting Deformation Leading to y- Axis Rotation

The rotation angle around the x- axis given in Figure 7.18 is 0.40° , while the rotation around the y- axis is 0.53° in Figure 7.20. As it can be observed from these results, it is feasible to actuate a rod-type MEMS proof mass in similar manner with the prototype actuator introduced in Ref. [30]. The properties of the resulting actuator are summarized in Table 7.4.

Table 7.4. MEMS VBA Properties

Property	Value	Unit
Mass	5.4	gr
Volume	$34 \times 34 \times 2$	mm^3
Angular Momentum	0.0103	μNms
Max Operating Temperature	686	$^\circ\text{C}$
Operating Voltage	2.53	V

However, even the present design with its current capabilities is capable of rotating miniature spacecraft. Assuming a chip satellite (such as the one exhibited in Figure 7.21) having a footprint of 5 cm by 5 cm with an inertia of 5.3×10^{-6} kg-m²; it is estimated that an array consisting of two of MEMS VBAs would be capable of rotating it with 0.2 °/s angular velocity. Note that, in satellite dynamics, an angular velocity of 3.4 °/s is considered as exceptionally agile [81]; hence 0.2 °/s would be considered an adequate performance.

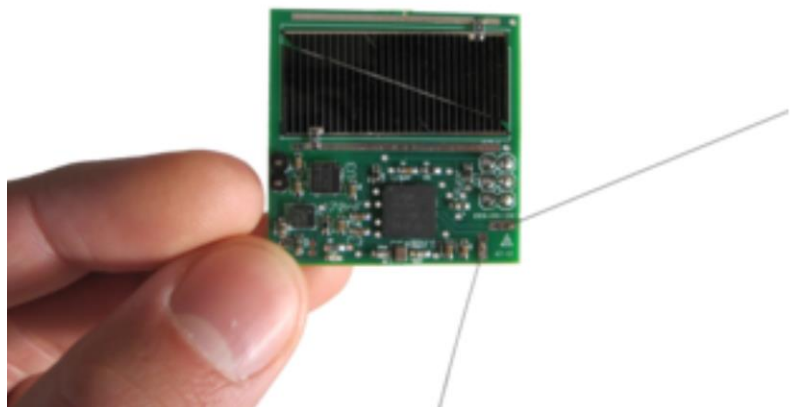


Figure 7.21. A Representative Chip-Sized Satellite [80]

Recall that, this is not a formal design for production but rather a design exploration. Through simulations it was shown that the rod-type VBA whose experimental prototype was built in previous studies [30], can be miniaturized and can conduct rotational oscillatory vibrations as defined in Eq. (2.1) and as exhibited in Figure 7.18 and Figure 7.20. The design methodology for various components has been identified in sections 7.3.4 and 7.3.5 and further iterations of the design would likely produce more efficient MEMS based rod-type VBAs.

CHAPTER 8

CONCLUSION

8.1. Summary

State of the art regarding satellite attitude actuators were investigated. It was observed that bearing mechanisms were the root cause of many momentum exchange device malfunctions.

History of vibration based actuation was also surveyed. Later, the mathematical relationship between the VBA design parameters and the resulting change in the satellite attitude due to the VBA operation was formulated. Furthermore, the effect of satellite attitude motion and VBA actuation coupling was investigated. It was found that VBAs with spherical rotors were least effected from such coupling.

A sphere-type prototype VBA was designed and manufactured. This effort included mechanical, electrical design as well as algorithm development. A simulation campaign in MSC ADAMS environment was carried out to quantify the expected outcome of this device's operation, which lead to rotational motion of the simulated air bearing. However, effect of the gimbal axis linear spring implementation was also observed upon close inspection of the resulting angular motion.

To characterize the prototype VBA, various methods were utilized. First, the torque output of the VBA was measured via the load cell. A tuning campaign was carried out to identify adequate stepper motor excitation inputs. Later, further experimentation with the frictionless air bearing were carried out. First, tethered experimentation was carried out. Due to the limiting effect of tethers on the air bearing motion, the sought output was observable only after analyzing the frequency content of the resulting encoder data. Later, a completely wireless experimental setup was formed. The VBA was able to rotate this experimental setup, proving the VBA attitude actuation concept.

Later, miniaturization trends in the satellite industry was surveyed. Models for dimensional analysis were built both for reaction wheel and the rod-type actuator. The RW model was validated with existing RW data from the market. Additionally, figures of merit for actuator performance quantification were introduced which are the specific angular momentum (angular momentum per unit mass of actuator) and volumetric angular momentum (angular momentum per volume of actuator).

Prospective dimensions for a MEMS based VBA was obtained from this dimensional analysis study. Consequently, a MEMS based rod-type VBA was designed. Its functioning was exhibited through simulations. Rod-type VBA was chosen for its suitability for production from a planar structure. Also, TMAs were utilized for the actuation of rod-type VBA rotor. However, due to their single directional operation, a new actuators scheme had to be introduced. All in all, feasibility of a MEMS based VBA was proven.

8.2. Discussion

In the course of the literature survey it was observed that the complex mechanisms such as the CMGs were susceptible to failures. Even extensive testing on laboratory conditions may not reveal susceptibility to malfunctions as observed in Skylab and ISS CMG failures. This lead to the motivation for VBA development.

The literature survey for VBA provided many theoretical undertakings but minimal experimental investigation. Most extensive experimental study was undertaken by Bernstein in 2003 [13], but that study involved VBAs as traversing point masses; not as rotational oscillatory motion.

As evident from the comparison of equations (2.68) and (2.69), the sphere-type VBA is least susceptible to such coupling effect in comparison with the rod-type VBA. However, sphere-type VBAs suffer from sinusoidal output whereas rod-type VBAs have constant output. Furthermore, the VBA prototype was unable to attain an ideal case of spherical-rotor VBA. This is due to the inability to implement torsional spring. Instead, linear springs utilizing moment arms were utilized. These later turned out to

be problematic since the output of gimbal linear springs had effected the motion in z-axis. Simulations exhibited excessive vibration due to this implementation.

In the un-tethered experiment, VBA was able to rotate the air bearing and the experimental tray. Yet, this was not a continuous and indefinite rotation as predicted by the simulation. It was observed during the free rotation of the air bearing (*i.e.* when the prototype was unactuated) that the experimental setup had a particular equilibrium point even though extensive balancing efforts. This is probably due to the imbalance of the experimental tray (*i.e.* COG of experimental tray is not coincident with the air bearing rotation axis). This prevented continuous rotation, but enabled rotation up to a point until the restoring torque exceeded the prototype VBA's maneuver capacity.

Lastly, market survey revealed the smallest COTS RW to have a 2 centimeter diameter. Custom solutions have to be sought for sizes smaller than this. Yet, this dimension class is even large for the previously mentioned pocketQube standard.

8.3. Conclusion

The mathematical formulation exhibited the possibility of VBAs that depend on oscillatory rotational motion.

It was found that angular momentum capacity of these devices mainly depend on the rotor inertia, oscillatory angles, input phase differences and frequency. Choice of rotor geometry enables either sinusoidal output with decoupling with host satellite's rotational rates (sphere-type VBA) or constant output with additional coupling with the host satellite's rotational rates (rod-type VBA).

It was shown that a working sphere-type VBA can be built from COTS equipment and its functioning can be proved via experimentation with frictionless air bearing.

Furthermore, it was identified that the VBAs are more adequate for miniaturization in comparison with the traditional momentum exchange devices. Their performance is dependent to the operating frequency, which can increase with decreasing size.

Furthermore, the volumetric and specific angular momentum of VBAs are independent of size (at least theoretically). This is in stark comparison with the traditional momentum exchange devices, which has poorer performance when scaled down.

Survey revealed that standardization and miniaturization lead to the distributed space missions utilizing many small satellites. This is an ideal ecosystem for smaller momentum exchange devices. Smaller satellite form factors such as pocketQube is being proposed and may be adopted in the future as it had been the case with the Cubesats. Below dimensions smaller than 10 millimeters, it is highly likely that rod-type VBAs would be more efficient than the traditional reaction wheels.

As mentioned earlier, the design study yielded that the rod-type MEMS based VBA to be feasible and can be utilized effectively in a chip satellite setting.

All in all, a novel actuator depending on vibration based actuation method was introduced and its concept is proven through experimentation. This method of actuation proved to be promising in a setting where equipment miniaturization is highly sought after.

8.4. Future Work

Several avenues for future research are identified. These can be summarized as:

- Multi-body dynamics based formulation would be needed to relate the internal torques such as stepper motor torque with the VBA and hence satellite attitude output. Methods for verifying such multibody dynamics models should also be investigated.
- Utilization of rod-type VBA arrays to mitigate undesired vibration and to have constant VBA output can be investigated. For instance, the possibility of eliminating coupling effects with the spacecraft motion through utilization of more than one rod-type VBAs for excess vibration cancelling can be researched.

- A new iteration of sphere-type VBA should be introduced without moment arm and linear spring implementation. Actually, it should not include any elements such as shafts etc.; instead it shall have strictly flexible elements, enabling oscillatory rotation.
- Active elements (*i.e.* coils within the stepper motors) in the VBA should have larger volume fraction. The volume encompassed by the active elements in the current prototype is much smaller than the whole rotor; corresponding to inefficient utilization of volume and underpowered prototype. To investigate the full potential of sphere-type VBA, a spherical rotor with higher active element fraction should be designed. A VBA with higher performance would be better suited for VBA characterization and research.
- An array of sphere-type VBAs may also be operated in conjunction to investigate canceling out the parasitic vibrations in non-output axes (Figure 8.1) as well as smoothing out the sinusoidal angular momentum output (Figure 8.2). Theoretically, these two approaches can be combined in a four element VBA array that can produce constant torque in a single axis (Figure 8.3).

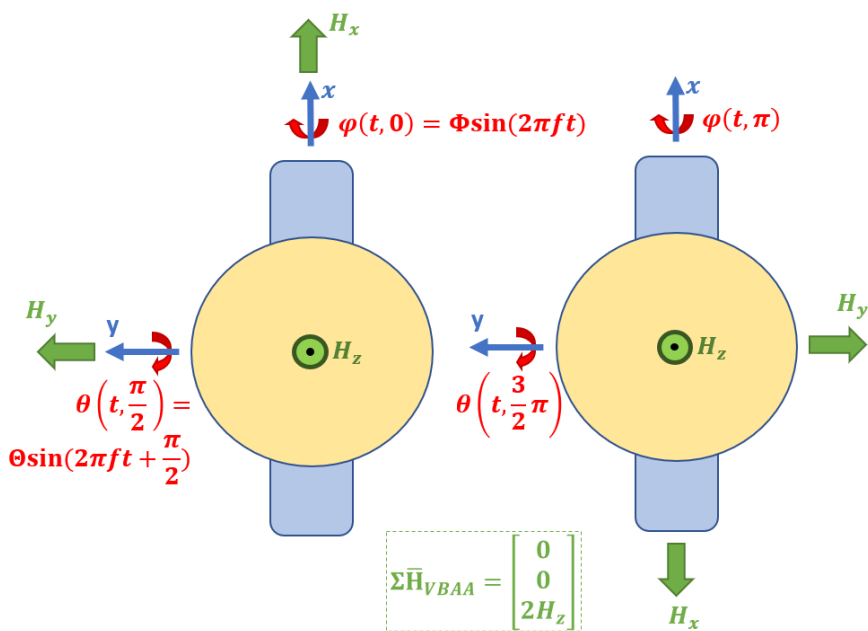


Figure 8.1. Driving Two Spherical Rotor VBAs (Viewed from Top) with $\pi/2$ Total Phase Difference to Cancel out Parasitic Angular Momentums in Non-output Axes

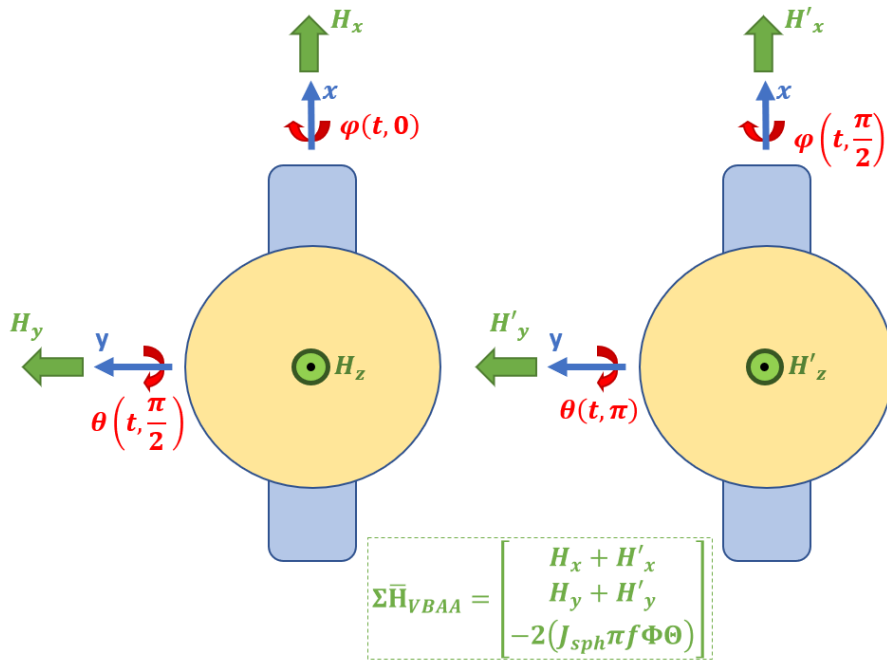


Figure 8.2. Driving Two Spherical Rotor VBAs with π Total Phase Difference to Smooth Output Angular Momentum

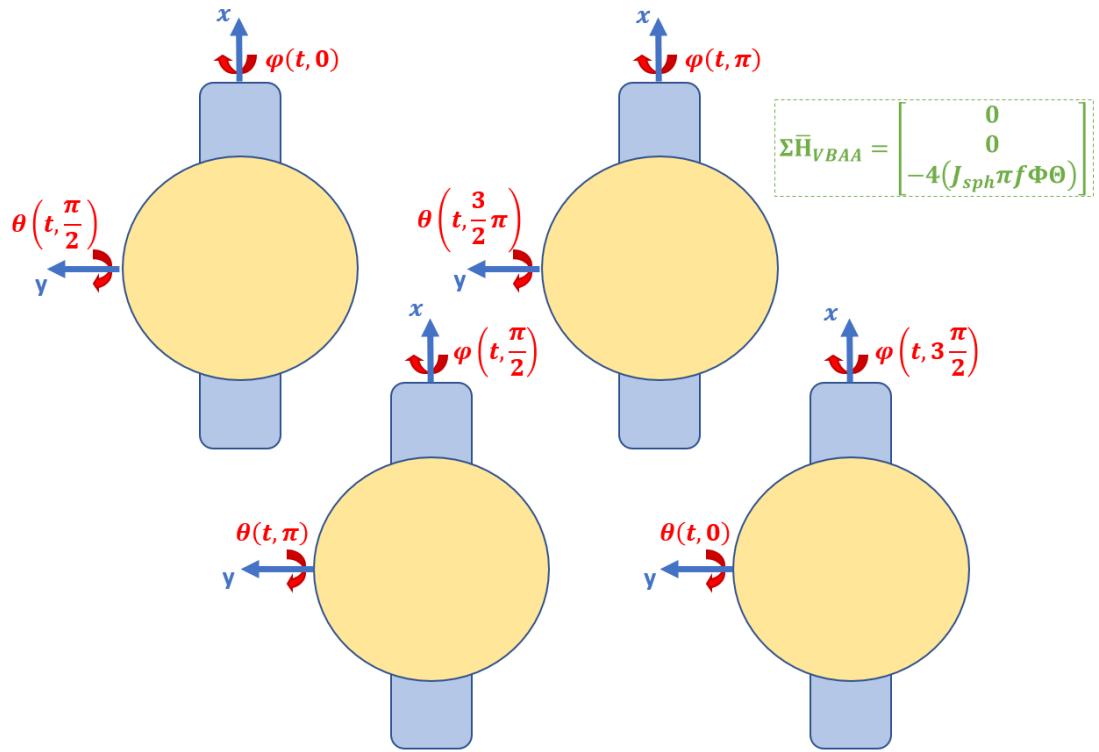


Figure 8.3. A Hypothetical Four Element VBA Array with Constant and Single Axis Angular Momentum Output

- Experimental tray may be redesigned with further provisions for more effective balancing.
- MEMS based rod-type VBA can be made more efficient by contouring TMA geometry for improved force, power and stroke efficiency. Furthermore, current design does not involve any sensing of rod motion. Hence sensing elements have to be incorporated into the VBA design, such as electrostatic comb sensors for TMA position sensing.

REFERENCES

- [1] Sidi, Marcel J.: *Spacecraft Dynamics and Control: A Practical Engineering Approach*, Cambridge University Press, 1997
- [2] Rossini, L., Chetelat, O., Onillon, E., and Perriard, Y.: Force and Torque Analytical Models of a Reaction Sphere Actuator Based on Spherical Harmonic Rotation and Decomposition, *IEEE/ASME Transactions on Mechatronics*, Vol. 18, No. 3
- [3] Seddon, J., and Pechev, A.: 3-D Wheel: A Single Actuator Providing Three-Axis Control of Satellites, *Journal of Spacecraft and Rockets* Vol. 49, No. 3, May–June 2012.
- [4] Inumoh, L., Horri, N.,and Pechev, A.: Tilted wheel for three-axis attitude control of a rigid satellite, *Advances in the Astronautical Sciences*. 145. 289-300.
- [5] Wayer, J.K., Castet, J.F., Saleh, J. H.: Spacecraft Attitude Control Subsystem: Reliability, Multi-State Analyses, and Comparative Failure Behavior in LEO and GEO, *Acta Astronautica*, 2013
- [6] Chang, H., Jiao, W., Fu, Q., Xie, J., Yuan, W.: Design and Simulation of a MEMS Control Moment Gyro-scope for the Sub-Kilogram Spacecraft, *Sensors*, 2010.
- [7] Sahnow David J. et al.: Operations with the new FUSE observatory: three-axis control with one reaction wheel, *Proc. of SPIE*, Vol. 6266, 626602, 2003
- [8] Hacker Johannes M., Ying J., and Lai Peter C., “Reaction Wheel Friction Telemetry Data Processing Methodology and On-Orbit Experience,” *Journal of Astronautical Sciences*, 2015, 62:254–269
- [9] Masashi U., et al, “Attitude Control Challenges and Solutions for Hayabusa Spacecraft,” *Proc. of SPIE*, Vol. 6266
- [10] Kane T.R. and Scher M.P.: A Dynamical Explanation of the Falling Cat Phenomenon, *Int. J. Solids Structures*, Vol. 5, pp. 663 to 670. Pergamon Press., UK, 1969
- [11] Kane T.R. and Scher M.P.: Human Self-Rotation by Means of Limb Movements, *Journal of Biomechanics*, Vol. 3. pp. 39-49., Pergamon Press., UK, 1970
- [12] Brockett R.W., On the Rectification of Vibratory Motion, Sensors and Actuators, Vol. 20 pp. 91-96., 1989
- [13] Bernstein D. S., McClamroch N. H. and Shen J.: Shape Change Actuation for Precision Attitude Control, *IEEE Control Systems Magazine*, pp. 44-56, October 2003
- [14] Kawamura T.: Understanding of Falling Cat Phenomenon and Realization by Robot, *Journal of Robotics and Mechatronics*, Vol. 26 No.6 pp. 685-690, 2014

- [15] Stevenson D., Schaub H.: Nonlinear Control Analysis of a Double-Gimbal Variable-Speed Control Moment Gyroscope, AIAA Journal of Guidance, Control, and Dynamics, Vol. 35, No 3, 2012.
- [16] Coon, Thomas R. and Irby, John E.: Skylab Attitude Control System, IBM Journal of Research and Development, Vol. 20, No 1, 1976.
- [17] Akbulut, B., Tekinalp, O., Arberkli, F., and Azgin, K.: Oscillating Control Moment Gyroscope Experimental Results, AIAA Scitech 2019 Forum, San Diego, CA, USA, AIAA 2019-0937, 2019.
- [18] Carlo, M., and Izzo, D.: Satellite Pointing System based on EAP actuators, Proceedings of TAROS, 2005.
- [19] Xiao-wei, S., Xue-qin, C., Yun-hai, G., and Shi-jie, Z.: Small satellite attitude control based on mechanically-pumped fluid loops, 6th IEEE Conference on Industrial Electronics and Applications, Beijing, 2011.
- [20] Tayebi, J., and Soleymani, A.: A comparative study of CMG and FMC actuators for Nano satellite attitude control system-pyramidal configuration, 7th International Conference on Recent Advances in Space Technologies (RAST), Istanbul, 2015.
- [21] Reiter, J., Böhringer, K., Campbell, M.: MEMS Control Moment Gyroscope Design and Wafer-Based Spacecraft Chassis Study, Micromachined Devices and Components V, Santa Clara CA USA, 1999.
- [22] Kim Y.V. and Deraspe G.: Resolving Radarsat-1 Momentum Wheels Failure Problem, 54th International Astronautical Congress, Bremen, Germany, 2003
- [23] Portree D. S. F.: Mir Hardware Heritage, NASA-RP-1357
- [24] Bendix Corporation: ATM CMG Bearing Failure Analysis Final Report, NASA Technical Memorandum, TM X-64583, 1975.
- [25] Nobari, N. A.: Attitude Dynamics and Control of Satellites with Fluid Ring Actuators, Ph.D. Dissertation, McGill Univ., 2013.
- [26] Akbulut, B.: Attitude Control of Multiple Rigid Body Spacecraft with Flexible Hinge Joints, MS Thesis, METU, Ankara, Turkey, 2009.
- [27] Viswanathan, S. P., Sanyal, A. K., Leve, F., and McClamroch, N. H.: Dynamics and Control of Spacecraft with a Generalized Model of Variable Speed Control Moment Gyroscopes, Journal of Dynamic Systems, Measurement, and Control Vol. 137, No. 7, 2015.
- [28] Roithmayr, C. M., Karlgaard, C. D., Kumar, R. R., Seywald, H. and Bose, D. M.: Dynamics and Control of Attitude, Power, and Momentum for a Spacecraft Using Flywheels and Control Moment Gyroscopes, Technical Publication, NASA Langley Research Center, NASA/TP-2003-212178, 2003
- [29] Skelton II, C. E.: Mixed Control Moment Gyro and Momentum Wheel Attitude Control Strategies, MS Thesis, Virginia Polytechnic Institute and State University, Blacksburg, VA, USA, 2003.

- [30] Arberkli, F.: A Control Moment Gyroscope Based on Rotational Vibrations, Dynamic Model and Experimentation, MS Thesis, METU, Ankara, Turkey, 2019.
- [31] ESA: ECSS E-HB-60A Control Engineering Handbook, ECSS Standard, European Cooperation on Space Standardization, 2010
- [32] Lissauer, J. and de Pater, I.: Fundamental planetary science: physics, chemistry and habitability, Cambridge University Press, 2013
- [33] Inumoh, L., Horri, N., Forshaw J. L. and Pechev, A.: Bounded gain-gain scheduled LQR satellite control using a tilted wheel, IEEE Transactions on Aerospace and Electronic Systems, Vol. 50, No. 3, 1726-1738.
- [34] Akbulut, B., Arberkli, F., Azgin, K. and Tekinalp, O.: A Simplified Model for Vibrating Mass Control Moment Gyroscope, 27th AAS/AIAA Space Flight Mechanics Meeting, San Antonio, TX, USA, 2017.
- [35] Votel, R., and Sinclair, D.: A comparative study of CMG and FMC actuators for Nano satellite attitude control system-pyramidal configuration, 26th Annual AIAA/USU Conference on Small Satellites, Utah, USA, 2012.
- [36] Halt, T., and Wieger, A.: Smallsats by the Numbers – 2019, Bryce Space and Technology, Alexandria, VA, USA, 2019
- [37] Merhparvar, A., and Pignatelli, D.: CubeSat Design Specification, Rev. 13, California Polytechnic State University, Ca, USA, 2014
- [38] Radu, S., *et al*: The PocketQube Standard, Issue 1, 2018
- [39] Collins Aerospace: RSI 45 Momentum and Reaction Wheels, www.rockwellcollins.com, accessed 16/5/2019
- [40] Astro-und Feinwerktechnik Adlershof GmbH: RW1 Datasheet, www.astrofein.com, accessed 17/5/2019
- [41] Astro-und Feinwerktechnik Adlershof GmbH: RW35 Datasheet, www.astrofein.com, accessed 17/5/2019
- [42] Astro-und Feinwerktechnik Adlershof GmbH: RW90 Datasheet, www.astrofein.com, accessed 17/5/2019
- [43] Astro-und Feinwerktechnik Adlershof GmbH: RW150 Datasheet, www.astrofein.com, accessed 17/5/2019
- [44] Astro-und Feinwerktechnik Adlershof GmbH: RW250 Datasheet, www.astrofein.com, accessed 17/5/2019
- [45] Sinclair Interplanetary: 3 mNms Picosatellite Wheel Datasheet, www.sinclairinterplanetary.com, accessed 17/5/2019
- [46] Sinclair Interplanetary: 10 mNms Picosatellite Wheel Datasheet, www.sinclairinterplanetary.com, accessed 17/5/2019
- [47] Sinclair Interplanetary: 30 mNms Nanosatellite Wheel Datasheet, www.sinclairinterplanetary.com, accessed 17/5/2019
- [48] Sinclair Interplanetary: 60 mNms Microsatellite Wheel Datasheet, www.sinclairinterplanetary.com, accessed 17/5/2019
- [49] Sinclair Interplanetary: 1 Nms Microsatellite Wheel Datasheet, www.sinclairinterplanetary.com, accessed 17/5/2019

- [50] Collins Aerospace: RSI 01-5/28 Reaction Wheel Datasheet, www.rockwellcollins.com, accessed 18/5/2019
- [51] Collins Aerospace: RSI 01-5/15 Reaction Wheel Datasheet, www.rockwellcollins.com, accessed 18/5/2019
- [52] Vectronic Aerospace GmbH: VRW-1 Datasheet, www.vectronic-aerospace.com, accessed 17/5/2019
- [53] Vectronic Aerospace GmbH: VRW-05 Datasheet, www.vectronic-aerospace.com, accessed 17/5/2019
- [54] Vectronic Aerospace GmbH: VRW-02 Datasheet, www.vectronic-aerospace.com, accessed 17/5/2019
- [55] Blue Canyon Technologies: RWP015 Datasheet, www.bluecanyontech.com, accessed 11/5/2019
- [56] Blue Canyon Technologies: RWP050 Datasheet, www.bluecanyontech.com, accessed 11/5/2019
- [57] Blue Canyon Technologies: RWP100 Datasheet, www.bluecanyontech.com, accessed 11/5/2019
- [58] Blue Canyon Technologies: RWP500 Datasheet, www.bluecanyontech.com, accessed 11/5/2019
- [59] Blue Canyon Technologies: RWP1 Datasheet, www.bluecanyontech.com, accessed 11/5/2019
- [60] Blue Canyon Technologies: RWP4 Datasheet, www.bluecanyontech.com, accessed 11/5/2019
- [61] Blue Canyon Technologies: RWP8 Datasheet, www.bluecanyontech.com, accessed 11/5/2019
- [62] CubeSpace: CubeWheel S Datasheet, www.cubespace.co.za, accessed 10/5/2019
- [63] CubeSpace: CubeWheel M Datasheet, www.cubespace.co.za, accessed 10/5/2019
- [64] CubeSpace: CubeWheel L Datasheet, www.cubespace.co.za, accessed 10/5/2019
- [65] Microsat Systems Canada Inc.: MicroWheel 200 Brochure, www.mscinc.ca, accessed 10/5/2019
- [66] Microsat Systems Canada Inc.: MicroWheel 1000 Brochure, www.mscinc.ca, accessed 10/5/2019
- [67] Microsat Systems Canada Inc.: MicroWheel 4000 Brochure, www.mscinc.ca, accessed 10/5/2019
- [68] Surrey Satellite Technology Ltd.: SSTL 10SP-O Datasheet, www.sstl.co.uk, accessed 9/5/2019
- [69] Surrey Satellite Technology Ltd.: SSTL 10SP-M Datasheet, www.sstl.co.uk, accessed 9/5/2019
- [70] Surrey Satellite Technology Ltd.: SSTL 200SP Datasheet, www.sstl.co.uk, accessed 9/5/2019
- [71] NewSpace Systems Ltd.: NRWA-T005 Reaction Wheel Datasheet, www.newspacesystems.comhttp://www.sstl.co.uk/, accessed 9/5/2019

- [72] NewSpace Systems Ltd.: NRWA-T065 Reaction Wheel Datasheet, www.newspacesystems.comhttp://www.sstl.co.uk/, accessed 9/5/2019
- [73] NewSpace Systems Ltd.: NRWA-T10 Reaction Wheel Datasheet, www.newspacesystems.comhttp://www.sstl.co.uk/, accessed 9/5/2019
- [74] Livermore, C.: Course Materials for 6.777J/2.372J Design and Fabrication for Microelectromechanical Devices, Spring 2007, MIT Opencourseware, MIT, accessed on 15/02/2019
- [75] Chen S., Choi H., So P. T. C., Culpeper M.C.: “Thermomechanical Based three axis optical scanner for high speed Two photon Endomicroscopic Imaging”, Journal of Microelectromechanical Systems, Vol 23, IVO 3, June 2014
- [76] Chen, S. and Culpeper, M.C.: “Design of Contoured Microscale Thermomechanical Actuators”, Journal of Microelectromechanical Systems, Vol 15, No 5, October 2006
- [77] Baker M. S., Plass R. A., Headly T. J. and Walraven, J. A.: “Final report: Compliant Thermo-Mechanical MEMS Actuators”, Sandia National Laboratories, SAND2004-6635, 2004
- [78] Girbau D., Lazaro, A., Prudell L.; “RF MEMS switches based on the buckle beam thermal Actuator”, 33rd European Microwave Conference, Munich, 2003
- [79] Milman Y. V., Gridneva I.V., Golubenko A. A.: “Construction of Stress-Strain Curves for Brittle Materials by Indentation in a Wide Temperature Range”, Science of Sintering, Vol 39, January 2007
- [80] Manchester Z., Peck M., Filo A.: “KickSat: A Crowd-Funded Mission To Demonstrate The World’s Smallest Spacecraft”, 27th Annual AIAA/USU Conference on Small Satellites, Logan, UT, USA 2013
- [81] Gleyzes M. A., Perret L., Kubik P.: “Pleiades System Architecture and Main Performances”, XXII ISPRS Congress, Melbourne, Australia, 2012
- [82] Tedaldi D., Pretto A. and Menegetti E.: “A Robust and Easy to Implement Method for IMU Calibration without External Equipments”, 2014 IEEE International Conference on Robotics and Automation (ICRA), Hong Kong, 2014, pp. 3042-3049
- [83] InvenSense Inc., “MPU-6000 and MPU-6050 Register Map and Descriptions”, Rev. 4.2, RM-MPU-6000A-00, 08/19/2013
- [84] Koh S. K. and Anantharesh G. K.: “Motion-Planning for the Axis-control of Miniature Spacecraft using Microactuators”, Proceedings of DETC’02, Montreal, Canada, 2002
- [85] Tyrell N. S.: “Attitude Control via Structural Vibration”, MS Thesis, MIT, Boston, MA, USA, 2014
- [86] Trimmer W. S. N.: “Microrobots and Micromechanical Systems”, Sensors and Actuators, Vol 19, 267-287, 1989
- [87] Wautelet M.: “Scaling Laws in the macro-, micro-, and nanoworlds”, European Journal of Physics, Vol 22, 601-611, 2001

APPENDICES

A. Datasheet for the Components Utilized in Actuators

Ordering number : EN2623F

LA6500

Monolithic Linear IC
Power Operational Amplifier



ON Semiconductor®

<http://onsemi.com>

Overview

The LA6500 is a power operational amplifier.

Features

- High output current (I_O max = 1.0A)
- High gain
- With current limiter
- Capable of being operated from single supply

Specifications

Maximum Ratings at $T_a = 25^\circ\text{C}$

Parameter	Symbol	Conditions	Ratings	Unit
Maximum supply voltage	V_{CC}/V_{EE}		± 18	V
Differential input voltage	V_{ID}		30	V
Common-mode input voltage	V_{IN}		± 15	V
Output current	I_O max		1.0	A
Allowable power dissipation	P_d max1	With infinity large heat sink	20	W
	P_d max2	Independent IC	1.75	W
Operating temperature	T_{opr}		-20 to +75	$^\circ\text{C}$
Storage temperature	T_{stg}		-55 to +150	$^\circ\text{C}$

Stresses exceeding Maximum Ratings may damage the device. Maximum Ratings are stress ratings only. Functional operation above the Recommended Operating Conditions is not implied. Extended exposure to stresses above the Recommended Operating Conditions may affect device reliability.

Figure A.1. Power Operational Amplifier LA6500 Specifications

LA6500

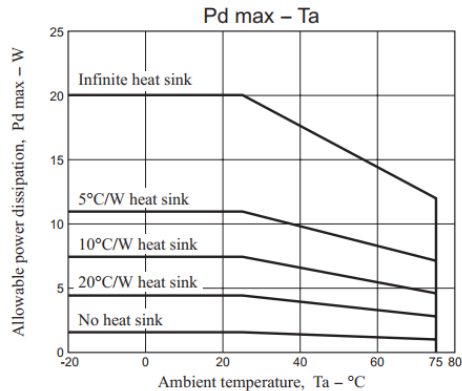
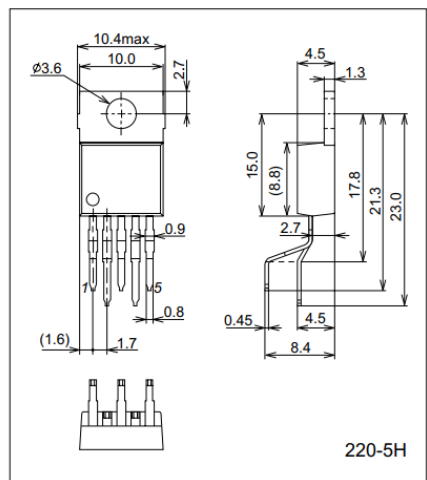
Electrical Characteristics at $T_a = 25^\circ\text{C}$, $V_{CC}/V_{EE} = \pm 15\text{V}$

Parameter	Symbol	Conditions	Ratings			Unit
			min	typ	max	
Quiescent current dissipation	I_{CC0}			6.0	12.0	mA
Input offset voltage	V_{IO}			2	6	mV
Input offset current	I_O			10	200	nA
Input bias current	I_B			100	700	nA
Common-mode input voltage range	V_{ICM}		-15		+13	V
Common-mode rejection	CMR			70	80	dB
Maximum output voltage	V_O	$R_L = 33\Omega$	± 12	± 13		V
Voltage gain	VG_O			100		dB
Slew rate	SR	$G_V = 0, R_L = 33\Omega, R = 2.2\Omega, L = 0.1\mu\text{F}$		0.15		$\text{V}/\mu\text{s}$
Equivalent input noise voltage	V_{NI}	$R_g = 1\text{k}\Omega$, DIN AUDIO		2		μV
Supply voltage rejection	SVR			30	150	$\mu\text{V/V}$
Limiting current	I_{SC}			1.0		A

Package Dimensions

unit : mm (typ)

3079C



Pin Assignment

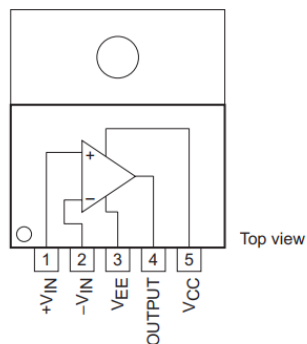


Figure A.2. Power Operational Amplifier LA6500 Specifications Continued

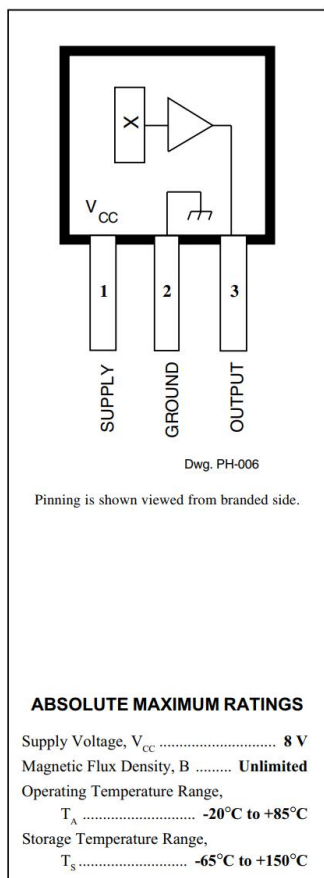
PARAMETER	CONDITIONS	MIN	TYP	MAX	UNITS	NOTES
GYROSCOPE SENSITIVITY						
Full-Scale Range	FS_SEL=0 FS_SEL=1 FS_SEL=2 FS_SEL=3		±250 ±500 ±1000 ±2000		%/s %/s %/s %/s	
Gyroscope ADC Word Length	16				bits	
Sensitivity Scale Factor	131 65.5 32.8 16.4				LSB/(%/s) LSB/(%/s) LSB/(%/s) LSB/(%/s)	
Sensitivity Scale Factor Tolerance	-3			+3	%	
Sensitivity Scale Factor Variation Over Temperature	25°C		±2		%	
Nonlinearity	Best fit straight line; 25°C		0.2		%	
Cross-Axis Sensitivity			±2		%	
GYROSCOPE ZERO-RATE OUTPUT (ZRO)						
Initial ZRO Tolerance	25°C		±20		%/s	
ZRO Variation Over Temperature	-40°C to +85°C		±20		%/s	
Power-Supply Sensitivity (1-10Hz)	Sine wave, 100mVpp; VDD=2.5V		0.2		%/s	
Power-Supply Sensitivity (10 - 250Hz)	Sine wave, 100mVpp; VDD=2.5V		0.2		%/s	
Power-Supply Sensitivity (250Hz - 100kHz)	Sine wave, 100mVpp; VDD=2.5V		4		%/s	
Linear Acceleration Sensitivity	Static		0.1		%/s/g	
SELF-TEST RESPONSE						
Relative	Change from factory trim	-14		14	%	1
GYROSCOPE NOISE PERFORMANCE						
Total RMS Noise	FS_SEL=0		0.05		%/s-rms	
Low-frequency RMS noise	DLPFCFG=2 (100Hz)		0.033		%/s-rms	
Rate Noise Spectral Density	Bandwidth 1Hz to 10Hz		0.005		%/s/ √ Hz	
At 10Hz						
GYROSCOPE MECHANICAL FREQUENCIES						
X-Axis		30	33	36	kHz	
Y-Axis		27	30	33	kHz	
Z-Axis		24	27	30	kHz	
LOW PASS FILTER RESPONSE	Programmable Range	5		256	Hz	
OUTPUT DATA RATE	Programmable	4		8,000	Hz	
GYROSCOPE START-UP TIME	DLPFCFG=0 to ±1% of Final			30	ms	
ZRO Settling (from power-on)						

Figure A.3. MPU6050 IMU Specifications for Gyroscope Functionality

PARAMETER	CONDITIONS	MIN	TYP	MAX	UNITS	NOTES
ACCELEROMETER SENSITIVITY						
Full-Scale Range	AFS_SEL=0 AFS_SEL=1 AFS_SEL=2 AFS_SEL=3		±2 ±4 ±8 ±16		g	
ADC Word Length	Output in two's complement format		16		bits	
Sensitivity Scale Factor	AFS_SEL=0 AFS_SEL=1 AFS_SEL=2 AFS_SEL=3		16,384 8,192 4,096 2,048		LSB/g LSB/g LSB/g LSB/g	
Initial Calibration Tolerance			±3		%	
Sensitivity Change vs. Temperature	AFS_SEL=0, -40°C to +85°C		±0.02		%/°C	
Nonlinearity	Best Fit Straight Line		0.5		%	
Cross-Axis Sensitivity			±2		%	
ZERO-G OUTPUT						
Initial Calibration Tolerance	X and Y axes Z axis		±50 ±80		mg mg	1
Zero-G Level Change vs. Temperature	X and Y axes, 0°C to +70°C Z axis, 0°C to +70°C		±35 ±60		mg	
SELF TEST RESPONSE						
Relative	Change from factory trim	-14		14	%	2
NOISE PERFORMANCE						
Power Spectral Density	@10Hz, AFS_SEL=0 & ODR=1kHz		400		µg/√Hz	
LOW PASS FILTER RESPONSE						
	Programmable Range	5		260	Hz	
OUTPUT DATA RATE						
	Programmable Range	4		1,000	Hz	
INTELLIGENCE FUNCTION INCREMENT				32		mg/LSB

Figure A.4. MPU6050 IMU Specifications for Accelerometer Functionality

RATIOMETRIC, LINEAR HALL-EFFECT SENSORS



The UGN3503LT, UGN3503U, and UGN3503UA Hall-effect sensors accurately track extremely small changes in magnetic flux density—changes generally too small to operate Hall-effect switches.

As motion detectors, gear tooth sensors, and proximity detectors, they are magnetically driven mirrors of mechanical events. As sensitive monitors of electromagnets, they can effectively measure a system's performance with negligible system loading while providing isolation from contaminated and electrically noisy environments.

Each Hall-effect integrated circuit includes a Hall sensing element, linear amplifier, and emitter-follower output stage. Problems associated with handling tiny analog signals are minimized by having the Hall cell and amplifier on a single chip.

Three package styles provide a magnetically optimized package for most applications. Package suffix 'LT' is a miniature SOT-89/TO-243AA transistor package for surface-mount applications; suffix 'U' is a miniature three-lead plastic SIP, while 'UA' is a three-lead ultra-mini-SIP. All devices are rated for continuous operation over the temperature range of -20°C to +85°C.

FEATURES

- Extremely Sensitive
- Flat Response to 23 kHz
- Low-Noise Output
- 4.5 V to 6 V Operation
- Magnetically Optimized Package

ABSOLUTE MAXIMUM RATINGS

Supply Voltage, V_{CC}	8 V
Magnetic Flux Density, B	Unlimited
Operating Temperature Range,		
T_A	-20°C to +85°C
Storage Temperature Range,		
T_S	-65°C to +150°C

Always order by complete part number, e.g., **UGN3503UA**.

Figure A.5. UGN3503 Hall Effect Sensor Specifications

ELECTRICAL CHARACTERISTICS at $T_A = +25^\circ\text{C}$, $V_{CC} = 5 \text{ V}$

Characteristic	Symbol	Test Conditions	Limits			
			Min.	Typ.	Max.	Units
Operating Voltage	V_{CC}		4.5	—	6.0	V
Supply Current	I_{CC}		—	9.0	13	mA
Quiescent Output Voltage	V_{OUT}	$B = 0 \text{ G}$	2.25	2.50	2.75	V
Sensitivity	ΔV_{OUT}	$B = 0 \text{ G} \text{ to } \pm 900 \text{ G}$	0.75	1.30	1.75	mV/G
Bandwidth (-3 dB)	BW		—	23	—	kHz
Broadband Output Noise	V_{out}	$BW = 10 \text{ Hz to } 10 \text{ kHz}$	—	90	—	μV
Output Resistance	R_{OUT}		—	50	220	Ω

Figure A.6. UGN3503 Hall Effect Sensor Specifications Continued

B. Datasheet for the Equipment Utilized in Experimental Setup

NI PCI-4461

24-Bit, 204.8 kS/s, 2 Inputs/2 Outputs

- 24-bit resolution ADCs and DACs with 118 dB dynamic range
- 6 gain settings for input ranges from ± 316 mV to 42.4 V
- 2 simultaneously sampled analog inputs at up to 204.8 kS/s
- 2 simultaneously updated analog outputs at up to 204.8 kS/s
- Software-configurable AC/DC coupling and IPEM conditioning
- Variable antialiasing and anti-imaging filters and TEDS support



Overview

The National Instruments PCI-4461 high-accuracy data acquisition module is specifically designed for sound and vibration applications. With 24-bit sigma-delta analog-to-digital converters (ADCs) and 24-bit analog output, it is ideal for stimulus-response applications including audio and structural tests. The NI PCI-4461 features 118 dB dynamic range and six gain settings for precision measurements with microphones, accelerometers, and other transducers that have very high dynamic ranges. Some common applications with the PCI-4461 include audio amplifier and production equipment test, shaker table control, vibration analysis, and machine condition monitoring.

Best Value - Buy Both and Save

The PCI-4461 is also available as a bundle with the NI Sound and Vibration Measurement Suite, which includes the NI Sound and Vibration Assistant, at a discount from the list price. See the *Resources* tab for more information on the list of analysis capabilities in the Sound and Vibration Measurement Suite.

Multidevice Synchronization for High-Channel-Count Systems

You can synchronize the PCI-4461 with additional PCI-4461 boards to build systems with six simultaneous inputs and six simultaneous outputs (requires three PCI-4461 boards). In addition, you can synchronize other dynamic signal acquisition (DSA) boards, such as the four-input NI PCI-4462, with the PCI-4461 to create systems with 10 simultaneous inputs and two simultaneous outputs (requires one PCI-4461 board and two PCI-4462 boards).

Recommended Software

NI sound and vibration analysis software, including the NI Sound and Vibration Measurement Suite and the NI Sound and Vibration Toolkit, provides signal processing functionality for performing audio measurements, fractional-octave analysis, frequency analysis, transient analysis, and order tracking. NI analysis software features NI Sound and Vibration Assistant interactive software for quickly acquiring, analyzing, and logging acoustic, noise, and vibration data. With a configuration-based, flexible measurement library and open-analysis capability, Sound and Vibration Assistant is designed for quick data capture through a unique software-based measurement approach to create customized applications.

Figure B.7. NI PCI-4461 High Performance ADC/DAC Card Specifications

Analog Input	
Channels	2, 0
Single-Ended Channels	0
Differential Channels	2
Resolution	24 bits
Sample Rate	204.8 kS/s
Max Voltage	42.4 V
Maximum Voltage Range	-42.4 V , 42.4 V
Maximum Voltage Range Sensitivity	5.05 μ V
Minimum Voltage Range	-316 mV , 316 mV
Minimum Voltage Range Sensitivity	37.7 nV
Number of Ranges	6
Simultaneous Sampling	Yes
On-Board Memory	2047 samples
Dynamic Range	118 dB
Excitation Current	10 mA
Analog Output	
Channels	2
Resolution	24 bits
Max Voltage	10 V
Maximum Voltage Range	-10 V , 10 V
Maximum Voltage Range Sensitivity	1.19 μ V
Minimum Voltage Range	-100 mV , 100 mV
Minimum Voltage Range Sensitivity	11.9 nV
Update Rate	204.8 kS/s
Current Drive Single	16.67 mA

Figure B.8. NI PCI-4461 High Performance ADC/DAC Card Specifications Continued

MC3A-250 SPECIFICATIONS

The MC3A is a compact, six-axis transducer with threaded inserts on its top surface and through holes on its bottom surface that act as attachment points. The body of the load cell is manufactured from a high-strength aluminum alloy with an anodized finish to protect the exterior from corrosion. Elastomeric O-ring seals provide internal protection of the strain gages and wiring from industrial environments and moisture exposure. A [waterproof version SF3](#) is available for use in tow tanks, ocean engineering, and other underwater applications.



Units: Metric Capacity: 1112 N ▾

Dimensions (WxLxH)		76 x 76 x 76.2 mm						
Weight	0.909 Kg.				Sensing elements		Strain gage bridge	
Channels	Fx, Fy, Fz, Mx, My, Mz				Amplifier		Required	
Body Material	Aluminum				Analog outputs		6 Channels	
Temperature range	-17.78 to 51.67°C				Digital outputs		None	
Excitation	10V maximum				Cross talk		< 2% on all channels	
Fx, Fy, Fz hysteresis	± 0.2% full scale output				Fx, Fy, Fz non-linearity		± 0.2% full scale output	
Channel	Fx	Fy	Fz	Units	Mx	My	Mz	Units
Capacity	556	556	1112	N	28	28	14	N-m
Sensitivity	2.16	2.16	0.54	µv/v-N	106.3	106.3	85.06	µv/v-N-m
Natural frequency	-	-	-	Hz	500	500	-	Hz
Stiffness (X 105)	52.58	52.58	745	N/m	-	-	0.0564	N-m/rad
Resolution	To determine the resolution of your system, please use our Output Calculator .							
Notes:	The listed natural frequency is the lowest natural frequency for the force sensor and will dominate.							

Figure B.9. MC3A-250 Load Cell Specifications

12. Technical Data

12.1. Basic Specifications

Model	Table Diameter (mm)	Journal Length (mm)	Load Capacity (N [lb _r])		Tilt Load Capacity (N·m [lb _r ·in])	Stiffness (N/μm [lb _r /μin])	
			Axial	Radial		Axial	Radial
A-601.025	50	25	134 [30]	57 [13]	0.57 [5]	26 [0.15]	8 [0.05]
A-602.038	75	38	299 [67]	132 [30]	1.13 [10]	57 [0.33]	22 [0.13]
A-603.025	100	25	536 [121]	115 [26]	1.70 [15]	96 [0.55]	18 [0.10]
A-603.050	100	50	536 [121]	229 [51]	4.52 [40]	96 [0.55]	35 [0.20]
A-604.050	150	50	1206 [271]	344 [77]	22.6 [200]	210 [1.2]	64 [0.37]
A-604.090	150	90	1206 [271]	605 [135]	36.7 [325]	210 [1.2]	113 [0.65]
A-605.065	200	65	2144 [482]	577 [129]	39.6 [350]	385 [2.2]	110 [0.63]
A-605.100	200	100	2144 [482]	917 [205]	67.8 [600]	385 [2.2]	175 [1.0]
A-607.075	300	75	4244 [954]	1203 [269]	141.3 [1250]	788 [4.5]	204 [1.17]
A-607.175	300	175	4244 [954]	2789 [627]	282.5 [2500]	788 [4.5]	475 [2.71]

Model	Units	A-601.025	A-602.038	A-603.025	A-603.050	A-604.050	A-604.090	A-605.065	A-605.100	A-607.075	A-607.175
Radial Error Motion	nm	300	250	175	175	100	100	100	100	75	75
Axial Error Motion	nm	100	75	75	75	50	50	50	50	40	40
Tilt Error Motion	μrad	5	4	2.5	2.5	2	2	1.5	1.5	1	1
Max Velocity	RPM			3000				2000		1000	
Moment of Inertia	kg-mm ²	35	231	705	750	4,715	5,050	17,900	18,800	181,900	206,700
Rotating Mass	kg	0.15	0.4	0.7	0.8	2.1	2.6	4.6	5.3	19.4	26
Total Weight	kg	0.4	1.2	1.5	2.5	5.4	8.2	11.6	16.3	38.1	59.0
Operating Pressure						550 +/-35 kPa (80 +/-5 psi)					
Air Consumption						< 57 liters/minute (2.0 SCFM)					
Air Quality		<ul style="list-style-type: none"> ▪ Clean (filtered to 1.0 μm or better) - ISO 8573-1 Class 1 ▪ Oil-free -ISO 8573-1 Class 1 ▪ Dry (-15 °C dew point) - ISO 8573-1 Class 3 									
Construction		Hardcoat Aluminum SS Fasteners									

1. Load capacities listed assume supply pressure of 80 psi. Contact PI to determine load capacity if alternate supply pressures are required.
2. Precision specifications are dependent on quality of mounting surfaces, payload, orientation, and external forces on the bearing. Please consult PI for application-specific parameters. Values shown are static (zero rotational velocity during measurement).
3. Velocity may be limited by encoder options or payload imbalance.

12.2. Specifications – Optional Encoder

Model	Code	Units	A-601.xxx	A-602.xxx	A-603.xxx	A-604xxx	A-605.xxx	A-607.xxx
Resolution	H	μrad	192	133	100	66	50	33
Max Velocity		RPM	2500	2000	1500	1000	800	500
Output Signal		-	Incremental Digital RS-422 A-quad-B, Differential, 4 MHz Clock					
Index Mark		-	1 / rev, 1 count wide, Synchronized to Output Signal					
Power Input		-	5 VDC, <200 mA					
Input Ripple		-	200 mVp-p max @ up to 500 kHz					

Figure B.10. PI Glide Model A-603.050H Air Bearing Specifications

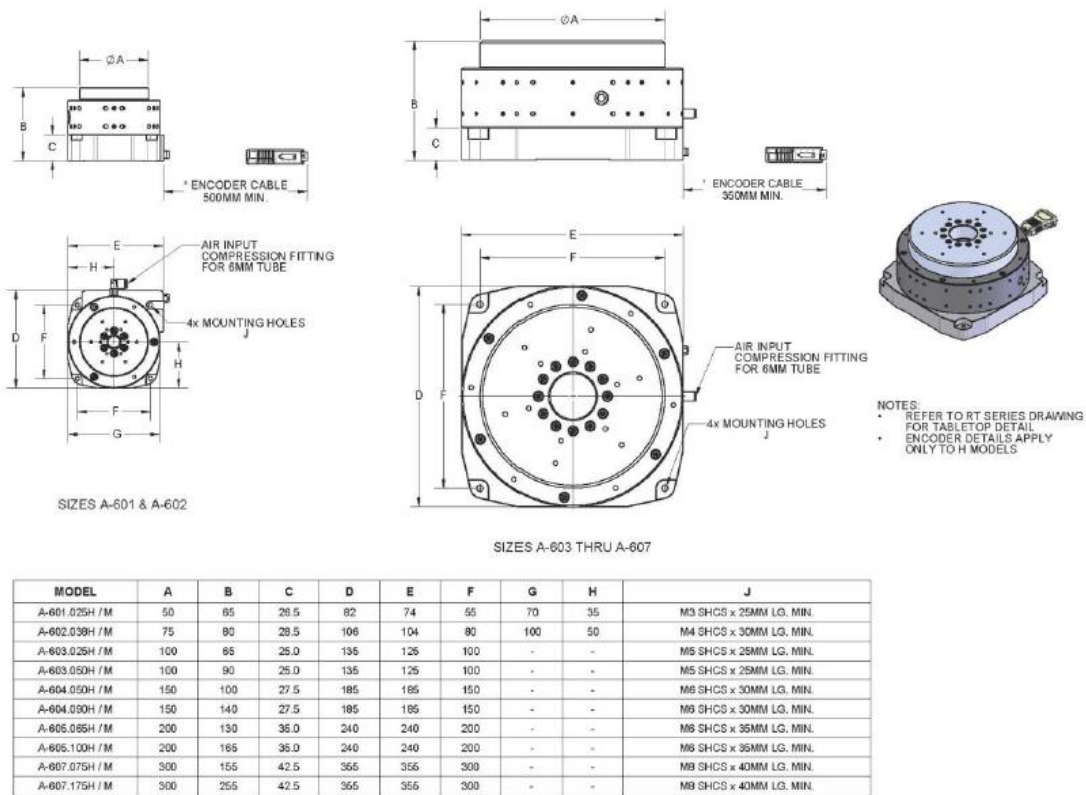


Figure B.11. PI Glide Model A-603.050H Air Bearing Specifications Continued

- The Powerbox serves as a complete replacement package for receiver mounted units or for custom OEM applications.
- Low noise level: 62-64 dB(A)



- Options:**
- Manifold (including pressure switch, safety valve, pressure regulator, pressure gauge and connections).

LFx Powerbox

- Powerbox mounted on a 20 l internally epoxy-coated air receiver for storing oil-free clean air.
- Wheel set for easy transportation.
- Standard pressure switch for start/stop regulation, safety valve, pressure regulator, pressure gauge and 3 m cable and plug¹.



- Options:**
- Desiccant dryer.
 - Galvanized receiver.
 - Electronic timer drain.
 - Solenoid valve.
 - Cable & plug for UK, Switzerland, Italy or Australia.

LFx Trolley

- Powerbox mounted on a 50 or 90 l internally epoxy-coated air receiver for storing oil-free clean air.
- Standard pressure switch for start/stop regulation, safety valve, pressure regulator, pressure gauge and 3 m cable and plug¹.



- Options:**
- Wheel set.
 - Desiccant dryer.
 - Galvanized receiver.
 - Electronic timer drain.
 - Solenoid valve.
 - Cable & plug for UK, Switzerland, Italy or Australia.

LFx Tank Mounted

¹ Standard CE 7/7 plug for 50 Hz / NEMA 5-20 plug for 60 Hz.

Technical specifications

	W	D	H	Maximum dimensions		Weight		Noise level		
				mm (W x D x H)	inch (W x D x H)	kg	lbs	dB(A)		
Powerbox	LFx 0.7/1.0		520 x 340 x 490		20.5 x 13.4 x 19.3		26	56	62-63	
	LFx 1.5/2.0		520 x 340 x 490		20.5 x 13.4 x 19.3		29	63	63-64	
Trolley (receiver 20 l)	LFx 0.7/1.0		520 x 440 x 824		20.5 x 17.3 x 32.4		44	97	62-64	
	LFx 1.5/2.0		520 x 440 x 824		20.5 x 17.3 x 32.4		48	105	62-64	
Tank mounted (vessel 50 l)	LFx 0.7/1.0		828 x 365 x 891		32.6 x 14 x 35		49	108	65-67	
	LFx 1.5/2.0		828 x 365 x 891		32.6 x 14 x 35		53	117	65-67	
Tank mounted (vessel 90 l)	LFx 0.7/1.0		960 x 364 x 973		37.8 x 14.3 x 38.3		64	141	65-67	
	LFx 1.5/2.0		960 x 364 x 973		37.8 x 14.3 x 38.3		68	149	65-67	
		Compressor type		Max. working pressure		Capacity FAD		Installed power		
		50 Hz		bar	psig	l/s	m ³ /min	cfm	kW	hp
		LFx 0.7		10	145	1.02	0.06	2.16	0.55	0.7
		LFx 1.0		10	145	1.39	0.09	2.92	0.75	1
		LFx 1.5		10	145	2.07	0.18	4.38	1.1	1.5
		LFx 2.0		10	145	2.53	0.12	5.36	1.5	2
		Compressor type		Max. working pressure		Capacity FAD		Installed power		
		60 Hz		bar	psig	l/s	m ³ /min	cfm	kW	hp
		LFx 0.7		10	145	1.35	0.081	2.86	0.55	0.7
		LFx 1.0		10	145	1.46	0.097	3.09	0.75	1
		LFx 1.5		10	145	2.39	0.14	5.06	1.1	1.5



Atlas Copco

Never use compressed air as breathing air without prior purification in accordance with local legislation and standards.

www.atascopco.com

Figure B.12. Atlas Copco Air Compressor for Air Bearing Supply

8-bit A/D and D/A converter

PCF8591

1 FEATURES

- Single power supply
- Operating supply voltage 2.5 V to 6 V
- Low standby current
- Serial input/output via I²C-bus
- Address by 3 hardware address pins
- Sampling rate given by I²C-bus speed
- 4 analog inputs programmable as single-ended or differential inputs
- Auto-incremented channel selection
- Analog voltage range from V_{SS} to V_{DD}
- On-chip track and hold circuit
- 8-bit successive approximation A/D conversion
- Multiplying DAC with one analog output.



2 APPLICATIONS

- Closed loop control systems
- Low power converter for remote data acquisition
- Battery operated equipment
- Acquisition of analog values in automotive, audio and TV applications.

3 GENERAL DESCRIPTION

The PCF8591 is a single-chip, single-supply low power 8-bit CMOS data acquisition device with four analog inputs, one analog output and a serial I²C-bus interface. Three address pins A0, A1 and A2 are used for programming the hardware address, allowing the use of up to eight devices connected to the I²C-bus without additional hardware. Address, control and data to and from the device are transferred serially via the two-line bidirectional I²C-bus.

The functions of the device include analog input multiplexing, on-chip track and hold function, 8-bit analog-to-digital conversion and an 8-bit digital-to-analog conversion. The maximum conversion rate is given by the maximum speed of the I²C-bus.

6 PINNING

SYMBOL	PIN	DESCRIPTION
AIN0	1	analog inputs (A/D converter)
AIN1	2	
AIN2	3	
AIN3	4	
A0	5	hardware address
A1	6	
A2	7	
V _{SS}	8	negative supply voltage
SDA	9	I ² C-bus data input/output
SCL	10	I ² C-bus clock input
OSC	11	oscillator input/output
EXT	12	external/internal switch for oscillator input
AGND	13	analog ground
V _{REF}	14	voltage reference input
AOUT	15	analog output (D/A converter)
V _{DD}	16	positive supply voltage

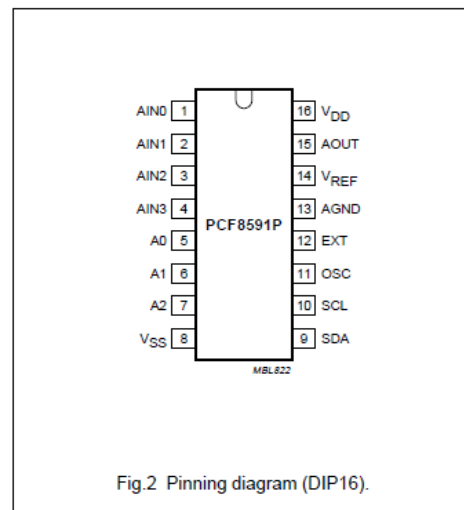
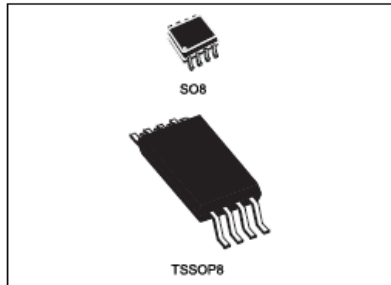


Fig.2 Pinning diagram (DIP16).

Figure B.13. PCF8591 ADC/DAC Specifications



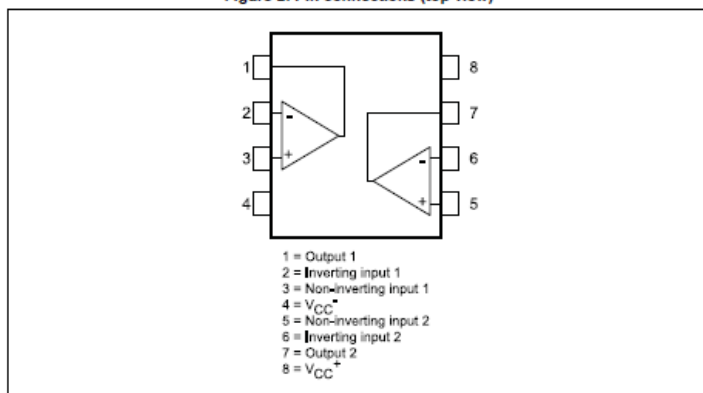
Description

The TL082, TL082A and TL082B are high speed JFET input dual operational amplifiers incorporating well-matched, high voltage JFET and bipolar transistors in a monolithic integrated circuit.

The devices feature high slew rates, low input bias and offset current, and low offset voltage temperature coefficient.

2 Pin connections

Figure 2: Pin connections (top view)



3 Absolute maximum ratings and operating conditions

Table 1: Absolute maximum ratings

Symbol	Parameter	TL082I, AI, BI	TL082C, AC, BC	Unit	
V_{CC}	Supply voltage ⁽¹⁾	± 18		V	
V_{in}	Input voltage ⁽²⁾				
V_{id}	Differential input voltage ⁽³⁾				
P_{tot}	Power dissipation	680		mW	
R_{ThA}	Thermal resistance junction-to-ambient ⁽⁴⁾				
R_{ThC}	SO8	125		$^{\circ}\text{C}/\text{W}$	
	TSSOP8	120			
R_{ThC}	SO8	40			
	TSSOP8	37			
Output short-circuit duration ⁽⁵⁾		Infinite			
T_{stg}	Storage temperature range	-65 to 150		$^{\circ}\text{C}$	
ESD	HBM: human body model ⁽⁶⁾	1	kV	V	
	MM: machine model ⁽⁷⁾				
	CDM: charged device model ⁽⁸⁾				

Figure B.14. TL082 Operational Amplifier Specification

CURRICULUM VITAE

PERSONAL INFORMATION

Surname, Name : Akbulut, Burak
Nationality : Turkish (TC)
Date and Place of Birth : 1985, Ankara
Phone : +90 312 811 18 00 / 14150
E-mail : e134632@metu.edu.tr

EDUCATION

Degree	Institution	Year of Graduation
MBA	Bilkent University, Faculty of Business Administration	2016
MS	METU Mechanical Engineering	2009
BS	METU Aerospace Engineering with Minors in Mechatronics	2006
High School	Atatürk Anadolu High School, Ankara	2002

WORK EXPERIENCE

Year	Place	Enrollment
2007-Present	Turkish Aerospace Inc.,	ADCS Engineer

FOREIGN LANGUAGES

Advanced English

PUBLICATIONS AND CONFERENCE PROCEEDINGS

1. F. Arberkli, B. Akbulut, O. Tekinalp and K. Azgın “Dynamic Model and Experimental Results of a Novel Reaction Wheel”, AIAA Journal of Spacecraft and Rockets, 2019 (submitted)
2. B. Akbulut, F. Arberkli, O. Tekinalp and K. Azgın “Oscillating Control Moment Gyroscope Mathematical Model Development, Verification and Results”, 32nd ISTS & 9th NSAT Joint Symposium, Fukui, Japan, June 15-21, 2019

3. B. Akbulut and E. Arıkan “Geostationary Transfer Orbit to Moon Low Thrust Transfer Design for a Small Satellite”, 9th International Conference on Recent Advances in Space Technologies, İstanbul, Turkey June 11-14, 2019
4. B. Akbulut, F. Arberkli, O. Tekinalp and K. Azgin “Oscillating Control Moment Gyroscope Experimental Results”, AIAA SciTech Forum, San Diego, CA, USA January 7–11 2019
5. B. Akbulut, F. Arberkli, O. Tekinalp and K. Azgin “A Hypothetical Mechanical Design for Vibrating Mass Control Moment Gyroscopes”, 2018 Space Flight Mechanics Meeting, AIAA SciTech Forum, Kissimmee, Florida, USA January 8–12 2018
6. B. Akbulut, F. Arberkli, O. Tekinalp and K. Azgin “Experimental Characterization and Validation of Vibrating Rotor Control Moment Gyroscope”, 2017 AIAA SPACE and Astronautics Forum & Exposition, Orlando, Florida, USA September 12-14, 2017
7. Y. E. Aras, M. C. Soydan, M. N. Uyar, M. S. Harmankaya and B. Akbulut “Developing and Modelling of Satellite Docking Algorithm”, 8th International Conference on Recent Advances in Space Technologies, İstanbul, Turkey June 19-22, 2017
8. B. Akbulut, K. Ataalp, M. Ünlü “A Multi-Mode Rendezvous Control Algorithm for a Satellite Utilizing Stereo Camera Based Proximity Sensor”, 27th AAS/AIAA Space Flight Mechanics Meeting, San Antonio, Texas, USA February 5-9, 2017
9. B. Akbulut, F. Arberkli, O. Tekinalp and K. Azgin “A Simplified Model for Vibrating Mass Control Moment Gyroscope”, 27th AAS/AIAA Space Flight Mechanics Meeting, San Antonio, Texas, USA February 5-9, 2017
10. B. Akbulut, F. Arberkli, O. Tekinalp and K. Azgin “Vibrating Mass Control Moment Gyroscope Dynamic Model Validation Study”, AIAA/AAS Astrodynamics Specialist Conference Long Beach, CA, USA September 13-16, 2016
11. B. Akbulut, O. Tekinalp and K. Azgin “Vibrationally Excited Satellite Attitude Actuator: a Feasibility Study”, 7th International Conference on Recent Advances in Space Technologies, İstanbul, Turkey June 16-19, 2015
12. B. Akbulut et al “ADCS Sensor Placement on an Earth Observation Satellite”, 7th International Conference on Recent Advances in Space Technologies, İstanbul, Turkey June 16-19, 2015
13. O. C. Sakinci, A. Sen, C. Tansu, E. C. Ünlüsoy, M. Yurtcu, N. Evirgen and B. Akbulut “Proof of Concept for Satellite Attitude Determination Using GNSS”, 7th International Conference on Recent Advances in Space Technologies, İstanbul, Turkey June 16-19, 2015
14. O. Kayhan, S. Aydin, C. Guzenge, A. Kaya, E. C. Kovan, M. Kemal, K. Yurtcu and B. Akbulut “Tracking of Low Earth Orbit Satellites by Optical Systems”, 7th International Conference on Recent Advances in Space Technologies, İstanbul, Turkey June 16-19, 2015
15. O. F. Kilic, H. Yildiz, M. Poyraz, S. Ozdemir, S. Mutlu and B. Akbulut “Visual Guidance System for Satellite Rendezvous Applications”, 7th International Conference on Recent Advances in Space Technologies, İstanbul, Turkey June 16-19, 2015

16. B. Akbulut and O. Tekinalp "Architectures for Vibrating Mass Attitude Control Actuators", 25th AAS/AIAA Space Flight Mechanics Meeting, Williamsburg, VA, USA, January 11-15 2015
17. B. Akbulut et al "Design of an Earth-Observation Satellite Constellation via Image Return Time Figure of Merit", presented at 1st IAA Conference on Dynamics and Control of Space Systems, Porto, Portugal, March 19-21 2012
18. S. Kayashta, B. Akbulut, O. Tekinalp and K. Ozgoren "Attitude Control of a Piezo-Strut Mounted Camera on a Spacecraft with Deployed Solar Panels", presented at IEEE Aerospace Conference, Big Sky, MT, USA, March 5-12 2011
19. B. Akbulut, K. Ozgoren and O. Tekinalp "Attitude Control of a Multiple Rigid Body Spacecraft with Flexible Joints", 20th AAS/AIAA Space Flight Mechanics Meeting, San Diego, CA, USA, February 14-17 2010
20. B. Akbulut, A. Altay and A. Özkan "Preliminary Earth Observation Mission Design with the Mission Analysis Tool" presented at International Workshop on Small Satellites, New Missions and New Technologies, İstanbul, Turkey June 5-7, 2008
21. B. Akbulut, A. Altay and A. Özkan "Satellite Altitude Decay Estimation via GPS Position Data" presented at International Workshop on Small Satellites, New Missions and New Technologies, İstanbul, Turkey June 5-7, 2008